Atomistic Models of Magnetic Systems with Combined Ferromagnetic and Antiferromagnetic Order

JOSEPH BARKER

A Thesis Submitted for the Degree of Doctor of Philosophy

THE UNIVERSITY OF YORK

DEPARTMENT OF PHYSICS

September 2013

Abstract

There has long been an interest in the exploitation of novel magnetic behaviour for practical applications such as magnetic storage devices. Some of the most interesting dynamical behaviour occurs when a material contains both ferromagnetic (FM) and antiferromagnetic (AF) characteristics. Many such systems have forgone study due to practical difficulties of experimental observation of antiferromagnetic order. In this work several systems of current interest which contain both AF and FM order are studied. These materials and systems are used, or are candidates for, technological applications, especially magnetic storage devices. The forefront in this area is concerned with laser induce magnetisation reversal and there are many unexplained phenomena, especially in ferrimagnetic and metamagnetic materials. A combination of analytical and large scale numerical calculations are used, often with comparison to experimental data where available. The approach used is generally based around so-called atomistic spin dynamics, where the Landau-Lifshitz-Gilbert equation, augmented with a Langevin term, is solved for each atomic moment. This allows the description of magnetic materials at elevated temperatures and through phase transitions. Semi-analytic formalisms are studied, comparing with atomistic spin dynamics and micromagnetics, to inform multiscale modelling techniques. The excitation of a localised mode an antiferromagnetic layer which is coupled to a ferromagnetic layer is studied. It is shown that this excitation leads to an enhanced damping of the ferromagnet, an important consideration for the design and optimisation of spin valves. The metamagnet FeRh which undergoes an antiferromagnetic-ferromagnetic phase transition is also investigated. There is much debate about the origin of the phase transition and a model is constructed in this work which demonstrates that an all magnetic origin is possible if effective four spin exchange terms are considered. This model is also capable of explaining the observed dynamics in femtosecond laser heating experiments. Finally, the spin wave dynamics of the prototypical amorphous ferrimagnet GdFeCo are considered. The thermally induced switching which has been discovered in this material is explained as the excitation of a two-magnon state.

Contents

List of Figures

List of Tables

Acknowledgements

I have been very fortunate to have had Professor Roy Chantrell as a guiding influence for the last eight years. The many opportunities he has afforded me and the constant encouragement he has provided are a debit which I can never repay to him. I thank him for all of his help and guidance in all matters over the years and I hope that in the future I can apply what I have learnt from him.

I thank my colleagues and collaborators who have constantly stimulated my work and provided help and support in many forms, Tom Ostler, Jerome Jackson, Unai Atxitia, Ceilia Aas, Ondrej Hovorka, Ramon Cuadrado, Noi Chureemart and Oksana Chubykalo-Fesenko, Simon Frostick. I am extremely grateful for the support of my family and close friends who have kept me on track through thick and thin, especially the Cleggs, the Jacksons and the Drings.

Declaration

All work is the original work of the author except where explicitly indicated. This work has not been submitted to any other examining body or for any other degree. Much of the work has been published or publicly presented by the author.

Joseph Barker
York, September 2013

List of abbreviations

AC	alternating current
AF	antiferromagnetic
ASD	atomistic spin dynamics
BCC	body centered cubic
CPU	central processing unit
CSDM	classical spectral density method
CSR	compressed sparse row
DC	direct current
DFT	density functional theory
DSF	dynamic structure factor (dynamics scattering function)
DIA	diagonal
EM	electro-magnetic
FM	ferromagnetic
FMR	ferromagnetic resonance
FT	Fourier transform
GPU	graphical processing unit
HAMR	heat assisted magnetic recording
IFE	inverse Faraday effect
ISF	intermediate structure factor (intermediate scattering function)
KKR	Korringa-Kohn-Rostoker scattering
LLB	Landau-Lifshitz-Bloch
LLG	Landau-Lifshitz-Gilbert
LSWT	linear spin wave theory
MOKE	magneto-optical Kerr effect
NM	non-magnetic
OU	Ornstein-Uhlenbeck
QSA	quasi-static approximation
RPA	random phase approximation

SNR . . . . . signal to noise ratio
SpMV . . . . . sparse matrix vector product
TIMS . . . . . thermally induced magnetisation switching
XMCD . . . . . X-ray magnetic circular dichrosim
XMLD . . . . . X-ray magnetic linear dichrosim

List of symbols

a . . . . . lattice parameter
$\hat{a}_i$ . . . . . annihilation operator
$\hat{a}_i^\dagger$ . . . . . creation operator
α . . . . . Gilbert damping parameter
$\alpha(m)$ . . . . . longitudinal correlation decoupling function
$A(T)$ . . . . . micromagnetic exchange stiffness at temperature T
$\mathcal{A}_{\mathbf{k}}$ . . . . . combined band amplitude along wave vector $\mathbf{k}$
Λ . . . . . energy dissipation constant
b_{ij} . . . . . electron hopping matrix elements
β . . . . . $1/k_{\mathrm{B}}T$
C_e . . . . . electronic heat capacity
C_p . . . . . phonon heat capacity
$C(\mathbf{r}-\mathbf{r}')$ . . . . . spin-spin equal time correlation function
$C(\mathbf{r}-\mathbf{r}',t)$ . . . . . spin-spin space time correlation function
d_z . . . . . uniaxial anisotropy energy
D_{ijkl} . . . . . four spin exchange interaction energy
e . . . . . electron charge
$\hat{\mathbf{e}}$ . . . . . unit vector
ε_f . . . . . Fermi energy
$\mathcal{E}$ . . . . . energy
$\mathcal{E}_0$ . . . . . initial energy
ΔE . . . . . energy barrier
$\mathbf{E}$ . . . . . electric field
F . . . . . free energy
f_0 . . . . . FMR frequency
$FT_{(\mathbf{r})}[A(\mathbf{r},t)]$ . . . . . Fourier transform in space of field A(**r**,t)
$FT_{(\mathbf{t})}[A(\mathbf{r},t)]$ . . . . . Fourier transform in time of field A(**r**,t)
$\varphi(t-t')$ . . . . . memory kernel between time t and t'

γ . . . . . gyromagnetic ratio
$\gamma_{\mathbf{k}}$ . . . . . reciprocal lattice interaction vectors
G_{ep} . . . . . electron-phonon coupling strength
H_{ani} . . . . . anisotropy field
H_{exc} . . . . . exchange field
$\mathcal{H}$ . . . . . Hamiltonian term
$\mathbf{H}$ . . . . . magnetic field
$\mathbb{I}$ . . . . . identity matrix
J . . . . . scalar exchange energy
$\tilde{J}$ . . . . . scalar interface exchange energy
J_0 . . . . . zero point Fourier exchange energy
J_{ij} . . . . . isotropic Heisenberg exchange energy
$J_{\mathbf{k}}$ . . . . . Fourier transform of exchange energy
$\mathbb{J}_{ij}$ . . . . . exchange energy tensor
$\mathcal{J}_{ij}$ . . . . . electron exchange matrix elements
$\mathbf{k}$ . . . . . wave vector
k_{B} . . . . . Boltzmann constant
K . . . . . scalar anisotropy energy
$\bar{K}$ . . . . . easy plane anisotropy energy
$K(T)$ . . . . . micromagnetic anisotropy energy at temperature T
$\mathbb{K}_{ii}$ . . . . . anisotropy tensor
$\mathbf{L}$ . . . . . Néel vector
$\mathbb{L}$ . . . . . set of lattice vectors
$m_e(T)$ . . . . . equilibrium magnetisation at temperature T
$\mathbf{M}$ . . . . . magnetisation
M_{s} . . . . . saturation magnetisation
η . . . . . heat bath coupling strength
$\hat{\mathbf{n}}$ . . . . . surface normal
n_s . . . . . number of random lattice clusters of size s
N . . . . . total number of an index (i,j)
$N_e^{\uparrow}$ . . . . . majority band integrated density of states
$N_e^{\downarrow}$ . . . . . minority band integrated density of states
σ . . . . . width of a Gaussian
σ_i . . . . . Dirac spinor
Ω . . . . . thermal sum of the spectral density
$\Omega_{\mathbf{k}}(\omega)$ . . . . . spectral density function
$\mathbf{p}_c$ . . . . . percolation threshold

$\mathbf{p}_i$ . . . . . position within a unit cell
P . . . . . probability
$P(t)$ . . . . . laser power at time t
$\mathbf{q}_i$ . . . . . set of integers
Q . . . . . dissipative function of a dynamical system
$\mathcal{R}$ . . . . . Rayleigh dissipation functional
s . . . . . quantum spin
$\mathbf{s}(\mathbf{r})$ . . . . . spin density at $\mathbf{r}$
$\langle S \rangle$ . . . . . mean value of spin
$\mathbf{S}_i$ . . . . . classical spin vector of unit length
$\mathbf{S}_\mathbf{k}$ . . . . . Fourier transform of classical spin vectors
$\mathbf{S}_+$ . . . . . spin raising operator
$\mathbf{S}_-$ . . . . . spin lowering operator
$\delta\mathbf{S}_i$ . . . . . small deviation of a spin vector
$\tilde{\mathbf{S}}_i$ . . . . . Euler approximation of a spin vector
$\mathcal{S}(\mathbf{k}, t)$ . . . . . intermediate structure factor
$\mathcal{S}(\mathbf{k}, \omega)$ . . . . . dynamic structure factor
$\tilde{\mathcal{S}}(\mathbf{k}, \omega)$ . . . . . discrete sampled dynamic structure factor
T . . . . . temperature
T_c . . . . . Curie temperature
T_e . . . . . electronic temperature
T_p . . . . . phonon temperature
T_M . . . . . metamagnetic transition temperature
T_{comp} . . . . . magnetisation compensation temperature
$\text{Tr}(\mathbb{A})$ . . . . . trace of matrix A
Δt . . . . . time step
μ_0 . . . . . permeability of free space
μ_B . . . . . Bohr magneton
μ_s . . . . . magnitude of a spin moment
ν . . . . . universal critical exponent
U . . . . . Coulomb interaction energy
$\mathbf{v}_i$ . . . . . integer lattice four vector
ω . . . . . angular frequency
ω_0 . . . . . FMR angular frequency
$\omega_\mathbf{k}$ . . . . . spin wave dispersion
W . . . . . Wiener stochastic process
$\mathcal{W}$ . . . . . windowing function

ξ . . . . . cluster correlation length
ξ_i . . . . . a stochastic process
$\boldsymbol{\xi}_i$ . . . . . vector of independent stochastic processes
x . . . . . fractional concentration of Gd
χ . . . . . random lattice correlation length
$\chi_\perp(T)$ . . . . . transverse magnetic susceptibility at temperature T
$\chi_\parallel(T)$ . . . . . longitudinal magnetic susceptibility at temperature T
χ_{mo} . . . . . magneto-optical susceptibility
z . . . . . coordination number of a lattice

CHAPTER 1

Introduction

1.1 Motivation

One of the primary uses for magnetic materials is for the storage of information in computer devices. The increasing appetite for digital storage capacity has driven a large part of the research in magnetism for the past 20 years. In general the aim is to increase the information density of storage devices, so that a larger volume of data can be stored on the same size of device every year. To overcome physical limitations on storage density, new radical paradigms are needed periodically to change the way in which magnetic materials are used to store the information reliably. The last major change was the introduction of perpendicular media, where the orientation of the magnetic poles storing the information was effectively changed by 90 degrees so that smaller magnetic grains could be stored in a denser array.

Once again the limits of the current technology are being reached and without radical change, it will not be possible to increase the data density of magnetic hard drives. There is also now the competition of *solid state* hard drives which store information using charge. Currently such devices are limited by the lithographic processes which are used to create the circuits and solid state hard drives are considerably more expensive than magnetic hard drives and have a limited lifetime, although solid state devices have the advantage of speed and low power consumption. For magnetic hard drives to remain relevant against such competition, they must continue to offer higher storage densities and lower prices.

Magnetic recording tri-lemma

Improvements in magnetic hard drives must continuously balance three competing and contradictory requirements, a change in one aspect of the tri-lemma must be reconciled with the other two facets[1]. The first of these requirements is that of longevity. Magnetic hard drives must store information without corruption for long periods of time, even when no power is being supplied, this is called non-volatile memory, and is essentially the purpose of a hard drive within a computer. The competing processes against this stability is thermal energy. Bi-stable magnetic systems can thermally relax over the energy barrier which defines the orientation of the system. The energy barrier which prevents thermal switching must be of a minimum height so that the probability of thermal switching in a given time is low. In magnetic hard drives this time scale is conventionally required to be $\sim$ 10 years. The energy barrier utilised in magnetic storage originates from the magnetic anisotropy energy of a material and the probability of reversal follows the Arrhenius-Néel law

$$P = f_0 \mathrm{e}^{-\frac{\Delta E}{k_\mathrm{B} T}} \tag{1.1}$$

where f_0 is the attempt frequency (usually taken as $1 \times 10^9 \mathrm{s}^{-1}$, ΔE is the anisotropy energy barrier, k_B is the Boltzmann constant and T is the temperature. The energy barrier is approximately KV where K is the anisotropy per unit volume and V is the volume of a magnetic grain. This leads to the second requirement, which is signal to noise ratio (SNR). Information *bits* are stored on collections of magnetic grains. Each collection must be made of enough grains that the transition between bits is quite sharp so that the signal can be detected by the read head. This means that the grains must be quite small compared to a bit, but because the energy barrier depends on the volume, the anisotropy energy of the magnetic material must be higher if we reduce the size of grains so that the storage density can be increased. This however conflicts with the final aspect of the tri-lemma, write-ability. The maximum field that a write head can generate is $\sim$1.8T and this field must be sufficient to force the magnetisation over the anisotropy energy barrier. If the anisotropy energy is too high then it will be impossible to write information to the hard drive.

Hard drives have now reached the limit where the anisotropy energy required to reduce the grain size is so great that it would not be possible to write the information. This has led to a new paradigm known as heat assisted magnetic recording (HAMR). This idea is centered on the fact that the effective anisotropy of a magnetic material is temperature dependent. Therefore one can heat the magnetic grains upon writing, reducing the

effective anisotropy, so making it possible to change the state with the write field. Upon cooling the magnetic anisotropy recovers and so the thermal stability of the information is ensured. The fundamental research behind HAMR is now mostly complete[2] and the implementation is underway[3]. So research has now turned to finding new ideas and phenomena in magnetic materials to address densities and importantly, speeds, beyond that which HAMR can provide. One of the most promising areas is that of all optical magnetisation switching, where the writing would no longer require a write pole to generate a field, but the laser itself could cause the switching. This research comes from the area of sub-picosecond magnetism, where many novel experiments have been performed, showing promise for data storage applications[4].

1.2 Sub-picosecond magnetism

The pioneering work in the field of sub-picosecond magnetism was performed in 1996 by Beaurepaire *et al.*who demonstrated that Nickel could be significantly demagnetised in less than one picosecond with the application of a 60 fs laser pulse (Fig. 1.1a)[5]. The mechanism for this demagnetisation was well described in their original paper in terms of three coupled thermal heat baths; lattice, electron and spin. It was proposed that the laser primarily excites the electronic heat bath to extreme temperatures, with the spins and lattice degrees of freedom coupling to this. This explanation has withstood the test of time and is the accepted explanation of ultrafast demagnetisation on the picosecond timescale.

In 2004 experiments using the Stanford Linear Accelerator (SLAC) were published with the aim of finding the limit of deterministic switching in terms of short time, high field pulses[6]. The authors used the magnetic field of an X-ray beam to create a radially dependent magnetic field strength with a pulse duration of 2.3 picoseconds and applied this to a CoCrPt granular medium. They found deterministic switching only to 1.7 T. Beyond this the switching became randomised. The implied result is that for very short timescales, high intensity magnetic fields excite non-uniform modes which means that coherent reversal is no longer possible.

GdFeCo

Following this work, the group of Rasing at Radboud University in Nijmegen have been leading the cutting edge of experimental research in sub-picosecond excitation of magnetic materials. One of the early remarkable results from this group was the

excitation of a high frequency precessional mode in $DyFeO_3$. Intriguingly, the chirality of the laser pulse also selected the phase of the mode[7] (Fig. 1.1b). The result was explained as the occurrence of a magnetic field induced within the material by the laser, known as the inverse Faraday effect. The estimate of the size of such a field was put at 5 T, a very large magnetic field. This result prompted further work in the group to try an determine if the magnetic state of a material could be reversed with this large induced field. In 2007 this aim was realised when Stanciu *et al.* demonstrated helicity-dependent laser induced magnetisation reversal in GdFeCo using a 40 fs laser pulse[4] (Fig 1.1c).

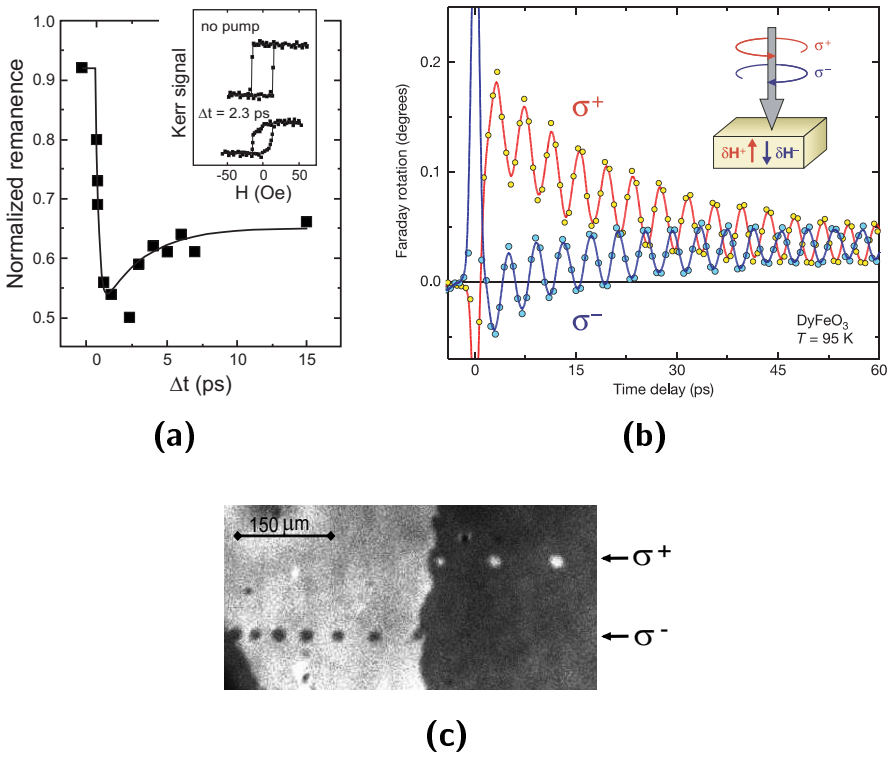

Figure 1.1 | Pioneering experiments in sub-picosecond laser excitation. **(a)** The magneto-optical signal showing the sub-picosecond demagnetisation of Nickel after a 60 fs laser pulse. From Beaurepaire *et al.*, 1996[5,8]. **(b)** Excitation of $DyFeO_3$ showing chirality dependent excitation of a precessional mode after a 200 fs laser pulse. From Kimel *et al.*, 2005[7]. **(c)** 40 fs laser pulses reverse small regions as they are strobed across magnetic domains in GdFeCo. σ^+ and σ^- are the two polarisations of laser light. Reversal of the magnetisation depends on the chirality. From Stanciu *et al.*, 2007[4].

Following this discovery, many researchers, both experimental and theoretical, have been attempted to shed light on what happens to magnetic systems in the sub-picosecond regime. Ostler *et al.* then made the remarkable discovery that no external magnetic field (from the laser or otherwise) was required to explain the reversal in GdFeCo[9]. The reversal was shown to be deterministic both by modelling and

experiment. A deterministic switching in a uniaxial magnetic system by heat alone is both completely unexpected and beyond any existing explanation of magnetism. This series of discoveries in GdFeCo has stimulated much of the work in this thesis, especially with regard to the analysis of spin waves during laser heating.

FeRh

With femtosecond laser systems becoming more common, experiments have also been performed on other interesting materials. One of the more novel examples is FeRh. It has long been known that FeRh has an AF-FM phase transition with temperature, but Ju *et al.* showed that FM order could be generated in less than a picosecond by apply a 100fs laser pulse[10]. Such a fast transition between AF and FM origin suggests a magnetic origin to the phase transition rather than originating from the lattice expansion as previously believed. In FeRh also, attention was now paid to the microscopic mechanisms which cause this behaviour.

All optical recording has the potential to extend magnetic storage technology beyond the current limits. Crucially, because no applied field is required, the limit of the write pole field no longer exists. With a magnetic write head, the stray magnetic fields must be carefully managed to avoid altering adjacent bits of information. The fact that no write pole is required also could simplify the design of write head transducers, greatly simplifying the manufacture of hard rives, thus reducing cost.

1.3 Modelling Magnetic Materials

A large number of different models exist for magnetic materials. This is because often the behaviour of magnetic materials is very different on differing length and time scales. The origin of magnetic behaviours can also differ between materials. Recently atomistic scale modelling has become a very active area of research as people wish to investigate fast time scale, finite temperature effects in magnetic materials.[†] Research in this area aims to answer both fundamental questions about the fast timescales of magnetic processes and provide technological advances in areas such as magnetic memory storage.

On the smallest length scales, around a few angstroms, magnetism can be modelled within a quantum mechanical framework such as density functional theory (DFT) or

[†] See for example refs.[11–15]

Korringa-Kohn-Rostoker scattering (KKR). These techniques allow one to calculate the magnetic behaviour of materials arising from the electronic wavefunction. Such first principles techniques are useful for understanding the origin of magnetism within a given material and calculate magnetic moments and fundamental properties such as the exchange energy or anisotropic energies. The limit of such first principal techniques is that they can only be applied to small periodic unit cells or small finite collections of atoms.[†] Furthermore, dynamic and finite temperature effects cannot easily be included in such formalisms, especially if one wishes to consider non-equilibrium scenarios.

Beyond a first principles approach, one may consider models of an atomistic scale where model dimensions are measure in nanometres. These include models such as the Hubbard model, Ising model and Heisenberg model. At this length scale we consider discretized atomic sites and the energetic considerations of a moment associated with each atomic site. Due to the simplified Hamiltonians employed in these models, the statistical behaviour of large numbers of moments can be calculated. Techniques also exist to include thermal effects in these models and in some cases an equation of motion can be written for the moment. The statistical ensemble of many atomic sites allows macrospin thermodynamic variables to be calculated and it is possible to model magnetic phase transitions.

The largest length scales use a continuum approach, essentially solving Maxwell's equations to determine the magnetic state dependent on a materials geometry. This is known as micromagnetics and is good on length scales of tens of nanometres to micrometres. The limiting factor here is that the long wavelength approximation does not allow high temperature effects to be modelled. Similarly, non-equilibrium dynamics cannot be reproduced on short length and time scales. Overcoming such limitations in micromagetics is an active field of research. Approaches such as the Landau-Lifshitz-Bloch equation have been shown to be accurate for finite temperature and non-equilibrium scenarios despite modelling materials using a macrospin of dimensions much greater than an individual atomic site[17,18]. On the same length scale as micromagnetics there are also techniques which allow the modelling of very long term behaviour. Kinetic Monte-Carlo allows one to assess the probability of the macroscopic magnetisation of particle moving between energy minima on very long time scales and at finite temperatures[19]. While not a true dynamic formalism this does allow access to long time regimes which cannot be assessed with any other modelling technique.

[†]For example Gruner [16] does *large scale* calculations with 561 atoms.

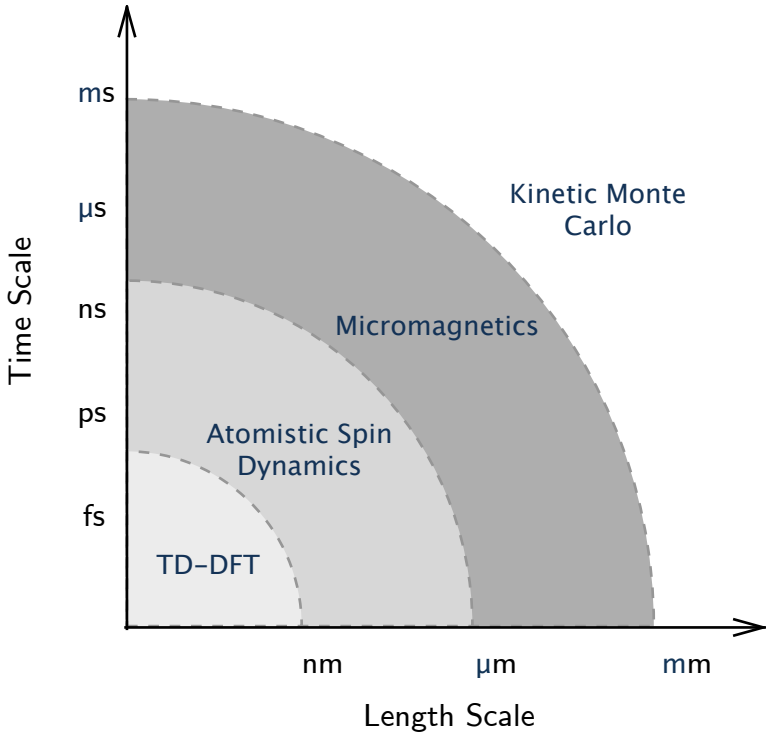

Figure 1.2 | Time and length scales of magnetic modelling methods. Approximate regions of time and length scales which can be addressed by different magnetic modelling techniques.

In studying the sub-picosecond laser excitation of magnetic materials it is atomistic spin dynamics which is the most appropriate approach, due to the large temperatures and non-equilibrium regimes that are accessed. Work by Schellekens and Koopmans has shown that this approach is well justified from a theoretical point of view[20]. They compare this approach with a band model approach[21,22], and find that the atomistic dynamics are the dominant contribution to the demagnetisation.

CHAPTER 2

Atomistic Spin Dynamics

To model dynamic, finite temperature magnetic systems the most common approach is that of atomistic spin dynamics (ASD). This classical approach lies between quantum mechanical first principles methods and the continuum approach of micromagnetism. By using a canonical ensemble of classical spin vectors, coupled by the Heisenberg exchange interaction, and solving their equation of motion, finite temperature statistical systems can be solved without the need to calculate the entire partition function. ASD starts on the classical Heisenberg model, where the quantum mechanical exchange interaction is reduced to a pairwise interaction between classical spin vectors which rotate about the unit sphere rather than being quantised in size or direction. Even so, the link between the quantum and classical Heisenberg models is strong as both regimes share the same equation of motion. The Heisenberg model is often augmented with additional terms to model other effects such as relativistic crystal field interactions or the dipole-dipole interaction between the classical moments. Such models are called extended Heisenberg models.

2.1 The Origin of Atomic Magnetic Moments

Atomistic magnetic moments originate from two sources, the orbital motion of electrons about atomic nuclei and the intrinsic spin of the electrons. The orbital contribution to the moment is created because of the movement of the electronic charge about the nucleus. A current loop such as this induces a magnetic moment, however in solid state materials and particularly metallic systems, this contribution is negligible. The delocalisation of the electrons and the strong electrostatic interactions with the crystal field reduces the orbital contribution significantly, this is known as

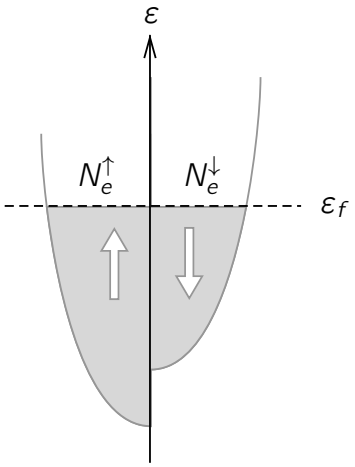

Figure 2.1 | Stoner model of ferromagnetism. The density of states integrate to the Fermi energy (ε_f) is different for spin up ($N_e^{\uparrow}$) and spin down ($N_e^{\downarrow}$) bands resulting in a net spin moment.

quenching.[23,24]. The majority of the observed magnetic moment in bulk materials results from the intrinsic spin of the electrons. In insulating materials an atomistic spin moment forms when there is an excess of spin up (or down) electrons due to the Pauli principle. This effect is largest in $3d$ and $4f$ species due to the large number of states available in the outer, partially filled orbitals (Fig 2.2). However in metallic systems the largely delocalised nature of the electronic wavefunction means that we cannot easily describe the system in terms of discrete orbitals. This is apparent if one considers the magnetic moment per atom of a material such as Fe. According to the Pauli principle and Hund's rules there should be six unpaired $3d$ electrons per Fe atom, leading to a large moment which is an integer multiple of the Bohr magneton. Experimentally Fe is found to have a moment of $2.21\mu_{\mathrm{B}}$ which is both smaller and non-integer. The simplest model which takes into account the band structure of such materials is the Stoner model where the Weiss field from the adjacent atoms in the lattice causes a splitting of the electron band structure[24,25]. This leads to a difference in the integrated density of states of the spin-up and spin-down states at the Fermi energy (Fig. 2.1). The difference in these gives the net moment, thus one obtains a moment which is not an integer of μ_{B} but is instead defined as

$$m = \mu_{\mathrm{B}} \left(N_e^{\uparrow} - N_e^{\downarrow} \right) \tag{2.1}$$

where $N_e^{\uparrow}$ and $N_e^{\downarrow}$ are the density of states of each spin channel integrated up to the Fermi energy.

This still leaves the difficult concept of reconciling the band picture of magnetism with the localised approximation we must use for atomistic spin dynamics so that the

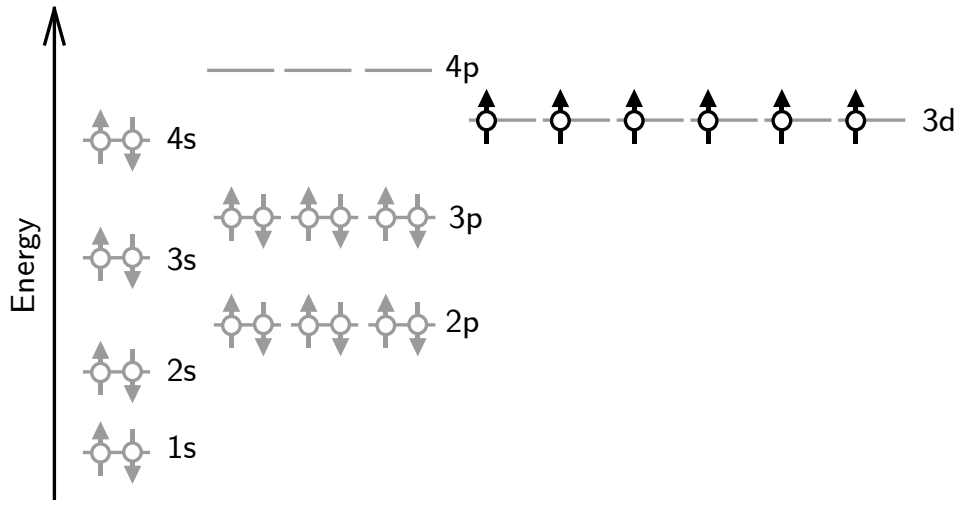

Figure 2.2 | Localised moment model of ferromagnetism. The Pauli principle leads to unpaired electrons within the atomic orbitals which gives a large net spin moment. The example here is for Fe, where in the localised moment picture there are six unpaired electrons in the 3d shell.

magnetism from the spin degrees of freedom can be discretised into classical spin vectors. To do this an adiabatic approximation must be taken to separate the timescales of magnetism into fast and slow processes. One can consider an atomic sphere with a volume, Ω, within which we attribute all of a wavefunctions spin moment, $\mathbf{s}$, to a particular atomic site. We need to know the timescale on which it is valid to say the magnitude of the total magnetic moment is constant within this sphere. For a moment to be persistent on some time scale, the correlation time of the spin orientation must be shorter than the timescale on which the classical spin vectors move within the classical Heisenberg model. Gyorffy, Pindor, Staunton, Stocks & Winter [26] study this issue in detail and give approximate values of 10^{15} Hz for the intersite hopping frequency of electrons and $\nu = 10^{13}$ Hz as a typical spin-wave frequency. Thus the moment attributed to an atom is written as the time and space integral within which electrons typically persist within the defined atomic sphere[27]

$$\mathbf{S}(t) = \frac{\nu}{2} \int_{\Omega} \mathrm{d}^3 r \int_{t-\frac{1}{\nu}}^{t+\frac{1}{\nu}} \mathrm{d}t' \mathbf{s}(\mathbf{r}, t'). \tag{2.2}$$

From here, the term spin will generally refer to the atomic magnetic moment $\mathbf{S}(t)$. In the context of atomistic spin dynamics, it is important that we do not draw strong conclusions on timescales faster that the order of 10 femtoseconds beyond which, electronic interactions will require a more rigorous treatment such as the calculation of spin transport[21]. One must also keep in mind that the lack of spin quantisation in

the ASD approach does not necessarily describe all magnetic materials well and other approaches may be appropriate such as the Hubbard Model[28].

2.2 The Exchange Interaction

Reducing our view of magnetism to isolated classical spin vectors we must consider the interactions which exist between such moments. While we have discretised the system with the atomic sphere approximation, we must include certain effects that are quantum mechanical in origin which cause interactions across the system. In fact, ordered magnetism is essentially quantum mechanical in origin and the most important effect we must include is that of exchange.

The Origin of Exchange Energy

For ordered magnetic states to exist at all, it is necessary that the Coulomb energy between two electrons on an atom is greater than the kinetic energy (hopping) of electrons moving between atoms. If this were not the case then electrons are free to move from spin-up to spin-down states, resulting in a nonmagnetic metal. The direct exchange of electrons between two atoms can be calculated from the exchange matrix elements

$$\mathcal{J}_{ij} = \int \phi^*(r - r_i)\phi(r - r_j)\frac{e^2}{|r - r'|}\phi^*(r' - r_j)\phi(r' - r_i)\mathrm{d}r\mathrm{d}r' \tag{2.3}$$

where $\phi^*(r - r_i)\phi(r - r_j)$ is the overlap charge density, essentially the charge in the overlap of electronic wave functions from adjacent atoms. These matrix elements multiply the fermion field operators ($a^\dagger$, a) involved in the exchange of electrons between atomic sites

$$\mathcal{H} = \frac{1}{2}\sum_{ij}\mathcal{J}_{ij}\left(a^\dagger_{i\uparrow}a^\dagger_{j\uparrow}a_{i\uparrow}a_{j\uparrow} + a^\dagger_{i\downarrow}a^\dagger_{j\downarrow}a_{i\downarrow}a_{j\downarrow} + a^\dagger_{i\uparrow}a^\dagger_{j\downarrow}a_{i\downarrow}a_{j\uparrow} + a^\dagger_{i\downarrow}a^\dagger_{j\uparrow}a_{i\uparrow}a_{j\downarrow}\right) \tag{2.4}$$

This can be cast in terms of spinors to give the Coulomb interaction energy[29]

$$\mathcal{E} = -\frac{1}{4}\sum_{ij}\mathcal{J}_{ij}\left(1 + \sigma_i \cdot \sigma_j\right) \tag{2.5}$$

It is important to note however that $\mathcal{J}_{ij}$ may only ever be positive, which means that direct exchange gives rise to ferromagnetic ordering only (Fig. 2.3). Antiferromagnetic

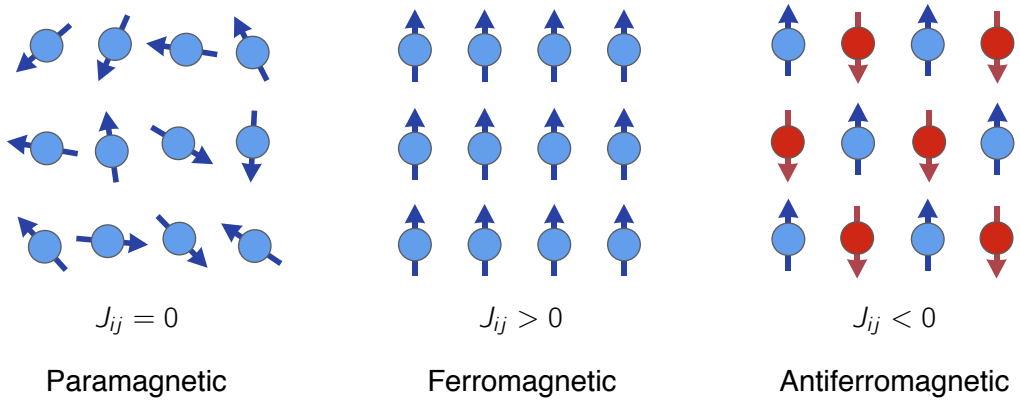

Figure 2.3 | Effect of the Heisenberg exchange. With no exchange energy and no applied field moments are randomly oriented and the material is *paramagnetic*. With a positive value of Heisenberg exchange ($J_{ij} > 0$) moments order in the same direction and the material is *ferromagnetic*. A negative value of Heisenberg exchange ($J_{ij} < 0$) causes moments to order into opposite sublattices known as *antiferromagnetic* order.

ordering arises due to virtual hopping between sites (a perturbation) where one must consider both the direct Coulomb interaction, U, between the electrons and hopping matrix elements b_{ij} of the electrons

$$b_{ij} = \int \phi^*(r - r_i)\mathcal{H}\phi(r - r_j)\mathrm{d}r \tag{2.6}$$

The proper perturbation treatment of this integral gives the virtual hopping energy[29]

$$\mathcal{E} = \frac{1}{2}\sum_{ij}\frac{|b_{ij}|^2}{U}\left(\sigma_i \cdot \sigma_j - 1\right) \tag{2.7}$$

Equations (2.5) and (2.7) can be combined to give the Heisenberg Hamiltonian

$$\mathcal{H}_{\text{Heisenberg}} = -\sum_{ij} J_{ij}\mathbf{S}_i \cdot \mathbf{S}_j \tag{2.8}$$

where J_{ij} is the effective exchange energy between classical spin vectors i and j. This energy can be positive or negative, leading to ferro or antiferromagnetic ordering respectively (Fig. 2.3). As a point of fact, the Heisenberg term is the first order interaction energy between spins and higher order interactions can be derived by considering the interaction of more than two electronic wavefunctions. In the majority of magnetic systems, the higher order terms are orders of magnitude smaller in energy than the Heisenberg term. However there are some materials[30], where higher order interactions must be considered to give the correct ground state and dynamics. In chapter 6, we will consider a Hamiltonian for FeRh with a higher order effective four

spin interaction.

Magnetisation

In experiments it is usually not possible to resolve moment at an atomic level. Instead what is observed is the magnetisation

$$\mathbf{M} = \frac{1}{N}\sum_{i}^{N}\mathbf{S}_i \tag{2.9}$$

At non zero temperatures the overall order of the system is reduced. This is due to the competition between the thermal energy and the exchange energy, leading to disorder in the spin lattice. In an antiferromagnet it is the staggered magnetisation which gives the measure of order. This is calculated as the difference between the sublattice magnetisations and is called the Néel vector

$$\mathbf{L} = \frac{1}{N_A}\sum_{i}^{N_A}\mathbf{S}_i^A - \frac{1}{N_B}\sum_{i}^{N_B}\mathbf{S}_i^B \tag{2.10}$$

As the thermal energy increases the order parameter reduces continuously until it reaches zero. This point is called the Curie temperature (or Néel temperature for AF) as illustrated in figure 2.4. This is a second order phase transition and the magnetic system now becomes paramagnetic because the thermal energy exceeds the exchange energy.

The application of femtosecond lasers to magnetic materials causes a rapid heating which may be above the Curie temperature. This is why ASD is an appropriate method to be used, as the micro-canonical ensemble of the spin degrees for freedom allows a good approximation of phase transitions such as the ferromagnetic-paramagnetic transition. Correctly modelling the behaviour close to this phase transition is vital for the accurate description of ultrafast thermal magnetisation processes.

The Generalised Heisenberg Hamiltonian

The Heisenberg Hamiltonian can be written in a more general sense by including the possibility of the exchange between atomic sites being non-isotropic. The exchange

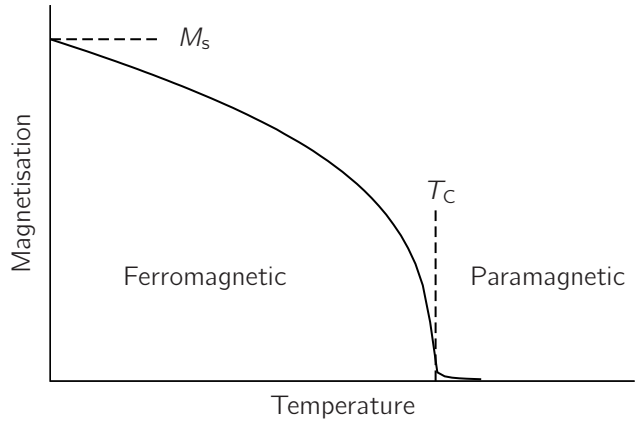

Figure 2.4 | Example magnetisation curve. At zero temperature the magnetisation is saturated (M_s) and all moments are aligned. Increasing temperature causes fluctuations in the alignment of each moment, reducing the magnetisation order parameter. At the Curie temperature (T_C) a phase transition occurs and the material becomes paramagnetic.

Hamiltonian can then be written in terms of a general exchange energy tensor

$$\mathcal{H}_{\text{exc}}\left(\{\mathbf{S}_i\}\right) = -\frac{1}{2}\sum_{i\neq j}\mathbf{S}_i^{\alpha}\mathbb{J}_{ij}^{\alpha\beta}\mathbf{S}_j^{\beta} \tag{2.11}$$

where $\mathbb{J}_{ij}^{\alpha\beta}$ is the where $\alpha, \beta = x, y, z$. The exchange tensor may be broken down into isotropic, symmetric anisotropic and antisymmetric anisotropic components. The isotropic part determines the relative orientation of the spins. A positive value leads to ferromagnetic order and a negative value gives antiferromagnetic order.

$$J_{ij}^{(\text{iso})} = \frac{1}{3}\text{Tr}(\mathbb{J}_{ij}) \tag{2.12}$$

The symmetric anisotropic component is non-zero when there is some favourable direction of alignment of spins, e.g. the z-components may be coupled more strongly due to a two-ion exchange.

$$\mathbb{J}_{ij}^{(\text{sym})} = \frac{1}{2}\left(\mathbb{J}_{ij} - \left(\mathbb{J}_{ij}\right)^{\text{T}}\right) - J_{ij}^{(\text{iso})}\mathbb{I} \tag{2.13}$$

The antisymmetric anisotropic component implies a canting of spins. The origin of this is usually the Dzyaloshinsky-Moriya interaction which is large in some magnetic materials.

$$\mathbb{J}_{ij}^{(\text{anti})} = \frac{1}{2}\left(\mathbb{J}_{ij} - \left(\mathbb{J}_{ij}\right)^{\text{T}}\right) \tag{2.14}$$

Anisotropic exchange can play an important role in some materials such as FePt, where the layered L1_0 structure leads to a two-ion anisotropy and an anisotropic exchange

tensor.

2.3 Magnetic Anisotropy

The exchange interaction determines the relative alignment between spins but does not give any preferential spatial orientation. Yet it is usually the case that magnetic materials have an anisotropic energy landscape in space. The origins of anisotropic terms are numerous and generally the energy contributions are orders of magnitude lower than the exchange energy in ordered magnetic systems. However spatially anisotropic energies determine the ground state to which the magnetisation will relax which is an important property for the technological applications of magnetic materials. In magnetic recording systems it is the bistable orientation of magnetisation which encodes the binary data which is stored.

Magnetocrystalline Anisotropy

Relativistic effects within the crystal lattice lead to an energy landscape which is not homogeneous in space, so it is energetically favourable for the atomistic moments to align to certain directions within the crystal lattice. In bulk materials the 'easy' lowest energy directions usually lie along symmetries in the lattice. In thin films this symmetry is often broken by strains present due to the substrate or capping layer. This can lead to a uniaxial contribution where the magnetisation has two well defined 'easy' directions. The crystal lattice can also contain exchange between different species leading to an apparent anisotropy as is the case with two-ion and super-exchange system.

The first order anisotropy interactions (uniaxial or easy plane) can be written as a self interaction term

$$\mathcal{H}_{\text{anistropy}} = -\sum_{i} \mathbf{S}_i^{\alpha} \mathbb{K}_{ii}^{\alpha\beta} \mathbf{S}_i^{\beta} \tag{2.15}$$

where the anisotropic self interaction tensor is written for the unit vector axis $\hat{\mathbf{e}}$ as

$$\mathbb{K} = K \begin{pmatrix} e_x^2 & e_x e_y & e_x e_z \\ e_x e_y & e_y^2 & e_y e_z \\ e_x e_z & e_y e_z & e_z^2 \end{pmatrix} \tag{2.16}$$

Writing the energy as a self interaction in this way allows the easy combination with Eq.(2.11) when implementing ASD as shown in chapter 3.

Shape Anisotropy

One of the most most complex effects in magnetisation dynamics which effects long length and timescales is that of shape anisotropy. To obey Maxwell's equations, the magnetic field induced from the magnetisation of a magnet must not diverge, in other words it must be flux closed. In mesoscopic magnetic materials it becomes energetically favourable for this flux closure to cause the formation of oppositely polarised magnetic domains. In smaller magnetic nanoparticles the energy required for a domain wall (the intermediate region of spin reorientation between domains) to form is usually large enough that the nanoparticle will retain a single domain wall but still the spin moments will align with lines of flux in the material. In the atomistic picture this can be expressed to a good approximation via a dipole-dipole interaction

$$\mathcal{H}_{\text{dipole}} = -\frac{\mu_s \mu_0}{4\pi a^3} \sum_{i \neq j} \frac{3\left(\mathbf{S}_i \cdot \hat{\mathbf{e}}_{ij}\right)\left(\hat{\mathbf{e}}_{ij} \cdot \mathbf{S}_j\right) - \left(\mathbf{S}_i \cdot \mathbf{S}_j\right)}{r_{ij}^3} \tag{2.17}$$

where r_{ij} is the distance between spins i and j, $\hat{\mathbf{e}}_{ij}$ is the unit vector and a is the lattice parameter. In atomistic dynamics and especially on the sub-picosecond timescale, this energy term is often ignored. The frequency of dipole-dipole interactions is orders of magnitude lower than the exchange contributions and so the effect of dipole-dipole interactions on very short timescales and at high temperatures is negligible.

2.4 Equation of Motion

Landau-Lifshitz Equation

The equation of motion for a classical spin vector was first written down by Landau and Lifshitz[31,32]. It follows from the very simple physical argument that a moment in an applied field will precess about the field. The frequency of precession in this case is determined by the gyromagnetic ratio of an electron, $\gamma = 1.76 \times 10^{11}$ rad·s^{-1}T^{-1}.

$$\frac{\partial \mathbf{S}_i}{\partial t} = -\gamma \left(\mathbf{S}_i \times \mathbf{H}_i\right) \tag{2.18}$$

The effective field, $\mathbf{H}_i$, is considered as the effective field felt locally by a spin on a site, i. This can be found from the relation

$$\mathbf{H}_i = -\frac{\partial \mathcal{H}}{\partial \mathbf{S}_i} \tag{2.19}$$

where one must remember that the Hamiltonian is a function of $\{\mathbf{S}_i\}$ thus equation (2.18) is a coupled set of equations through the effective field.

2.5 Energy Dissipation

One of the main advantages of atomistic spin dynamics is the ability to represent the effects of temperature, something which is very difficult to do from an ab-initio or micromagnetic approach. When applying thermal energy to a system, we must remember that this is not an isolated, closed system. There are extra degrees of freedom within materials which we do not usually model in ASD but the energy dissipation to these must be accounted for. This damping can be split into two groups; direct and indirect[27].

Direct damping is the energy transfer to external degrees of freedom such as phonons. Indirect damping results from energy transfer occurring within the magnetic system. This is the excitation of spin waves, which in themselves act as an energy reservoir. The common energy transfer channels are shown in figure 2.5.

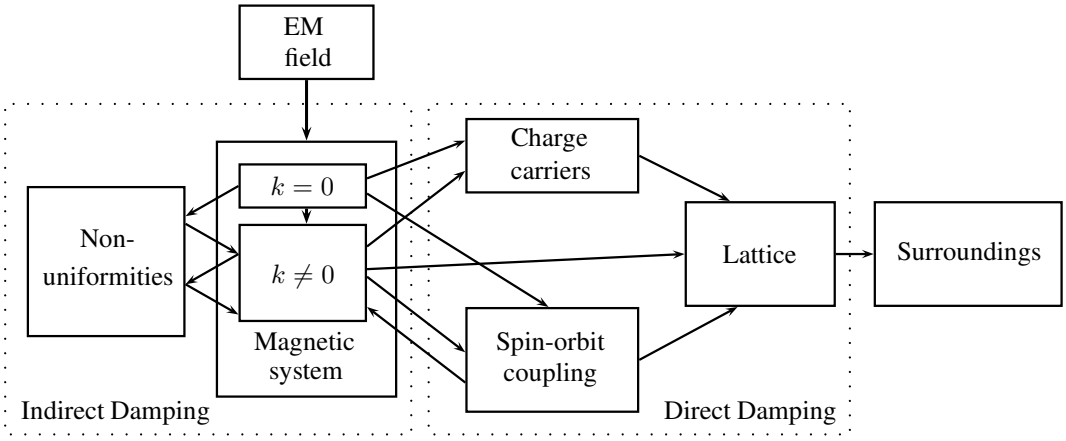

Figure 2.5 | Energy flow between thermal reservoirs. Direct damping occurs when energy and angular momentum are transfered to external degrees of freedom. Indirect damping occurs when the energy and angular momentum are transfered to non-linear ($k \neq 0$) modes. Figure adapted from Ref. 33.

Landau-Lifshitz-Gilbert (LLG) Equation

In ASD energy dissipation or damping is usually included empirically, by the inclusion of a damping term into the Landau-Lifshitz equation (2.18). There are several different

ways in which such damping can be included, the most commonly used was written by Gilbert to be valid for both high and low damped regimes[34,35].

The damping term may be included in a very general way by the inclusion of a Rayleigh dissipation functional into the Lagrangian of the system[35].

$$\mathcal{R} = \frac{1}{2}\sum_{i,j}\int\int\left[\frac{\partial \mathbf{S}_i(\mathbf{r},t)}{\partial t}\cdot\Lambda_{ij}(\mathbf{r},\mathbf{r}')\cdot\frac{\partial \mathbf{S}_j(\mathbf{r}',t)}{\partial t}\right]d\mathbf{r}d\mathbf{r}'. \tag{2.20}$$

where $\Lambda_{ij}(\mathbf{r},\mathbf{r}')$ is the dissipation tensor which is non-local in general. However, due to the inability to measure anisotropic or non-local damping experimentally, it is usual to simplify the dissipation to a local scalar. It is interesting to note that there have been recent advances in the calculation of the dissipation tensor from first principle techniques[36–39]. In the future it may be possible to improve the ASD modelling and indeed multiscale modelling by using such techniques with a fully parameterised dissipation tensor in the ASD equation of motion.

In this work we consider the usual case of scalar Gilbert damping which can be written

$$\frac{\partial \mathbf{S}_i}{\partial t} = -\gamma\mathbf{S}_i\times\left(\mathbf{H}_i - \Lambda\frac{\partial \mathbf{S}_i}{\partial t}\right) \tag{2.21}$$

This equation can be expanded into what is commonly called the Landau-Lifshitz-Gilbert equation

$$\frac{\partial \mathbf{S}}{\partial t} = -\frac{\gamma}{(1+\alpha^2)\mu_s}\left(\mathbf{S}\times\mathbf{H} + \alpha\mathbf{S}\times\mathbf{S}\times\mathbf{H}\right) \tag{2.22}$$

where α is the dimensionless Gilbert damping parameter. This parameter is material dependent but is often found to be quite small, of the order of 0.001. In some materials it can be much larger, for example in FePt, a technologically important material, $\alpha = 0.1$ and in FeRh, a metamagnet, which will be discussed later in this thesis, some measurements give $\alpha = 0.3$. Although it is important to note that the value of α obtained from experimental measurements can vary depending on the technique used, the reasons for this are still under scientific debate.

CHAPTER 3

Implementation

The practical implementation of atomistic spin dynamics contains many interesting problems in itself. For any given problem there are different computational solutions where often there is a trade-off between computational efficiency and the ability to perform calculations in a very general way. Traditionally, long time scale atomistic simulations have been very computationally expensive due to the short time steps required for numerical stability of the underlying stochastic differential equation. Here, atomistic spin dynamics are implemented on a graphical processing unit (GPU), a type of inexpensive but extremely powerful vector processor. The performance this implementation provides has allowed much of the work presented in this thesis to become tractable where previously the calculation time would have been prohibitive. This section details how atomistic spin dynamics have been implemented in a very general but efficient way for computation on either a conventional CPU or a GPU.

3.1 The Landau-Lifshitz Langevin Equation

One of the main advantages of simulations on an atomistic scale is that the statistical ensemble of spins allows accurate sampling of the partition function even for finite temperatures. In more macroscopic approaches such a micromagnetics, the exchange approximation is used and spins are considered co-linear on a length scale proportional to $\sqrt{K/J}$. At high temperatures, such an approach is invalid because the magnetisation of each discrete volume cannot decrease. Thus for the temperature regimes accessed by laser heating, an atomistic approach is well suited. In Monte-Carlo simulations on an atomistic scale, the sampling of microstates is weighted by a

Boltzmann factor which accounts for the thermal energy. i.e. Monte-Carlo moves are accepted with a probability

$$P = \exp\left(-\frac{\Delta E}{k_{\mathrm{B}}T}\right) \tag{3.1}$$

where ΔE is the energy difference before and after the trial move, k_{B} is the Boltzmann constant and T is the temperature in Kelvin. However, Monte-Carlo approaches do not give the dynamics of processes where the inclusion of thermal energy is complicated because it is the resultant trajectories which must sample the Boltzmann thermal distribution. One of the most common, empirical methods of including thermal effects into dynamical equations is the use of a Langevin equation. This adds thermal perturbations to the forces in the equation of motion approximating that the dynamics of the heat bath are unimportant on the time scale of the dynamics. With this separation of time scales it is only the statistical properties which are important[40]. The Langevin equation is written into the field term of each spin as

$$\mathbf{H}_i(t) = -\frac{\partial \mathcal{H}}{\partial \mathbf{S}_i} - \eta \int_{-\infty}^{t} \varphi(t-t')\frac{d\mathbf{S}_i}{dt'}dt' + \boldsymbol{\xi}_i(t) \tag{3.2}$$

where $\varphi(t-t')$ is a memory kernel describing the autocorrelation function of the spin with respect to time. This memory acts with a strength η and $\boldsymbol{\xi}$ is a stochastic term which represents the agitating thermal forces. On short time scale the spin dynamics are most effected by the electron heat bath and the separation of time scales between atomic moments and electron dynamics has already been made in the Heisenberg model. From the central limit theorem the stochastic term, $\boldsymbol{\xi}$, can be approximated as a white noise term (uncorrelated in time and space) with a strength determined from fluctuation dissipation theory[41] with moments

$$\begin{aligned} \langle \xi_{i,a}(t) \rangle &= 0 \\ \langle \xi_{i,a}(t), \xi_{j,b}(t') \rangle &= 2k_B T \eta \varphi(|t-t'|)\delta_{ij}\delta_{ab} \end{aligned} \tag{3.3}$$

where i and j are lattice sites; a and b are Cartesian components. The first moment being zero means that there is no directional bias in the stochastic term. In the second moment the delta function δ_{ij} defines the stochastic term to be local, so the thermal perturbation on any given lattice site is uncorrelated with respect to the other lattice sites. This is an approximation because only spin degrees of freedom are considered and no attempt is made to simulate the phonon or electronic systems which may cause spatial correlations between lattice sites. The delta function δ_{ab} defines the stochastic term to be diagonal, that is to say there is no correlation between the spin components. While it is possible that the thermal noise is correlated between Cartesian components,

the difficulty in measuring such an effect means there has been no study of this, also indicating that such effects are small. The coupling constant η is a single variable encapsulating the strength of coupling between the spin degrees of freedom and the effective external heat bath degrees of freedom. The memory convolution is non-linear in the equation of motion and therefore allows energy dissipation and η is a damping constant. From the Langevin equation (Eq.(3.2) and (3.3)) an equation can be derived with coloured noise, meaning the memory kernel $\varphi(t-t')$ has some time dependence. In the work presented the white noise limit will be used, which reduces the memory kernel to the Markovian limit $\varphi(t-t') = \delta(t-t')$. Including the field from the Langevin equation into the Landau-Lifshitz equation (2.18), the LLG equation (2.22) is recovered, where now the effective field felt by a spin includes the stochastic term $\boldsymbol{\xi}(t)$. This is called the Landau-Lifshitz-Gilbert Langevin equation (LLG-L).

Mathematically, white noise is generated by a Wiener process[41] which is simulated numerically by generating pseudo-random numbers from a Gaussian distribution of width

$$\sigma = \sqrt{\frac{2\alpha k_{\mathrm{B}} T}{\gamma \mu_s \Delta t}} \tag{3.4}$$

The inclusion of the time step Δt on the denominator is due to the inclusion of the stochastic term within the effective field. A Wiener process in fact, scales with time as $\sqrt{\Delta t}$ but numerical integration as discussed in the next section already includes a factor Δt so after the integration the scaling of the Wiener process will be correct with the moments of the random variables corresponding to Eq. (3.3) where $\varphi(t-t') = \delta(t-t')$.

The Ito-Stratonovich Dilemma

In the field of stochastic calculus, there are two main interpretations of integration, Ito and Stratonovich calculus. The difference between these is in the choice of where intermediate points are chosen along the path of integration. Considering an integral as the limit of a series of Riemann sums

$$x_n = \sum_{i=1}^{n} B(\tau_i)[W(t_i) - W(t_{i-1})] \tag{3.5}$$

where τ_i are the intermediate points $t_{i-1} \leq \tau_i \leq t_i$, then the result is dependent on the choice of τ because the continuous random process is being sampled at different points in time[41]. In physics it is most common to use the Stratonovich interpretation which

samples the random process at the starting point of each step. Using this interpretation means stochastic integration is treated in a similar way to ordinary integration (with a Riemann integral) and important in the physical sense is that causality is implied and obeyed. The Ito interpretation involves sampling the random process at the midpoint and usually results in a drift term which is not present in the Stratonovich solution. In the case of atomistic spin dynamics it has been shown that as long as the spin vector is of a conserved length, the Ito and Stratonovich solutions coincide[42]. This is because in a Heisenberg model there can be no drift term in the solution meaning that the two stochastic integrals coincide for both interpretations. Therefore this dilemma needs consideration only in situations where the length of the spin vector is allowed to change which is not considered in this work although has been considered by others[43].

The Heun Method

One of the simplest integration schemes which can be applied to the stochastic LLG-L equation is the Heun scheme. In fact, the Heun scheme is derived for deterministic ODEs (see Kloeden & Platen [44, p.487]) but for SDEs the extension is trivial due to its equivalence to the second order Runge-Kutta scheme which does have a form derived for SDEs[45]. In the literature it has become common place to refer to the Heun method for the integration of SDEs also. Two trial steps are made, one from the initial state and a second from an Euler step (Fig. 3.1). The average of the two results gives the result.

$$\mathbf{S}(t+\Delta t) = \mathbf{S}(t) + \frac{1}{2}\left[\frac{\partial \mathbf{S}(t)}{\partial t} + \frac{\partial \tilde{\mathbf{S}}(t+\Delta t)}{\partial t}\right]\Delta t \tag{3.6}$$

$$\tilde{\mathbf{S}}(t+\Delta t) = \mathbf{S}(t) + \frac{\partial \mathbf{S}(t)}{\partial t}\Delta t \tag{3.7}$$

There are several important considerations for the application of the Heun scheme. First is that the effective fields $\mathbf{H}_{\text{eff}}$ must be updated for both the prediction and correction steps. However by definition the stochastic term for both of these calculations must be the same. The Heun scheme is non-conservative, meaning the numerical error in the integration leads to an artificial drift in the length of the spin vectors. It is important both for numerical stability and to represent the Heisenberg Hamiltonian correctly, that $|\mathbf{S}_i| = 1$, therefore after each integration step the spin magnitude must re-normalised to unity.

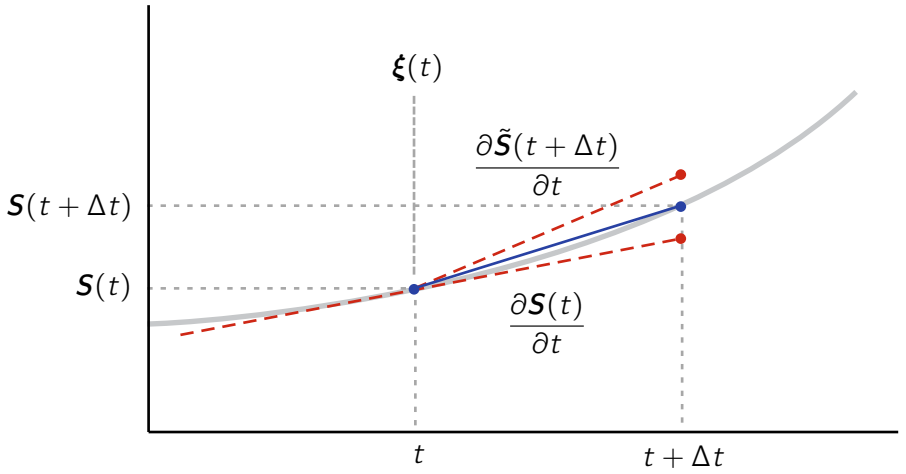

Figure 3.1 | Diagram of the Heun method. An initial estimation is made from the current gradient and a second estimation is made based on the gradient of an Euler step. The average of these two lines then defines the Heun step. The stochastic term, $\boldsymbol{\xi}(t)$ is evaluated only once at the start of the integration step.

Modelling Laser Heating

In this work the ability to model the heating effect of femtosecond laser pulses is required. A large amount of energy is deposited into the material in a very short space of time and so the different heat reservoirs are pushed out of equilibrium. The heat reservoirs of most relevance are those of the spin, electron and phonon systems. The spin heat bath is directly simulated by the ASD modelling. Energy is stored in spin wave modes which vary with time and equilibrate with the other thermal reservoirs via the stochastic fields and Gilbert damping. The electron and phonon heat baths are not directly simulated but the temperature of the electronic and phonon heat baths can be modelled in a so-called two-temperature model, where heat is initially deposited in the electron heat bath from the laser and then equilibrates thermodynamically with the phonon heat bath[46,47]. This is described by

$$C_e \frac{dT_e}{dt} = -G_{ep}(T_e - T_p) + P(t) \tag{3.8}$$

$$C_p \frac{dT_p}{dt} = G_{ep}(T_e - T_p) \tag{3.9}$$

Where T_e and T_p are the electron and phonon temperatures, C_e and C_p are the heat capacities and G_{ep} is the electron-phonon coupling. The value of G_{ep} strongly determines the rate at which thermal energy is dispated from the electron system to the phonon heat bath. The electron heat bath is assumed to have a much smaller heat capacity than the phonon heat bath, therefore on short time scales the electron temperature can rapidly increase with the application of a laser pulse as shown in

Fig. 3.2a. The spin system is effected most strongly by the electronic temperature on a picosecond time scale[48], therefore in simulations with a laser heat pulse spin system is coupled to the electron temperature, which in turn is connected to the phonon system (Fig. 3.2b).

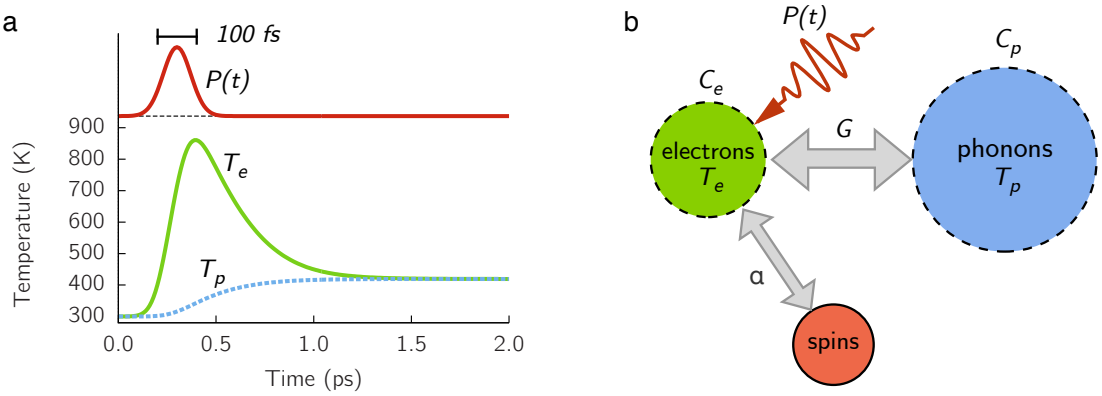

Figure 3.2 | Temperature profiles of the two-temperature model. A Gaussian laser power $P(t)$ heats the electronic system to which the spins are coupled. The small heat capacity of the electronic system (C_e) means this system increases to large temperatures. The coupling to the phonon system removes heat from the electronic system as per the two temperature model (Eq.3.9).

3.2 Interactions in Crystal Lattices

Atomic spin simulations are usually restricted to crystal lattices. Therefore it is desirable to describe such lattices and the interactions between lattice sites with ease. The definition of lattice vectors and motifs can be used to represent the lattice as a set of integer four vectors[49] . This allows interaction matrices to be calculated with ease by integer operations which are much more efficient than real space vectors translations.

The set of lattice vectors $\mathbf{a}$, $\mathbf{b}$ and $\mathbf{c}$ can be defined in a matrix

$$\mathbb{L} = \begin{pmatrix} a_0 & a_1 & a_2 \\ b_0 & b_1 & b_2 \\ c_0 & c_1 & c_2 \end{pmatrix} \tag{3.10}$$

The positions of a lattice site $\mathbf{r}_i$ within space is now given by

$$\mathbf{r}_i - \mathbf{p}_n = \mathbb{L}\mathbf{q}_i \tag{3.11}$$

where $\mathbf{q}$ is a set of integers and $\mathbf{p}$ is the position of a lattice site within the unit cell. Making $\mathbf{q}_i$ the subject, any lattice site can be mapped to an integer unit cell space.

$$\mathbf{q}_i = \mathbb{L}^{-1}\left(\mathbf{r}_i - \mathbf{p}_n\right) \tag{3.12}$$

Thus any lattice site can now be defined by an integer four vector

$$\mathbf{v}_i = \begin{pmatrix} q_{i,0} \\ q_{i,1} \\ q_{i,2} \\ n \end{pmatrix} \tag{3.13}$$

where n enumerates the lattice site within the unit cell, associating it with a certain value of $\mathbf{p}$.

Interactions between lattice sites can now be defined in real space vectors between numbered sites within the motif. Application of the inverse lattice vectors to the interaction vectors gives the integer translation vector $\mathbf{q}$ and n must be specified.

The Interaction Matrix

The interactions between lattice sites can be written in the form of an interaction matrix ($\mathbb{W}_{ij}$) which is composed of 3×3 blocks of each interaction tensor (Eqs. (2.11) and (2.15)). This gives a $3N \times 3N$ matrix which describes the tensorial interaction between any two spins.

$$\mathbb{W}_{ij} = \{\mathbb{J}_{ij}\} + \{\mathbb{K}_{ii}\} \tag{3.14}$$

Using such a matrix the field on each site can be calculated easily from the matrix vector product

$$\mathbf{H}_i = \mathbb{W}_{ij}\mathbf{S}_j \tag{3.15}$$

where $\mathbf{H}_i$ and $\mathbf{S}_j$ are vectors of length $3N$. Note that $\mathbb{W}_{ij}$ is symmetric only if the spin and field vectors are ordered by index and then component, i.e.

$$(\{\mathbf{S}_j\}) = (S_0^x, S_0^y, S_0^z, \cdots, S_{N-1}^x, S_{N-1}^y, S_{N-1}^z) \tag{3.16}$$

Doing so means that only one half of the interaction matrix need be stored to calculate all interactions. If dipole-dipole interactions were included in this matrix, then it would be a dense matrix as every spin interacts with all others. However if this interaction is disregarded, either because only fast time scales are of interest or

because such interactions can be implemented efficiently with other methods, then it is a sparse matrix which is formed. This is because the exchange interaction is usually very limited in distance and often approximated to the nearest neighbour contributions so the majority of elements of $\mathbb{W}_{ij}$ are zero. This drastically reduces the memory required to store the interaction matrix. Even for long range exchange Hamiltonians such as FePt[50] this interaction matrix will be reasonably sparse. How sparse matrices are formed and computations involving them are performed is an interesting computational problem which will be discussed below, especially in the context of GPU computing.

Sparse Matrices

The structure of the sparse interaction matrix will depend on how the lattice sites are numbered during the decomposition of the lattice into the matrix. For a logical numbering of lattice sites such as labelling sequentially by the x, y, z translations of the unit cell, a strongly diagonal matrix is obtained (Fig 3.3). It is possible to choose alternative numbering algorithms which localise the labeling in 3 dimensional space, effectively making the matrix denser along the leading diagonal (known as bandwidth and profile reduction[51]). However any algorithm involves sudden jumps in the numbering between some areas of space which leads to the sparse diagonals seen in the matrix. Periodic boundary conditions cause the small diagonals in the corners of the matrix which can have implications for the speed of the calculations, depending on the format used to store the matrix (Fig 3.3).

3.3 GPU Parallel Acceleration

Graphics processing units (GPUs) are a specialised class of computer hardware that has been aggressively developed in the recent past to render graphics for computer games. This continuous, competitive development has led to hardware that is computationally very powerful, but also very low cost. The GPU architectures which have developed are very specialised to their task of rending 3-dimensional graphics, which involves massive amounts of parallel floating point computation. They are essential massive vector processors, an architecture which was popular in the 1970's and 1980's[52]. In 2007 the existing GPU hardware was made accessible to software developers by NVIDIA using their proprietary CUDA extensions to the C++ programming language. Since then there has been a large interest in using GPUs to accelerate highly parallel

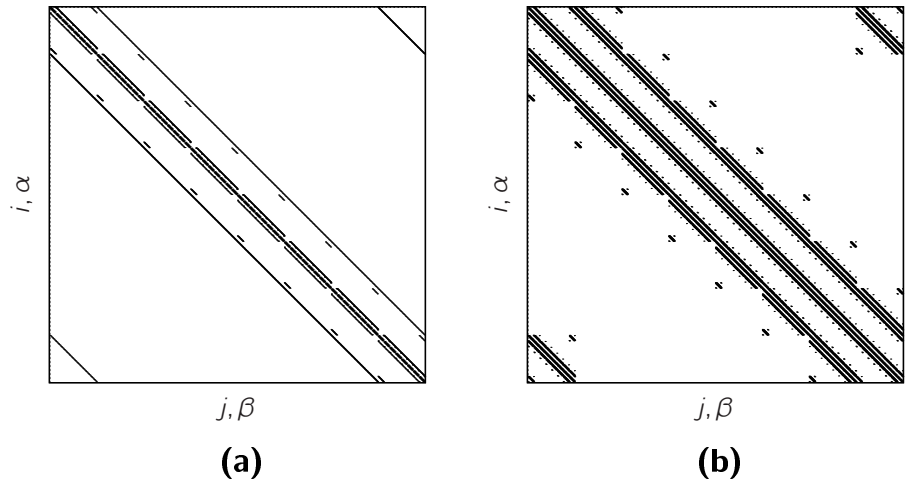

Figure 3.3 | Strongly diagonal decomposed interaction matrices. Both matrices represent simple cubic lattices **(a)** is for a nearest neighbour [001] interactions only. **(b)** contains [001], [011] and [111] interactions. The small corner bands are due to periodic boundary conditions.

parts of scientific calculations. The specialised architecture of a GPU means that algorithms must be employed which can exploit the hardware to the maximum extent. This section focuses on how GPU hardware can be exploited for atomistic spin calculations and the increased performance this leads to.

GPU Architecture

GPUs contain large banks of processing cores connected via a high bandwidth bus to a large amount of high speed memory (see Fig. 3.4 for a comparison with a traditional CPU architecture). This arrangement means that large blocks of memory can be moved onto the array of processors, where each processors would ideally work on one element of that memory. Such a transaction is the most efficient method of using a GPU or indeed a vector processor in general. Although the very latest GPU architecture (Keplar) implements a full cache hierarchy, saturating the very large memory bandwidth of the device will maximise computational through by avoiding idle processing time. To maximise this performance, the underlying algorithms must be analysed to ensure that the algorithm used is well suited to vector computation.

A further consideration is that there is a large difference between the single-precision and double-precision peak processing power due to both the limit of the bandwidth of the memory bus and also there are more single precision units in each multiprocessor

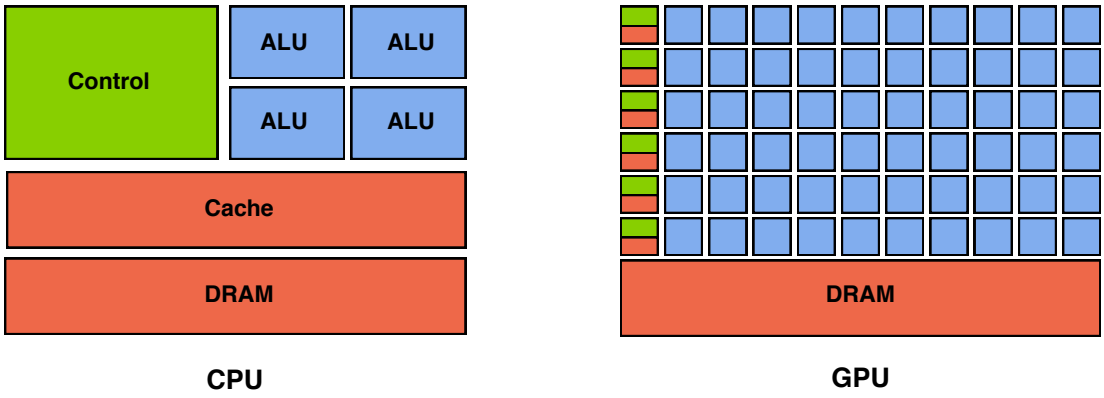

Figure 3.4 | Comparison of CPU and GPU architectures. Conventional CPUs contain a large cache and a small number of arithmetic logic units (ALU), often called 'cores'. Most of the data in memory is stored in DRAM before being moved onto the processor. In a GPU many ALUs share a small cache between them and there are many of these multiprocessor units. On a GPU the memory bus to the DRAM is both larger than on conventional CPUs and the DRAM is faster. (Adapted from Ref. 53)

than double precision units. Therefore to utilise the hardware resources to the maximum extent, some calculations which can be performed in single precision without a loss of accuracy can be identified. It is important that these calculations do not contain compound errors, so for example it would be unwise to implement a single precision integration scheme due to the dependence of each new time step on the previous time step. Within atomistic spin dynamics the field calculation can be implemented in single precision because the interaction matrix elements are constant for the duration of the calculation. By choosing an appropriate normalisation, it is unlikely that the exponent will be overflowed. With regard to the mantissa, generally the exchange and anisotropy energies, even when calculated from first principles, are not more accurate than three or four significant figures.

GPU Numeric Integration

The numeric integration of the LLG equation is straightforward to parallelise on a vector processor. The equation of motion of each spin depends only on its effective field and the spin at the previous time step. The integration of the equation of motion for each spin can therefore be performed independently and the memory can be read in aligned blocks. The computational difficulty arises in the calculation of the effective field which couples the system through the exchange interactions, thus requiring the values for spin vectors from very different areas of the memory.

The effective exchange field is determined by the sparse matrix, vector product

(SpMV) between the interaction matrix and the vector of all spin components (Eq.(3.15)). Parallelising a SpMV product on a vector processor is not trivial. In fact, different sparse matrix storage conventions can be more or less efficient depending on the sparsity pattern of the matrix and the architecture on which it is performed. Bell and Garland[54] have studied the performance of different sparse matrix types on GPUs for different sparsity patterns. Within atomistic spin simulations a lattice based system is usually considered and interactions between lattice sites are of some regular form, for example, nearest neighbour interactions. Furthermore the interaction matrix is constant for the duration of the simulation as lattice sites are fixed. If the interaction motif is decomposed into the sparse matrix in a regular manner, this will yield an interaction matrix composed of diagonal bands (for example Figure 3.3). The memory architecture of a GPU demands that that the very large memory bandwidth is saturated in order to maximise calculations on the vector processor. Here, two common sparse matrix schemes; compressed sparse row (CSR) and the diagonal (DIA) formats. These formats allow only the non-zero values of the matrix to be stored, thus vastly reducing the memory overhead. However the algorithms which must be used to calculate the SpMV for these formats differ greatly.

Compressed Sparse Row (CSR)

The CSR format stores all of the non-zero elements of the matrix in a contiguous block of memory. A second array is used to store pointers for every column, which point to the first and last elements of each row in the storage matrix. Thus the memory required is minimised by only storing non-zero elements and $N+1$ pointers. For serial calculation, for example a single thread on CPU, the multiplication algorithm is very efficient because the matrix memory is all read in order. This matrix format is used in the *cuSparse* library by NVIDIA. In Fig. 3.5 shows that ASD implemented with a CSR interaction matrix (for nearest neighbour interactions) gives a speedup of $\sim 25\times$ for large systems when compared to an optimised CPU implementation. However the diagonal format can give even better performance.

Diagonal (DIA)

The DIA format stores and calculates every matrix diagonal which contains non-zero elements. Furthermore, each diagonal which is stored is N elements long (where N is one dimension of the matrix). The implications of such a storage method are two fold. Firstly, for diagonals other than the leading diagonal, calculations performed

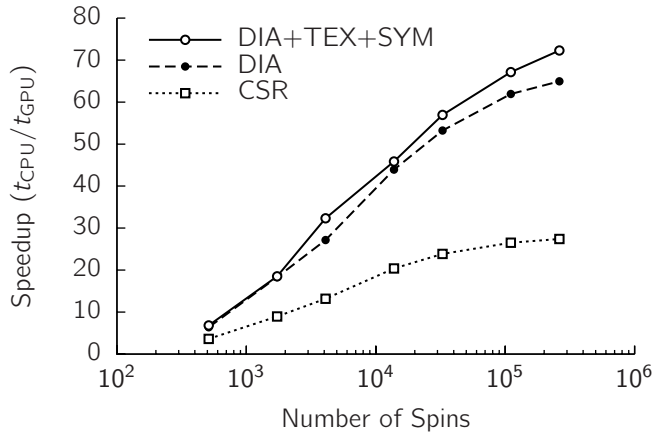

Figure 3.5 | GPU speedup of sparse matrix storage types. The speedup is measured relative to the CSR CPU implementation. The test hardware was a quad-core Intel i5 2.66GHz processor, 4GB RAM and NVIDIA 570GTX GPU. DIA+TEX+SYM is the final implementation where texture memory is used to allow some caching and the symmetric matrix calculation is performed to reduce the memory footprint.

beyond the extent of the matrix must be discarded. Secondly, storing some zero values increases the memory footprint of this method, although an array of pointers is not needed, just the offset of each diagonal. For calculation on a serial CPU a DIA implementation would be slower than a CSR implementation because it must perform (or preemptively discard) calculations of zero elements and elements not within the array. This means there will be jumps in the program control which are not beneficial for caching. On a GPU however, the constant size of each diagonal and the inclusion of zero elements on the diagonals means that all memory transactions are aligned and large continuous blocks can be read thus saturating the large bandwidth of the memory bus. Some calculations are still discarded, although for strongly diagonal matrices this is minimal, but the large number of processing units means that this has less of an impact on the net performance of the SpMV calculation. The results in Fig. 3.5 show a speedup of over $65\times$ in comparison to the CPU CSR implementation for large systems and a factor of $\sim 2.5\times$ greater than the GPU CSR implementation. Implementing caching by the use of special features such as texture memory and exploiting the symmetric nature of our matrix, performance can be increased slightly.

3.4 Conclusions

Implementing ASD on a GPU achieves speedups of greater than $75\times$ verses that of an optimised serial CPU implementation. Such a large increase in performance

allows the simulation of systems which would not previously have been possible on a reasonable time scale. These problems may involve either extremely large systems or very long time scales, or even be able to tackle both situations at once. Finite size effects can cause markedly different behaviour in small systems, realtive to the bulk, so for comparison of experimental and analytical work, the closer simulations can be to the thermodynamic limit the more valid the comparison. The GPU implementation developed within this thesis was used throughout the work presented. For example, in simulating systems of GdFeCo, a random lattice model requires a large system, of the order of millions of spins, to properly sample localised topological differences. The ability to simulate long time scales to calculate equilibrium properties, even at high temperature, to a high degree of accuracy for comparison with analytic methods is also enhanced by use of a GPU enabled ASD.

CHAPTER 4

Spin Waves

Akin to phonons in mechanical lattice dynamics, spin lattices also possess elementary excitations called magnons which describe the quantised excitation of the spin degrees of freedom. Generally when a magnon is created, it is delocalised across the lattice leading to a spin wave[55,56]. In the classical regime that which is considered in ASD, spins are not quantised but can continuously deviate around the unit sphere. Even so, the movement of a spin away from its ground state is an excitation which is delocalised via the interactions within the spin lattice[33]. Thus spin waves still exist in the classical regime and play an important role in the thermal and non-equilibrium behaviour of magnetic materials.

4.1 Classical Spin Waves

A classical spin wave is a periodic variation in the orientation of spins, away from their ground state, from one lattice site to the next. Spin waves can exist in both transverse (acoustic) and longitudinal (optical) modes. Transverse modes exist as a phase shift between adjacent spins leading to a variation of angle between each spin and its ground state as shown in figure 4.1. In a transverse mode the projection of the spin onto the ground state orientation is equal for all spins. Optical modes are the contrasting case of a sinusoidal variation in the projection of a spin onto the ground state, for example if the ground state is $S_z = 1$ then a sinusoidal variation in S_z is an optical mode. Optical modes are usually only found in materials which contain antiferromangetic or other non-trivial ordering resulting from interactions between spins which are not collinear in the ground state. Optical modes are usually higher in frequency than acoustic modes.

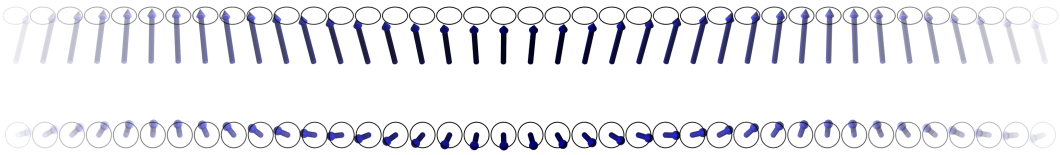

Figure 4.1 | Spin waves. The excess energy of excitations is delocalised by a phase shift across the spin lattice. This results in a spin wave.

Spin waves can also exist on very long length and time scales, for example in Yttrium Iron Garnet (YIG), spin waves can be observed with wavelengths on a μm scale with life times of seconds in part due to the low damping in this material[57]. This type of spin wave originates from magnetostatic forces, the propagation of magnetic fields through the material and free space as described by Maxwell's equations. The magnetostatic field is given by

$$\mathbf{H}(\mathbf{r}) = \int_S \frac{(\mathbf{r}-\mathbf{r}')\mathbf{M}(\mathbf{r}')\cdot\hat{\mathbf{n}}}{|\mathbf{r}-\mathbf{r}'|^3} dS - \int_V \frac{(\mathbf{r}-\mathbf{r}')\nabla\cdot\mathbf{M}(\mathbf{r}')}{|\mathbf{r}-\mathbf{r}'|^3} dV \tag{4.1}$$

where the first integral is over the surface and $\hat{\mathbf{n}}$ is a surface normal, the second integral is over the volume of the magnet. From this equation it is clear that there are long range interactions across the entire magnetic material. There is also a strong shape dependence to this field which can be highly non-trivial. The study of magnetostatic spin waves is usually restricted to micromagnetic length scales and will not be considered in the following work.

Spin waves also provide a channel for energy dissipation within magnetic materials. Direct damping, represented by the Gilbert damping in the atomistic LLG equation results from spin waves scattering with non-magnetic degrees of freedom, transferring energy and angular momentum out of the spin system[58]. Typically this would occur via channels such as scattering with phonons and charge carriers. In some materials spin-orbit coupling also plays a large role in energy dissipation[33]. There also exists an indirect damping within the spin lattice. Energy and angular momentum is transferred between spin wave modes within the lattice. The non-uniform spin wave modes act as another energy and angular momentum reservoir. Energy losses can occur when energy is transferred from the $k = 0$ mode to $k \neq 0$ modes, where nonlinear effects dissipate the energy[33,58].

The study of spin waves is especially important in ultrafast spin dynamics for several reasons. The high level of heating caused by the femtosecond laser takes the spin system close to or through the Curie temperature. In this regime nonlinear spin wave

effects become large, meaning that there is a strong energy transfer between spin wave modes in contrast to low temperatures where there is a superposition of linear modes. Related to this is the fact that the heat is applied so quickly that the spin system enters a non-equilibrium regime. Spin wave excitations exist outside of the equilibrium distribution for a finite life time, in effect storing energy and angular momentum which will be dissipated some time after the heat pulse.

4.2 Linear Spin Wave Theory

At low temperatures, $T < 0.75T_{\mathrm{C}}$, linear spin wave theory (LSWT) can be applied, which assumes that interactions between spin waves are small and the dynamics are dominated by the weighted superposition of the thermal distribution of independent spin wave modes. At higher temperatures the non-linear terms of the Landau-Lifshitz equation start to dominate causing energy transfer between different spin wave modes which are considered in the next section.

To give a brief outline of LSWT a simple Hamiltonian can be considered

$$\mathcal{H} = -\sum_{\langle ij \rangle} J_{ij} \mathbf{S}_i \cdot \mathbf{S}_j \tag{4.2}$$

Ignoring direct damping the equation of motion can be written using the Landau-Lifshitz equation

$$\frac{d\mathbf{S}}{dt} = \mathbf{S} \times \left(\sum_j J_{ij} \mathbf{S}_j \right) \tag{4.3}$$

which is a set of N non-linear equations. Writing the spins as the mean thermal value plus some deviation from the ground state ($\delta \mathbf{S}_i$)

$$\mathbf{S}_i = \langle \mathbf{S}_i \rangle + \delta \mathbf{S}_i \tag{4.4}$$

This implies a low temperature regime where spins will not be excited too far from the equilibrium. Transforming into Fourier space allows the use of the lattice symmetry to reduce the system of equations. The Fourier components of the spins can be defined as

$$\mathbf{S}_{\mathbf{k}} = \frac{1}{\sqrt{N}} \sum_i \mathrm{e}^{\mathrm{i}\mathbf{k}\cdot\mathbf{r}_i} \mathbf{S}_i \tag{4.5}$$

and the mean field approximation now becomes

$$\mathbf{S}_{\mathbf{k}} = \langle \mathbf{S} \rangle \delta(\mathbf{k} = \mathbf{0}) + \delta \mathbf{S}_{\mathbf{k}} \tag{4.6}$$

The Fourier transform of the exchange term is written as

$$J_{ij} = \sum_{\mathbf{k}} \mathrm{e}^{\mathrm{i}\mathbf{k}\cdot(\mathbf{r}_i - \mathbf{r}_j)} J_{\mathbf{k}} \tag{4.7}$$

This term depends on the interactions and will differ between lattices due to the interaction vector $\mathbf{r}_i - \mathbf{r}_j$. Thus the equation of motion is now written

$$\frac{d}{dt} \begin{pmatrix} \delta S^x_{\mathbf{k}} \\ \delta S^y_{\mathbf{k}} \\ \delta S^z_{\mathbf{k}} \end{pmatrix} \approx (J_0 - J_{\mathbf{k}}) \begin{pmatrix} 0 \\ 0 \\ \langle S \rangle \end{pmatrix} \times \begin{pmatrix} \delta S^x_{\mathbf{k}} \\ \delta S^y_{\mathbf{k}} \\ \delta S^z_{\mathbf{k}} \end{pmatrix} \tag{4.8}$$

$$\frac{d}{dt} \begin{pmatrix} \delta S^x_{\mathbf{k}} \\ \delta S^y_{\mathbf{k}} \\ \delta S^z_{\mathbf{k}} \end{pmatrix} \approx (J_0 - J_{\mathbf{k}}) \langle S \rangle \begin{pmatrix} -\delta S^y_{\mathbf{k}} \\ \delta S^x_{\mathbf{k}} \\ 0 \end{pmatrix} \tag{4.9}$$

This can be rewritten in terms of spin raising and lowing operators.

$$\frac{d}{dt} \begin{pmatrix} \delta S^x_{\mathbf{k}} + \mathrm{i}\delta S^y_{\mathbf{k}} \\ \delta S^x_{\mathbf{k}} - \mathrm{i}\delta S^y_{\mathbf{k}} \\ \delta S^z_{\mathbf{k}} \end{pmatrix} \approx -(J_0 - J_{\mathbf{k}}) \langle S \rangle \begin{pmatrix} \delta S^y_{\mathbf{k}} - \mathrm{i}\delta S^x_{\mathbf{k}} \\ \delta S^y_{\mathbf{k}} + \mathrm{i}\delta S^x_{\mathbf{k}} \\ 0 \end{pmatrix} \tag{4.10}$$

assuming wave like solutions

$$\delta S^+_{\mathbf{k}}(t) = \delta S^+_{\mathbf{k}}(0) \mathrm{e}^{-\mathrm{i}\omega_{\mathbf{k}} t} \tag{4.11}$$

$$\delta S^-_{\mathbf{k}}(t) = \delta S^-_{\mathbf{k}}(0) \mathrm{e}^{+\mathrm{i}\omega_{\mathbf{k}} t} \tag{4.12}$$

$$\delta S^z_{\mathbf{k}}(t) = \delta S^z_{\mathbf{k}}(0) \tag{4.13}$$

the equation of motion is solved

$$\begin{pmatrix} \delta S^+_{\mathbf{k}} \\ \delta S^-_{\mathbf{k}} \\ \delta S^z_{\mathbf{k}} \end{pmatrix} \approx -\mathrm{i}(J_0 - J_{\mathbf{k}}) \langle S \rangle \begin{pmatrix} -\mathrm{i}\omega_{\mathbf{k}} & 0 & 0 \\ 0 & \mathrm{i}\omega_{\mathbf{k}} & 0 \\ 0 & 0 & 0 \end{pmatrix} \begin{pmatrix} \delta S^+_{\mathbf{k}} \\ \delta S^-_{\mathbf{k}} \\ \delta S^z_{\mathbf{k}} \end{pmatrix} \tag{4.14}$$

Thus the dispersion relation is found to be

$$\omega_{\mathbf{k}} = -(J_0 - J_{\mathbf{k}}) \langle S \rangle \tag{4.15}$$

At low temperature this describes the spin wave spectrum, where $\langle S \rangle$ is the mean spin value, effectively the magnetisation.

4.3 Dynamic Structure Factor

Using atomistic spin dynamics spin wave dispersion can be calculated directly. Such a result includes spin wave-spin wave interactions therefore allowing comparison between analytic methods and approximations. In ASD the spin wave spectrum is calculated from the dynamic structure factor[†] (DSF)

$$\mathcal{S}\left(\mathbf{q},\omega\right) = \frac{1}{\mathcal{N}\sqrt{2\pi}} \sum_{\mathbf{r},\mathbf{r}'} \mathrm{e}^{\mathrm{i}\mathbf{q}\cdot\left(\mathbf{r}-\mathbf{r}'\right)} \int_{-\infty}^{+\infty} \mathrm{e}^{\mathrm{i}\omega t}\, C\left(\mathbf{r}-\mathbf{r}',t\right) \mathrm{d}t \tag{4.16}$$

where $C\left(\mathbf{r}-\mathbf{r}',t\right)$ is the spin-spin space-time correlation function

$$C\left(\mathbf{r}-\mathbf{r}',t\right) = \langle S_{+}(\mathbf{r},t) S_{-}(\mathbf{r}',0) \rangle \tag{4.17}$$

$\langle \cdots \rangle$ denotes a thermal average and $S_{\pm}(\mathbf{r},t) = S_x(\mathbf{r},t) \pm \mathrm{i}S_y(\mathbf{r},t)$ are the usual spin raising and lowering operators. Equation (4.16) is the scattering function which is measured in Brillouin scattering experiments of spin waves[59,60], thus it also gives a direct link to experimentally observable results.

The DSF can be calculated in ASD by the space and time discrete Fourier transforms of the spin lattice.

$$\mathcal{S}\left(\mathbf{q},\omega\right) = \mathrm{FT}_{(t)}\left[\mathcal{W}(\mathrm{FT}_{(\mathbf{r})}\left[S_{+}(\mathbf{r},t)S_{-}(\mathbf{r},t)\right])\right] \tag{4.18}$$

where $\mathcal{W}(t)$ is a Hamming windowing function in the time domain

$$\mathcal{W}(t) = 0.54 - 0.46\cos\left(\frac{2\pi t}{\tau - 1}\right) \tag{4.19}$$

and τ is the total time of the time series. ASD is usually concerned with periodic lattices which is therefore commensurate with the periodic nature of the Fourier transform in the spacial domain. However the behaviour in the time domain is not strictly periodic, primarily due to the stochastic Langevin term and also the arbitrary truncation of the time series. Therefore a windowing function must be applied to reduce spectral leakage from the sharp cut-off of frequencies which are not periodic

[†]Some literature refers to this as the dynamic scattering function.

in the sampled time. Windowing functions weight the sampled data, reducing towards zero at the edge of the sampled time. In this work the common Hamming windowing function is used. The Hamming window aims to optimise the central lobe of the power spectrum. This allows the relevant frequencies to be extracted accurately, although a small error maybe introduced into the measured linewidths. The discrete measurement made in ASD is therefore

$$\tilde{\mathcal{S}}\left(\mathbf{q},\omega\right)=\frac{1}{\tau}\frac{1}{\mathcal{N}\sqrt{2\pi}}\sum_{\mathbf{r},\mathbf{r}'}\mathrm{e}^{\mathrm{i}\mathbf{q}\cdot\left(\mathbf{r}-\mathbf{r}'\right)}\sum_{t=0}^{\tau-1}\mathrm{e}^{\mathrm{i}\omega t/\tau}\ \left[\mathcal{W}(t)\cdot C\left(\mathbf{r}-\mathbf{r}',t\right)\right] \tag{4.20}$$

The sampling time of the temporal Fourier transform gives the frequency cutoff of the DSF with $\omega_{\max}=\pi/\Delta t$. The windowing function avoids any aliasing of higher frequency modes. If the spin lattice is not periodic then a type of windowing must also be performed in the spatial transform. This is usually performed by zero padding whereby the lattice is doubled in all dimensions with the new sites taking zero values, effectively using a crude vacuum to separate images of the lattice in Fourier space.

Comparing LSWT and atomistic spin dynamics

The DSF is calculated for a prototypical material and compared with the LSWT result. This allows the implementation of the DSF in calculating the spin wave dispersion to be validated and also tests the limits of LSWT against a more complete thermal description of the spin waves. BCC Fe is used as the prototype material with the parameters listed in table 4.1.

Curie Temperature	T_{C}	1043K	Ref. 23
Exchange Energy	J_{ij}	6.92×10^{-21}J	
Anisotropy Energy	d_z	3.1×10^{-24}J	Ref. 23
Moment	μ_{s}	$2.2\mu_{\mathrm{B}}$	Ref. 61
Lattice Parameter	a	0.287nm	Ref. 61
Gilbert Damping	α	0.0014	Ref. 62

Table 4.1 | Parameters used for the atomistic model for BCC Fe. References are given to the experiments determining the value. The exchange energy is chosen to give the correct Curie temperature in the model.

After calculating the DSF from atomistic spin dynamics the spin wave dispersion can be extracted by fitting a Lorentzian to the peak along each q-vector. As a single species ferromagnet the band structure for BCC Fe shows a single band in the dispersion. In

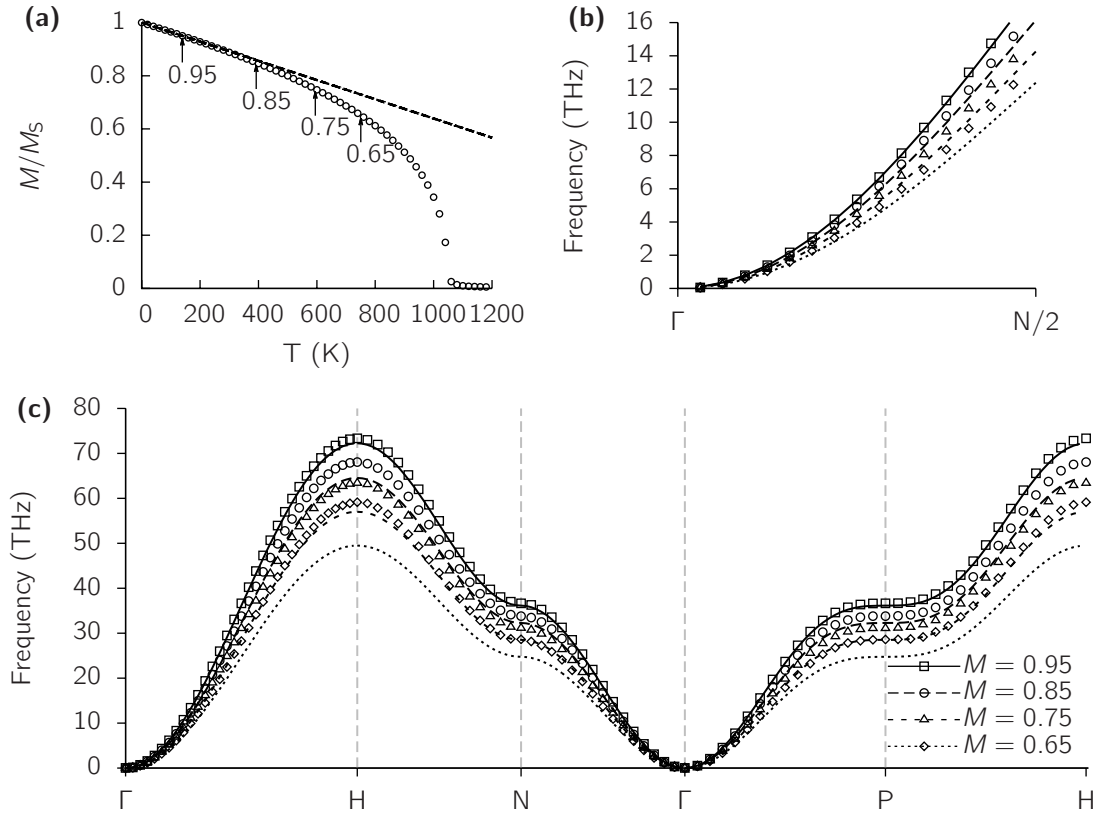

Figure 4.2 | LSWT at finite temperatures. **(a)** As the temperature increases the magnetisation deviates more from the linear regime. **(b)** At short wave-vectors (long length scales) the LSWT is still a reasonable approximation. **(c)** At the edge of the Brillouin zone (short length scales) the LSWT is very poor at describing the dispersion relation.

figure 4.2 the ASD calculated DSF is compared LSWT for decreasing magnetisation, which is a measure of the magnon density in the lattice. In a classical Heisenberg FM, the low temperature, linear regime is where the magnetisation decreases linearly with temperature (Fig. 4.2a). Beyond this linear regime is where magnon-magnon interactions become important and linear spin wave theory breaks down as shown in Fig. 4.2 a and b. At the edge of the Brillouin zone the frequencies obtained from LSWT are consistently lower than those calculated from ASD (Fig.4.2c). The reason for the poor agreement is that neither LSWT or ASD in its current form are well suited to represent such short wavelengths[14,63]. Therefore ASD cannot be used to benchmark spin wave theories at high frequencies. In order to account for magnon-magnon interactions, formalisms beyond linear spin wave theory must be considered.

4.4 Beyond Linear Spin Wave Theory

To consider higher order interactions and therefore higher temperatures, a different formalism must be used. For classical dynamical equations the classical spectral density method (CSDM) can be used and indeed has been applied to magnetic systems previously[64–66]. In this formalism the equation of motion of an ensemble of spins is solved self consistently in the Fourier (spectral) domain assuming some form of the spectral function, usually represented by a delta function[64–66]. There are still some open questions the CSDM approach especially in how the longitudinal spin-spin correlation function is determined. This is the issue considered here by comparing the results of different methods with ASD.

The CSDM dispersion relation for a simple FM with uniaxial anisotropy is written[64]

$$\omega_{\mathbf{k}} = h + \frac{1}{N^2}\sum_{\mathbf{k}}\left[(-2k + J_{\mathbf{k}} - J_{\mathbf{p}-\mathbf{k}})\langle s^+_{\mathbf{k}} s^-_{-\mathbf{k}}\rangle + 2(2k + J_{\mathbf{k}} - J_{\mathbf{p}-\mathbf{k}})\langle s^z_{\mathbf{k}} s^z_{-\mathbf{k}}\rangle\right] \tag{4.21}$$

where $\langle s^+_{\mathbf{k}} s^-_{-\mathbf{k}}\rangle$ and $\langle s^z_{\mathbf{k}} s^z_{-\mathbf{k}}\rangle$ spin-spin correlation functions in Fourier space for the transverse and longitudinal components respectively. The transverse correlation function can be calculated from

$$\langle s^+_{\mathbf{k}}(\tau) s^-_{-\mathbf{k}}\rangle = T\int_{-\infty}^{\infty}\frac{d\omega}{2\pi}\frac{\Omega_{\mathbf{k},-\mathbf{k}}(\omega)}{\omega}\mathrm{e}^{-\mathrm{i}\omega\tau} \tag{4.22}$$

assuming the spectral function is a delta function, and in the static case ($\tau = 0$), giving[64]

$$\langle s^+_{\mathbf{k}} s^-_{-\mathbf{k}}\rangle = \frac{2mNk_{\mathrm{B}}T}{\omega_{\mathbf{k}}}. \tag{4.23}$$

The longitudinal correlation function, $\langle s^z_{\mathbf{k}} s^z_{-\mathbf{k}}\rangle$, is more difficult to calculate because it cannot be expressed simply in terms of the spectral density function $\Omega_{\mathbf{k}}(\omega)$ but must come from the solution of further expressions which depend on $\langle s^+_{\mathbf{k}} s^-_{-\mathbf{k}}\rangle$. The way in which the longitudinal-transverse correlation is decoupled is somewhat arbitrary and an analysis of the commonly used expressions will be the focus of the work in this section. The spectral density is now written in the form

$$\omega_{\mathbf{k}} = h + m\left(2k + J_0 - J_{\mathbf{k}}\right) + \alpha(m)\frac{m}{\beta N}\sum_{\mathbf{p}}\frac{-2k + J_{\mathbf{p}} - J_{\mathbf{k}-\mathbf{p}}}{\omega_{\mathbf{p}}} \tag{4.24}$$

where it is the third term which incorporates magnon-magnon interactions. The strength of this term is dependent on the magnetisation through the decoupling function

$\alpha(m)$ which approximates higher order spin-spin correlation. The magnetisation must be calculated self consistently with Eq. (4.24). It has been shown that the correct high and low temperature behaviour is given with the magnetisation written as[64]

$$m^2 = \frac{1 - 3m\Omega}{1 - m\Omega} \tag{4.25}$$

where Ω is the thermal sum of the spectral density

$$\Omega = \frac{1}{N} \sum_{\mathbf{k}} \frac{1}{\beta\omega_{\mathbf{k}}} \tag{4.26}$$

The simultaneous, self consistent solution of equations (4.24) and (4.26) gives the equilibrium magnetisation and spin wave dispersion at an arbitrary temperature.

Decoupling Schemes

The derivation of the CSDM requires the decoupling of transverse and longitudinal correlation functions. There is no exact way to do this and different decoupling schemes exist within the literature, essentially performing the decoupling to higher orders in a perturbation series. It is not clear *a priori* which decoupling scheme produces the most physically correct results. In fact in different limits and for different Hamiltonians the agreement may be better or worse for different schemes. A typical Hamiltonian of exchange and uniaxial anisotropy is studied and the correct reproduction of the macroscopically observable quantities such as the temperature dependence of magnetisation, anisotropy and exchange stiffness are the quantities of importance. This is due to the role CSDM plays in multiscale modelling, allowing micromagnetic models to be constructed from first principles calculation without the need to perform computationally expensive atomistic spin dynamics to obtain these temperature dependant values [66].

In the classical limit, the decoupling schemes differ by their magnetisation dependence of the magnon-magnon interactions (the third term in Eq.(4.24)) as follows

$\alpha(m) = 0$	RPA	
$\alpha(m) = m$	Callen	Ref. 67
$\alpha(m) = m^3$	Copeland and Gersch	Ref. 68
$\alpha(m) = m + m^3$	Swendsen	Ref. 69

Table 4.2 | Spin-spin correlation decoupling schemes

Notice that in the RPA magnon-magnon interactions are not taken into account, yet this differs from mean field theory because the magnetisation is calculated taking into account the spectral density (Eq. (4.25)).

In reproducing the temperature dependence of the magnetisation, there are two main features which should be reproduced as accurately as possible. The first is to calculate the Curie temperature and the second is that the critical behaviour close to the Curie temperature is well reproduced. This is where magnon-magnon interactions play a dominant role. The CSDM is compared with different decoupling schemes to the LLG Langevin equation which will include magnon-magnon interactions of all orders. This does not measure the physical correctness of the CSDM for any given material as the Heisenberg model implemented in the ASD approach is still subject to its own inherent approximations. However the ASD provides a reference thermodynamical model of the same Hamiltonian as the CSDM to benchmark against. The CSDM treats the spin as a classical quantity and therefore magnetic materials that display a more quantum characteristic behaviour (i.e. the quantisation of spin plays a strong role in the thermal properties) should instead be modelled using a quantum approach such as a quantum Green's function technique [70]. However, in the quantum case, the same decoupling schemes are still required.

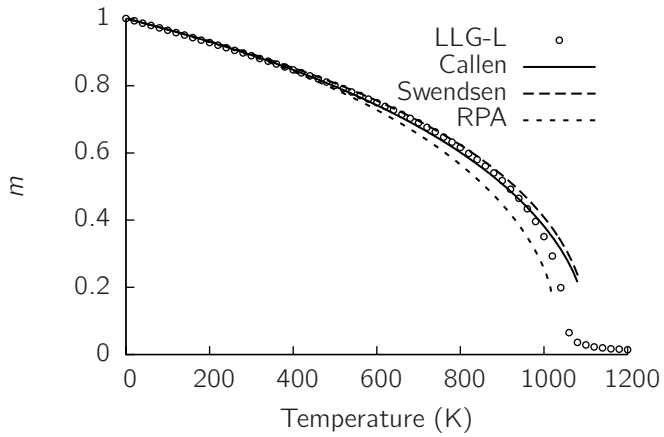

Figure 4.3 | Comparison of magnetisation for different decoupling schemes. The magnetisation calculated self consistently for BCC Fe parameters with RPA, Callen and Swendsen decoupling schemes (lines), compared to the magnetisation calculated from ASD (circles).

The self consistent magnetisation (Fig. 4.3) shows that the RPA underestimates T_{C} due to the lack of higher order terms that exist in the other schemes. The Callen and Swendsen decouplings result in the same T_{C} as each other, but overestimate T_{C} with respect to the ASD results. However, the inclusion of magnon-magnon interactions with these decoupling schemes results in a much better approximation

of the high temperature magnetisation than the RPA. The Swendsen overall gives the closest agreement to the ASD approach. By studying the self consistent spectrum in comparison to that obtained via the DSF (Eq. (4.20)) in the ASD approach more insight can be gained into why the Swendsen scheme is superior in this region.

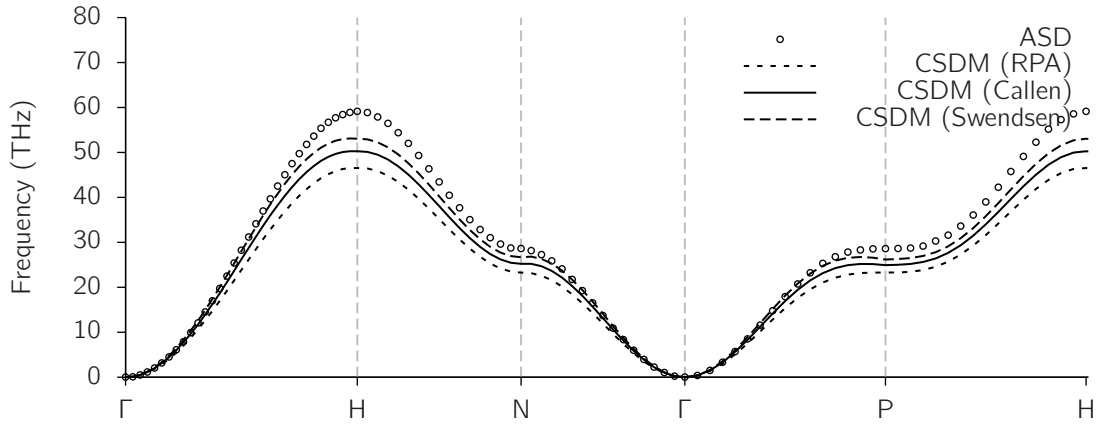

Figure 4.4 | Comparing CSDM, LSWT and LLG-L at T=750 K. The CSDM results are closest to the LLG-L result especially on longer length scales which dominate the macroscopic dynamics. The Swendsen decoupling scheme renders a very good approximation of the dispersion across much of the Brillouin zone, differing only in the very high frequencies where the time scale approximations of atomistic spin dynamics become spurious.

In figure 4.4 the data shows that the Swendsen scheme best reproduces the ASD spin wave spectrum across the majority of the Brillouin zone, even at high temperature. Hence why the magnetisation is reproduced best in this decoupling scheme. Focusing on long length scales close to the Γ-point (Fig. 4.5, the results show that the Callen scheme is actually superior in this limit. It is length scales greater than the exchange length ($\sqrt{(2A/\mu_0 M_s^2)}$ which is typically 3-10nm) which are important for micromagnetics and so the accuracy of the Callen scheme in this limit has important implications for multiscale modeling as shown below. At the highest frequencies at the edge of the Brillouin zone, the agreement between the analytic results (LSWT and CSDM) and ASD is quite poor. It is hard to draw strong conclusions in this regime as to the correctness of any approach. At such high frequencies the time scale approximations made by atomistic spin dynamics (chapter 2) are spurious, the electronic time scales and the spin wave frequencies become close enough to question the adiabatic approximation.

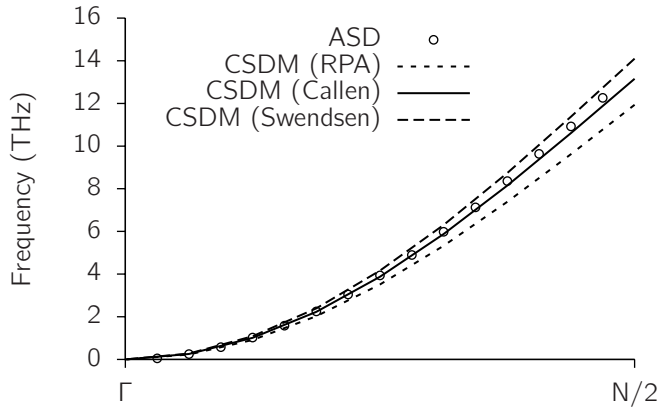

Figure 4.5 | Comparing CSDM, LSWT and LLG-L at T=750 K for long length scales. The Callen decoupling scheme agrees well with the LLG-L on long length scales. As the wave vector increases, the Swendsen scheme becomes a better representation.

Temperature Dependent Micromagnetic Parameters

The high temperature behaviour of magnetic materials has become more important as hard drive companies attempt to exploit the temperature dependent magnetic properties for applications such as HAMR. Device level modelling is typically done through micromagnetics due to the relatively large length and time scales which are of interest. Typical micromagnetic approaches using the LLG equation cannot represent the high temperature effects of a material because the magnetisation is kept constant in a discrete volume according to the exchange approximation. This is valid at low temperature where the angle between neighbouring spins would be small as the system is dominated by long wavelength modes. At high temperature it is the disorder of the spins which leads to the phase transition at the Curie point and there is no way for LLG micromagnetics to represent this. Newer formalisms such as the Landau-Lifshitz-Bloch (LLB) equation are capable of representing high temperature magnetism, through and even above the Curie temperature, by allowing the length of the magnetisation vector to change in a given volume. Micromagnetism, whether LLG or LLB based, requires the temperature dependent form of several parameters which can include; the equilibrium magnetisation $m_e(T)$, longitudinal susceptibility $\chi_{\parallel}(T)$, transverse susceptibility $\chi_{\perp}(T)$, anisotropy $K(T)$ and exchange stiffness $A(T)$. These can be parameterised from experiment or in a mean field, however to perform true multiscale modelling, these should be calculated on the basis of *ab initio* calculations of the anisotropy energy and Heisenberg exchange constants. In the past ASD has been used for the intermediate stage to calculate the micromagnetic parameters from ab initio calculations, giving far superior results than mean field

results[71]. The downside to this approach is that such atomistic simulations can be very computationally expensive, especially in the case that the ab initio results indicate that many neighbouring spins are involved in the exchange. Therefore it would be preferable to use the CSDM to obtain the thermodynamic parameters from an ab-initio calculation of the atomistic scale properties.

Exchange stiffness temperature scaling

The exchange stiffness, $A(T)$, can be calculated from the CSDM by fitting to the self consistent spectrum ω_k. For a ferromagnet the dispersion relation is[33]

$$\omega_{\mathbf{k}} = \gamma A(T) \frac{(J_0 - J_{\mathbf{k}})}{J_0} \tag{4.27}$$

At low temperatures this form fits the spectrum very well. However at high temperatures, approaching the Curie point, the fit across the Brillouin zone becomes worse due to the increase in magnon-magnon interactions. In micromagnetics is the longer length scales which are modelled, of the order of the exchange length. Therefore the fitting is limited to this regime, close to the Γ-point.

In the CSDM the equation is derived assuming a delta function for the spectral density, but in the ASD the complete spectrum including the line width which results from the direct (Gilbert) and indirect damping is obtained. So a two stage fit must be performed, firstly the peak of the spectrum must be extracted for each k-vector. This is done by fitting a Lorentzian in the frequency domain along each k-vector. The maxima of all the Lorentzians can be fitted to obtain the exchange stiffness. This fitting procedure is demonstrated in Fig. 4.6 where the colour plot is the ASD calculated spectrum, the white points are the maxima from the Lorentzian fitting and the red line is the range-limited fitting of Eq. (4.27).

Performing this fitting procedure for different temperatures the exchange stiffness is extracted as a function of temperature. This is compared to the exchange stiffness as calculated from the CSDM for different decoupling schemes (Fig. 4.7). This is plotted as a function of magnetisation to account for the difference in Curie temperatures between the decoupling schemes and ASD. The Callen decoupling scheme is in very good agreement with the ASD results across the whole magnetisation range. At low temperature the Swendsen scheme does not agree well with the ASD, but towards the higher temperature regime this also is in good agreement, possibly more so than the Callen scheme. This is reflected also in the magnetisation where the

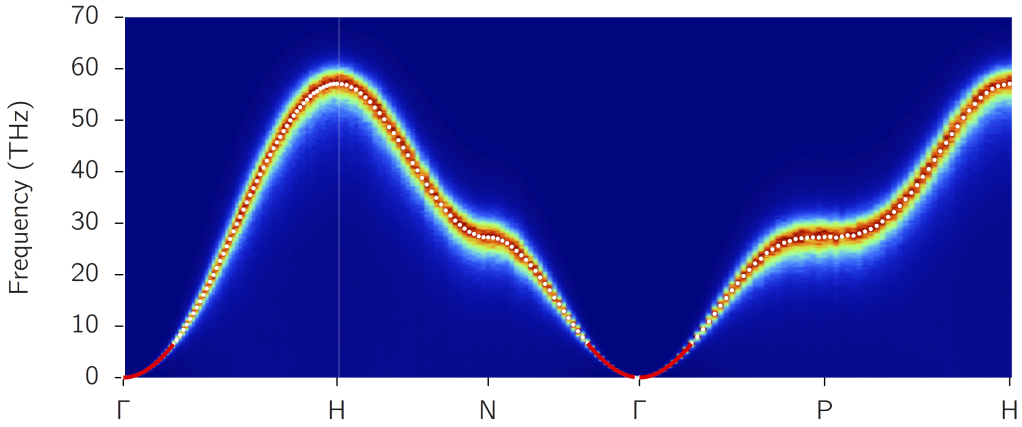

Figure 4.6 | Fitting the exchange stiffness from the DSF. The white dots give the peak of the Lorentzian fitted along each k-vector. The exchange stiffness is then found by fitting the equation (4.27) in the long wavelength regime marked as a red line.

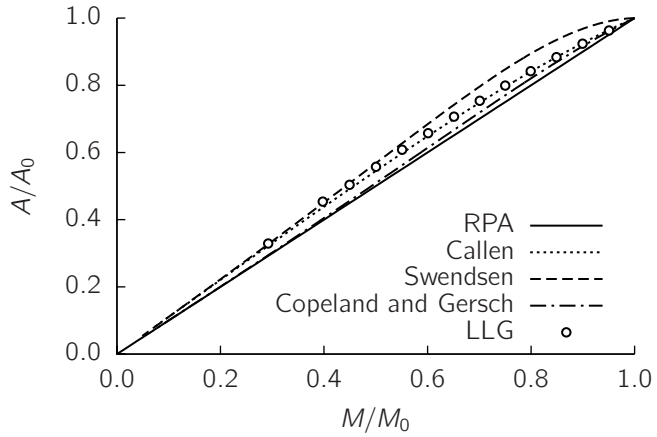

Figure 4.7 | Exchange stiffness comparison of decoupling schemes. Comparing different decoupling schemes with the LLG.

Swendsen scheme reproduces the form of the magnetisation best as the Curie point is approached (Fig. 4.3). The results echo what was seen in the comparison of the spectrum from ASD and for the different decoupling schemes (Fig. 4.5) in that the Callen scheme reproduces the the spectrum with increased accuracy over the other decoupling schemes.

Anisotropy temperature scaling

The anisotropy field is typically of GHz in frequency and the discrete Fourier transform used for the DSF gives a resolution which is too low to give an accurate value of the anisotropy. Instead the value of the effective anisotropy, $K(T)$, is extracted by fitting

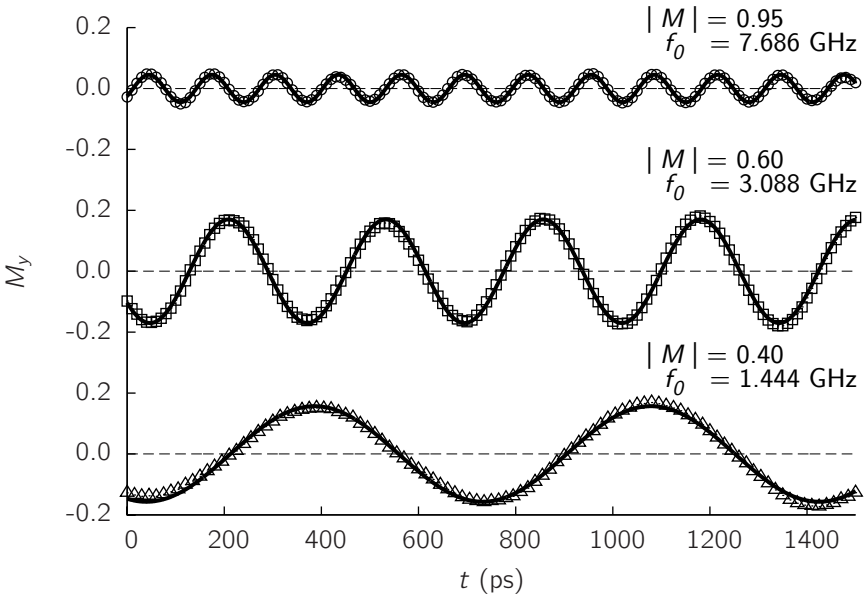

Figure 4.8 | Fitting effective anisotropy. The low damping means a small line width and the FMR frequency can be fitted well even at low magnetisation (high temperature).

to the ferromagnetic resonance of the magnetisation. The low Gilbert damping of Fe ($\alpha = 0.02$) means that the FMR mode is very well defined (small line width). There are other novel techniques which can be used to calculate the anisotropy numerically such as constrained Monte-Carlo[72], however such methods cannot be constructed experimentally. The magnetisation is fitted by

$$M_y = a_0 \sin(2\pi f_0 + \varphi_0) \tag{4.28}$$

to find the FMR frequency which is then related to the anisotropy as $f_0(T) = 2|\gamma|K(T)/2\pi$. The low FMR frequency means that the system must be integrated for a long time, especially as $K(T)$ reduces as a function of temperature, so the FMR frequency reduces also. Integration is performed for 1.5ns (after equilibration) for each temperature. This long time scale is only tractable with the use of GPUs as described in section 3. Example data and fitting is shown in Fig. 4.8. Even at high temperature ($|M| = 0.40$ corresponds to $\sim 0.92T_c$) the FMR frequency is well defined and the fit is quite accurate.

In figure 4.9 the ASD results are compared for different decoupling schemes in the CSDM. In the low temperature regime the Callen scheme reproduces the ASD results reasonably well, but at high temperature this becomes less so. At high temperatures the Swendsen scheme is closest to the ASD results, but the functional form is quite dissimilar. A line of M^3 scaling is plotted, which is the low temperature exponent

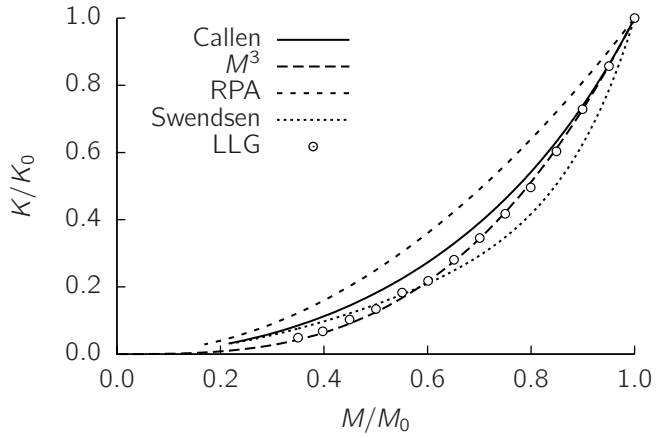

Figure 4.9 | Comparison of decoupling schemes with anisotropy. The Callen scheme gives the best agreement with the anisotropy scaling, especially at low temperatures. However a scaling of M^3 appears to most closely describe the scaling.

of the Callen decoupling and the experimentally observed uniaxial anisotropy scaling exponent[73] . This scaling is identical to the ASD results, even very close to T_c. The same conclusions have been drawn for a lower temperature range with other methods such as constrained Monte Carlo[72].

4.5 Conclusions

Comparing macroscopic, thermodynamic functions from ASD and CSDM using different decoupling schemes, the results show that the Callen decoupling scheme is generally the most compatible in the micromagnetic length scale. The scaling of the exchange stiffness is very well reproduced by the Callen scheme even though the Swendsen decoupling gives a closer comparison with the magnetisation. This appears to be because the Callen scheme produces a more accurate spin wave spectrum ω_k in the low k vectors than the Swendsen scheme which better describes ω_k across the range of k. Because micromagnetic properties are important on length scales $\sim \sqrt{K/J}$ the Callen scheme is more suited for calculating micromagnetic parameters. In calculating the unaxial anisotropy scaling exponent, the Callen scheme only reproduced the magnetisation scaling well in the low magnetisation regime. At high temperatures none of the decoupling schemes gives a good reproduction of the anisotropy scaling. The scaling is found to be M^3 across almost the whole temperature range.

This chapter also confirms the correctness of the spin dynamics implementation used within this thesis. Testing the implementation of a complicated method such as ASD is

hard to do in general terms. The reproduction of the important observable parameters from a system and the close agreement with the low temperature spin wave spectrum in the linear spin wave limit are strong evidence that the implementation is correct in the dynamical and stochastic aspects.

CHAPTER 5

Enhanced damping at ferromagnet - antiferromagnet interfaces

The coupling of ferromagnetic (FM) and antiferromagnetic materials is extensively used in devices. In constructions such as spin valves, the FM reference layer is pinned by the strong anisotropy of the coupled AF. Interesting magnetic effects exist in coupled FM/AF layers, for example exchange bias[74]. It has also been found that there is an enhancement of the Gilbert damping in the FM layer of FM/AF coupled devices[75,76]. This is surprising due to the large difference in the frequency of the uniform modes between FM and AF materials. The precise mechanism for the enhancement of the damping is not known. The increase in damping is shown to be a result of the excitation of a local mode within the AF to which it is coupled. This acts as an energy sink to which the FM can dissipate energy. The material parameters which effect the strength of the additional damping are identified. The insight provided will allow the tuning of the performance characteristics in spin valves and other devices.

5.1 Background

Several experiments have shown that in FM-AF bilayers there is an enhanced damping of the FM layer. Smith *et al.*[76] measured the damping of each layer in a spin valve stack (Fig. 5.1a). The pinned layer, which is a ferromagnet coupled an antiferromagnetic layer, showed $10\times$ the effective damping of the free layer, a FM layer not strongly exchange coupled to any other layers but of similar composition to the pinned FM layer. Therefore the increase in damping was attributed to the coupling to the AF.

Weber *et al.* performed MOKE measurements across an FM/AF bilayer, where the AF layer was in the form of a wedge with an increasing thickness across the sample (Fig. 5.1b). They found a larger FM damping with increasing thickness of the AF[75]. These experiments cannot be explained in terms of a resonant coupling of the FM and AF layers because in an FM the uniform mode is quite low frequency, depending only on the anisotropy field, $\omega_0 = \gamma H_{\mathrm{ani}}$ whereas in the AF, the exchange field plays a role, $\omega_0 = \gamma\sqrt{H_{\mathrm{ani}}(2H_{\mathrm{exc}} + H_{\mathrm{ani}})}$ which causes the uniform mode to be orders of magnitude larger than that of a FM. In the study by Weber *et al.* the results may be explained by the number of AF grains participating in the exchange bias due to the polycrystalline nature of the sample[77]. Also in the study by Smith *et al.* thermal activation in the AF may be a cause, due to the current being passed through the devices. However in this work an alternative mechanism will be investigated which is suggested in the conclusion of both studies.

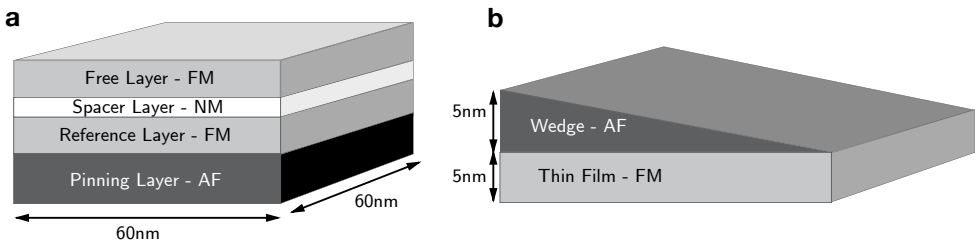

Figure 5.1 | AF/FM experiments investigating Gilbert damping. **a** A spin valve contains two FM layers magnetically decoupled with a nonmagnetic (NM) spacer layer. The magnetisation of the reference layer is held in the same direction by exchange coupling to the AF layer. The free layer has nominally the same makeup as the reference layer but experiments has observed an enhanced damping in the reference layer of $\sim 10\times$ that of the free layer[76]. **b** MOKE measurements of a wedge geometry have found that the damping of the FM layer increases with the increasing AF thickness[75].

5.2 Analytic Model

A better understanding of this phenomenon is useful for two reasons. By understanding the factors which are important in the energy transfer, devices may be tailored to have a higher or lower rate of damping where beneficial. There is also the interesting potential to probe the properties of the AF, where such experiments may be difficult to perform without the use of the coupled FM. We study a simple FM/AF bilayer first from an analytic description, where the AF is described in an atomistic sense[78,79]. This allows energy to propagate through the AF from the interface. Such a description allows us to go beyond a simple coherent spin model and allows non collinearity through the AF.

We approximate the FM to be coherent and represent it as a single macrospin. Thin films will generally have a large magnetostatic contribution to the energy, causing the magnetisation to lie in-plane. We simplify this contribution to an in-plane anisotropy term in the FM. The FM macrospin is coupled at the interface to the first of a ladder of atomic AF spins. Each AF spin is then coupled to AF spins above and below as well as having a uniaxial anisotropy aligned in the plane (see Fig. 5.2). The energy of this system is described as

$$\begin{aligned}\mathcal{E} = &- \tilde{J}(\mathbf{s}_0 \cdot \mathbf{m}) + J\left[(\mathbf{s}_0 \cdot \mathbf{s}_1) + (\mathbf{s}_1 \cdot \mathbf{s}_2) + \cdots + (\mathbf{s}_{N-1} \cdot \mathbf{s}_N)\right] \\ &+ \frac{\bar{K}}{2} m_x^2 - \frac{K}{2}\left[s_{0,z}^2 + s_{1,z}^2 + \cdots + s_{N,z}^2\right]\end{aligned} \tag{5.1}$$

where $\tilde{J}$ is the FM/AF exchange coupling strength divided by the number of FM atomic planes, $\bar{K}$ is the FM hard axis energy, J is the AF exchange strength, K is the AF uniaxial exchange anisotropy and N is the number of layers in the AF.

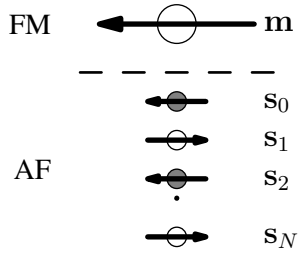

Figure 5.2 | FM/AF bilayer configuration. The system under consideration consists of a FM macrospin coupled to a simple layer-wise bulk AF of atomic spins.

In the linear approximation, $m_z \approx 1 - \frac{1}{2}(m_x^2 + m_y^2)$ and so the energy of the interfacial AF spin, s_0 is written

$$\mathcal{E}_{s_0} = -\tilde{J}(m_x s_{0,x} + m_y s_{0,y}) - \tilde{J} s_{0,z} + \frac{\tilde{J}}{2} s_{0,z}(m_x^2 + m_y^2) + J(\mathbf{s}_0 \cdot \mathbf{s}_1) - \frac{K}{2} s_{0,z}^2 \tag{5.2}$$

Now expressing the AF in terms of Holstein-Primakoff like operators

$$\begin{aligned} s_z &= s - \hat{a}^\dagger \hat{a}; \quad s_x = \sqrt{\frac{s}{2}}(\hat{a} + \hat{a}^\dagger); \quad s_y = \mathrm{i}\sqrt{\frac{s}{2}}(\hat{a}^\dagger - \hat{a}) \quad \text{for} \quad s = 0, 2, 4, \cdots \\ s_z &= -s + \hat{b}^\dagger \hat{b}; \quad s_x = \sqrt{\frac{s}{2}}(\hat{b} + \hat{b}^\dagger); \quad s_y = \mathrm{i}\sqrt{\frac{s}{2}}(\hat{b} - \hat{b}^\dagger) \quad \text{for} \quad s = 1, 3, 5, \cdots \end{aligned} \tag{5.3}$$

where $\hat{a}$ and $\hat{b}$ are used for even and odd AF layers respectively. The energy terms for

s_0 are written as

$$\begin{aligned}\mathcal{E}_{s_0} =& -\tilde{J}\sqrt{\frac{s}{2}}\left[(\hat{a}_0+\hat{a}_0^\dagger)m_x+\mathrm{i}(\hat{a}_0^\dagger-\hat{a}_0)m_y\right]-\tilde{J}(s-\hat{a}_0^\dagger\hat{a}_0)\\&+\frac{\tilde{J}}{2}(s-\hat{a}_0^\dagger\hat{a}_0)(m_x^2+m_y^2)+Js\hat{a}_0^\dagger\hat{a}_0+Js\left(\hat{a}_0^\dagger\hat{b}_1^\dagger+\hat{a}_0\hat{b}_1\right)-\frac{K}{2}(s-\hat{a}_0^\dagger\hat{a}_0)^2\end{aligned} \tag{5.4}$$

The equation of motion follows from $\mathrm{i}\partial\hat{a}_n/\partial t=[\hat{a}_n,\mathcal{E}]$ (taking $\hbar=1$) and keeping terms only linear in $(\hat{a}_0^\dagger\hat{a}_0)$ and $(m_x^2+m_y^2)$ giving

$$\mathrm{i}\frac{\partial}{\partial t}\hat{a}_0=\left(\tilde{J}+Js+Ks\right)\hat{a}_0+Js\hat{b}_1^\dagger-\tilde{J}\sqrt{\frac{s}{2}}(m_x+im_y) \tag{5.5}$$

For the bulk AF layers the energy is written

$$\begin{aligned}\mathcal{E}_{s_n} =& (2Js+Ks)\sum_{n=1}^{\frac{N-1}{2}}\left(\hat{a}_{2n}^\dagger\hat{a}_{2n}+\hat{b}_{2n-1}^\dagger\hat{b}_{2n-1}\right)\\&+Js\sum_{n=1}^{\frac{N-1}{2}}\left(\hat{b}_{2n-1}^\dagger\hat{a}_{2n}^\dagger+\hat{b}_{2n-1}\hat{a}_{2n}\right)+Js\sum_{n=1}^{\frac{N-1}{2}}\left(\hat{b}_{2n+1}^\dagger\hat{a}_{2n}^\dagger+\hat{b}_{2n+1}\hat{a}_{2n}\right)\end{aligned} \tag{5.6}$$

and the equations of motion are

$$\begin{aligned}\mathrm{i}\frac{\partial}{\partial t}\hat{a}_{2n}=&(2Js+Ks)\hat{a}_{2n}+Js\left(\hat{b}_{2n-1}^\dagger+\hat{b}_{2n+1}^\dagger\right)\\&\text{for}\quad n=1,2,3,\cdots,(N-2)/2\end{aligned} \tag{5.7}$$

$$\begin{aligned}\mathrm{i}\frac{\partial}{\partial t}\hat{b}_{2n+1}=&(2Js+Ks)\hat{b}_{2n+1}+Js\left(\hat{a}_{2n}^\dagger+\hat{a}_{2n+2}^\dagger\right)\\&\text{for}\quad n=0,1,2,\cdots,(N-1)/2\end{aligned} \tag{5.8}$$

The spin on the bottom of the AF, the Nth layer, is only coupled to one AF spin and the equation of motion is

$$\mathrm{i}\frac{\partial}{\partial t}\hat{b}_N=(Js+Ks)\,\hat{b}_N+Js\hat{a}_{N-1}^\dagger \tag{5.9}$$

For the FM the equations are written in terms of m_x and m_y because the hard axis anisotropy will cause an elliptical, rather than circular, motion. Using the linearised

expansion of m_z the energy is written

$$\mathcal{E}_{\mathrm{FM}} = -\tilde{J}(s_{0,x}m_x + s_{0,y}m_y) - \tilde{J}s_{0,z} + \frac{\tilde{J}}{2}s_{0,z}(m_x^2 + m_y^2) + \frac{\bar{K}}{2}m_x^2 \tag{5.10}$$

The equation of motion is described by the Landau-Lifshitz equation

$$\frac{\partial}{\partial t}\mathbf{m} = \mathbf{m} \times \frac{\partial \mathcal{E}}{\partial \mathbf{m}} \tag{5.11}$$

Again, to linear order this gives the coupled equations

$$\begin{aligned} -\frac{\partial}{\partial t}m_x &= \tilde{J}sm_y - \mathrm{i}\tilde{J}\sqrt{\frac{s}{2}}\left(\hat{a}_0^\dagger - \hat{a}_0\right) \\ \frac{\partial}{\partial t}m_y &= \left(\tilde{J}s + \bar{K}\right)m_x - \tilde{J}\sqrt{\frac{s}{2}}\left(\hat{a}_0^\dagger + \hat{a}_0\right) \end{aligned} \tag{5.12}$$

The resonant frequency of a ferromagnet is almost always much lower than that of an antiferromagnet due to the exchange enhancement in the AF. Therefore, taking a quasi-static approximation (QSA) for the AF spins and seeking attenuated solutions

$$\begin{aligned} \hat{a}_n &= (A_q\mathrm{e}^{-qn} + B_q\mathrm{e}^{qn})\mathrm{e}^{\mathrm{i}\omega t} \underbrace{\equiv}_{\mathrm{QSA}} A_q\mathrm{e}^{-qn} + B_q\mathrm{e}^{qn} \\ \hat{b}_n &= (C_q\mathrm{e}^{-qn} + D_q\mathrm{e}^{qn})\mathrm{e}^{\mathrm{i}\omega t} \underbrace{\equiv}_{\mathrm{QSA}} C_q\mathrm{e}^{-qn} + D_q\mathrm{e}^{qn} \end{aligned} \tag{5.13}$$

where $Re(q) > 0$ is required for solutions and A_q/B_q and C_q/D_q are determined by the boundary conditions.

Addressing first the bulk equations equations (5.7) and (5.8)

$$\begin{aligned} (2Js + Ks)\hat{a}_{2n} + 2Js(\hat{b}_{2n-1}^\dagger + \hat{b}_{2n+1}^\dagger) &= 0 \\ (2Js + Ks)\hat{b}_{2n+1} + 2Js(\hat{a}_{2n}^\dagger + \hat{a}_{2n+2}^\dagger) &= 0 \end{aligned} \tag{5.14}$$

The solution of the secular equation restricts the value of q by the condition

$$\cosh(q) = \frac{2Js + Ks}{2Js} \tag{5.15}$$

which is a localised mode in the AF. It immediately follows that $\hat{a}_n = -\hat{b}_n$ and the boundary condition A_q/B_q is determined from the bottom AF layer spin Eq.(5.9)

$$-(Js + Ks)(A_q\mathrm{e}^{-Nq} + B_q\mathrm{e}^{Nq}) + Js(A_q\mathrm{e}^{-(N-1)q} + B_q\mathrm{e}^{(N-1)q}) = 0 \tag{5.16}$$

and from Eq.(5.15) $(Js + Ks) = Js(\mathrm{e}^{q} + \mathrm{e}^{-q} - 1)$ thus

$$\frac{A_q}{B_q} = -\frac{(\mathrm{e}^{q} - 1)\mathrm{e}^{Nq}}{(\mathrm{e}^{-q} - 1)\mathrm{e}^{-Nq}} = -\frac{\Delta_{+}\mathrm{e}^{Nq}}{\Delta_{-}\mathrm{e}^{-Nq}} \tag{5.17}$$

Solution of the interfacial AF spin Eq.(5.9)

$$(\tilde{J} + Js(\mathrm{e}^{q} + \mathrm{e}^{-q} - 1))(A_q + B_q) - Js(A_q\mathrm{e}^{-q} + B_q\mathrm{e}^{q}) - \tilde{J}\sqrt{\tfrac{s}{2}}(m_x + \mathrm{i}m_y) \tag{5.18}$$

leads to the expressions for the amplitudes A_q and B_q and thus a_n can be written

$$\hat{a}_n = \tilde{J}\sqrt{\tfrac{s}{2}}(m_x + \mathrm{i}m_y)\frac{\left[\Delta_{+}\mathrm{e}^{Nq}\mathrm{e}^{-nq} - \Delta_{-}\mathrm{e}^{-Nq}\mathrm{e}^{nq}\right]}{(\Delta_{+}\mathrm{e}^{Nq})(\tilde{J} + Js\Delta_{+}) - (\Delta_{-}\mathrm{e}^{-Nq})(\tilde{J} + Js\Delta_{-})} \tag{5.19}$$

For practical antiferromagnetic materials used for magnetic device applications the anisotropy energy is orders of magnitude smaller than the exchange energy. From Eq. (5.15) assuming $K \ll J$

$$\cosh(q) \approx 1 + \frac{q^2}{2} \tag{5.20}$$

giving the q value as the exchange length of the material

$$q \approx \sqrt{\frac{K}{J}}. \tag{5.21}$$

Applying the small q approximation to Δ_{+} and Δ_{-} and expanding $\exp(q) \approx 1 + q$, which gives

$$\Delta_{+} \approx q, \quad \Delta_{-} \approx -q. \tag{5.22}$$

This allows Eq. (5.19) to be written in the more compact form

$$\hat{a}_n = \tilde{J}\sqrt{\tfrac{s}{2}}(m_x + \mathrm{i}m_y)\frac{\cosh\left((N-n)q\right)}{\tilde{J}\cosh\left(Nq\right) + Jsq\sinh\left(Nq\right)} \tag{5.23}$$

From the FM equations of motion Eq.(5.12) and assuming solutions of the form $m_x = F\cos(\omega t)$ and $m_y = G\sin(\omega t)$

$$\begin{aligned}\left(\frac{F}{G}\right)\omega m_y &= \tilde{J}sm_y - \tilde{J}^2sm_y\Omega_0 \\ \left(\frac{G}{F}\right)\omega m_x &= (\tilde{J}s + \bar{K})m_x - \tilde{J}^2sm_x\Omega_0\end{aligned} \tag{5.24}$$

where

$$\Omega_n = \frac{\cosh\left((N-n)q\right)}{\tilde{J}\cosh\left(Nq\right) + Jsq\sinh\left(Nq\right)} \tag{5.25}$$

and so the eigen frequency is

$$\omega^2 = \left(\tilde{J}s - \tilde{J}^2 s\Omega_0\right)\left(\tilde{J}s + \bar{K} - \tilde{J}^2 s\Omega_0\right) \tag{5.26}$$

5.3 Damping

In general the frictional forces of a system are linear functions of the velocity and the dissipative function of the AF system can be written as[80]

$$Q_{\mathrm{AF}} = \frac{1}{2}\sum_{(n,m)=0}^{N} \alpha_{\mathrm{AF}} \frac{d}{dt}(\hat{a}_n^\dagger)\frac{d}{dt}(\hat{a}_m) \tag{5.27}$$

and the dissipation of the FM system is

$$Q_{\mathrm{FM}} = \frac{1}{2}\alpha_{FM}\left(\left(\frac{d}{dt}m_x\right)^2 + \left(\frac{d}{dt}m_y\right)^2\right). \tag{5.28}$$

Using Eq. (5.23) and performing the summation of the AF layers the total effective energy dissipation, $Q_{\mathrm{eff}} = Q_{\mathrm{FM}} + Q_{\mathrm{AF}}$, is found as

$$Q_{\mathrm{eff}} = \frac{1}{2}\left(\left(\frac{d}{dt}m_x\right)^2 + \left(\frac{d}{dt}m_y\right)^2\right)\left(\alpha_{\mathrm{FM}} + \alpha_{\mathrm{AF}}\tilde{J}^2 s\sum_{(n,m)=0}^{N}\Omega_n\Omega_m\right) \tag{5.29}$$

Hence the effective damping constant for the FM is

$$\alpha_{\mathrm{eff}} = \alpha_{\mathrm{FM}} + \alpha_{\mathrm{AF}}\frac{\tilde{J}^2 s\coth(q/2)\left(2N\sinh(q) + \sinh(2Nq)\right)}{2(\tilde{J}\cosh(Nq) + Jsq\sinh(Nq))^2}. \tag{5.30}$$

5.4 Numeric validation

The analytic results can be verified by numeric simulations. An atomistic approach is well suited to represent the AF because the microscopic moments can be resolved. This is in contrast to micromagnetics where approximations of AFs are not well justified as there is no net magnetisation on these length scales. The effective damping can be calculated in the same way as a resonance experiment. The system is held fixed in a

chosen direction by a strong direct current (DC) field and a small alternating current (AC) field is applied in a direction perpendicular direction to the DC field. The power absorption can then be measured as the overlap between the AC field and the motion of the spins[81]

$$P(\omega) = -\frac{\mu_s}{\tau N} \sum_i \int \mathbf{S}_i(t) \cdot \frac{\partial \mathbf{B}_{\mathrm{AC}}(\omega, t)}{\partial t} dt \tag{5.31}$$

where τ is the total time of the integral. In this system the pinning field from the AF acts as the DC field, fixing the FM magnetisation in the x-direction and the AF does not couple to the AC field due to the lack of a net magnetisation. The simulation must be performed for different driving frequencies to resolve resonance peak where the overlap integral becomes largest. A BCC lattice is used as a prototypical layered antiferromagnet, ensuring a perfect interface and alternating AF sublattices through the thin film. The system geometry is similar to that of the pinning and reference layers of a spin valve. To find the effective damping from the FMR line width, the calculations of Eq.(5.31) can be fitted by the approximate form[76]

$$P(\omega) = P_0 \frac{\omega_0^2 \left(\omega_0^2 + (H_{yy}/H_{zz})\omega^2\right)}{(\omega^2 - \omega_0^2)^2 + (\omega \Delta\omega)^2} \tag{5.32}$$

where

$$\begin{aligned} \omega_0 &= \gamma \sqrt{H_{yy} H_{zz}}; \quad \Delta\omega = \gamma \alpha_{\mathrm{eff}} \left(H_{zz} + H_{yy}\right) \\ H_{yy} &\approx \frac{(\omega_{\mathrm{eff}}/\gamma)^2 + (\alpha_{\mathrm{eff}} H_{zz})^2/2}{H_{zz}} \end{aligned} \tag{5.33}$$

Examples of fitted curves are given in Fig. 5.3, where α_{eff} and ω_{eff} can be extracted. From the resonance profiles it is clear that higher interfacial coupling strengths ($\tilde{J}$) leads to an increase in frequency and damping. The analytic solution can be validated by a comparison between the simulations and the analytic theory. In Fig. 5.4 comparing the frequency of the resonance peak with the eigenfrequency, predictions can be made for a range of interfacial coupling strengths and AF anisotropy energies. The close agreement validates the quasi-static approximation for the AF operators, showing that it is the local mode in the AF the FM couples to, not the uniform mode of the AF. A comparison between the measured damping (α_{eff}) with the damping calculated calculated analytically is shown in Fig. 5.5 and a good agreement is found. The choice of a large damping in the AF ($\alpha_{\mathrm{AF}} = 0.1$) gives a large increase in the effective damping of the FM as is seen in experiments. Observing a larger parameter space of the analytic form for the frequency and damping in Fig 5.6, the results show that the enhancement in the effective FM damping lies well within a tractable parameter range.

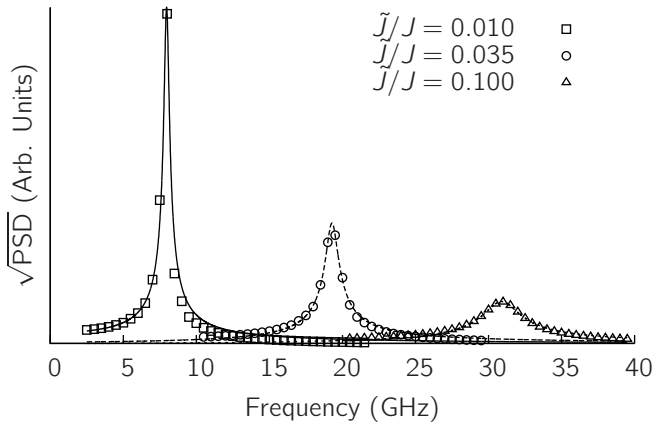

Figure 5.3 | Fitting resonance peaks from numerics. The fitted form allows the determination of α_{eff} and ω_{eff}. These examples show that increasing the interfacial coupling increases the frequency and also the damping.

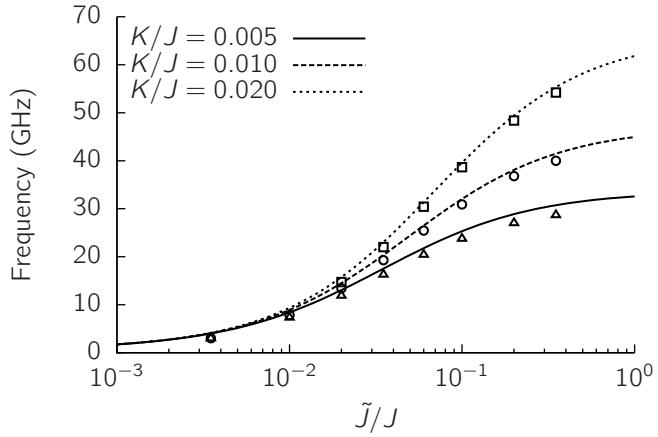

Figure 5.4 | Eigenfrequency of coupled AF/FM system. Frequency ω as a function of the interface coupling strength $\tilde{J}$. As the coupling strength increases the pinning field from the AF has more of an effect towards saturation at $\tilde{J}/J = 1$. The comparison between analytic (lines) and simulation (points) is very good. $\bar{K}/J = 0.003$.

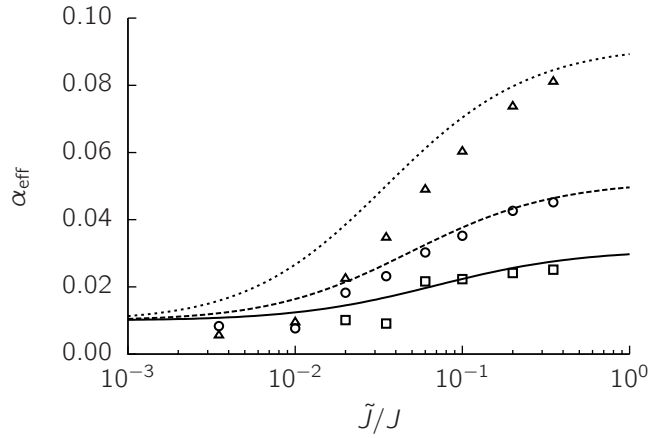

Figure 5.5 | Enhanced Gilbert damping of coupled AF/FM system. The effective damping of the FM increases with the interfacial coupling strength. Comparing the analytic theory (lines) and simulations (points) shows good agreement for the effective damping. $\bar{K}/J = 0.003$, $\alpha_{\text{FM}} = 0.01$, $\alpha_{\text{AF}} = 0.1$.

Even if α_{AF} is reduce significantly there is still an enhancement in the FM damping for strong interfacial coupling.

5.5 Damping through rough interfaces

The analytic and numeric work above demonstrates the excitation of the local AF mode through a perfectly coupled interface. In reality it is extremely costly to produce prefect interfaces in devices such as spin valves, therefore some roughness always exists. It is not clear a priori whether this damping mechanism will persist through a rough interface, where there may be some frustration due to competing exchange interactions. A rough interface can be modelled with an atomistic approach by creating a large bilayer and randomly substituting FM sites into the interface layer of the AF. Increasing the roughness of the interface reduces the effective interface coupling strength ($\langle \tilde{J} \rangle$) as the AF-FM coupling becomes compensated by interactions with both AF sublattices. By increasing the microscopic exchange interaction to maintain a constant frequency between systems of different roughness, it can be determined whether the strong local coupling still allows the increased in damping.

The FMR line widths are shown in Fig. 5.7. The perfect interface (Fig. 5.7a shows some enhancement in the damping above the intrinsic damping of the FM ($\alpha_{\text{FM}} = 0.01$). Increasing the interfacial roughness (Fig. 5.7b-c) requires a stronger microscopic interfacial exchange to maintain the 30GHz FMR peak, however the damping does not increase despite the large increase in the microscopic coupling

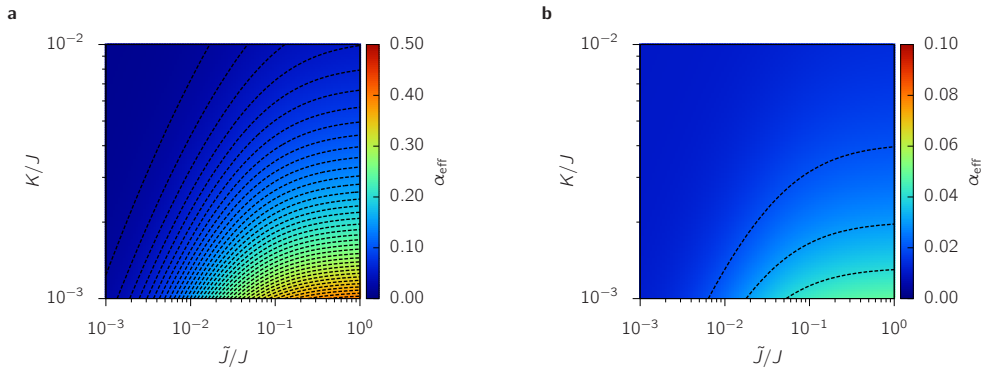

Figure 5.6 | Enhanced Gilbert damping parameter space. (**a**) The AF layer has a larger damping ($\alpha_{\mathrm{FM}} = 0.01$, $\alpha_{\mathrm{AF}} = 0.1$) and there is a significant increase in the effective damping of the FM layer with increasing interface coupling strength ($\tilde{J}/J$) and AF anisotropy (K/J). (**b**) Even for low AF damping ($\alpha_{\mathrm{FM}} = 0.01$, $\alpha_{\mathrm{AF}} = 0.01$) α_{eff} can be enhanced beyond the intrinsic damping of either material if there is strong interfacial exchange and high AF anisotropy. Contours are shown at every 0.01.

strength. This suggests that the local coupling is not the only factor and the average properties of the interface must be considered in determining the effective damping.

To elucidate why this is the case, the AF spin dynamics is visualised during a weak FMR excitation of the FM, comparing the perfect and rough interface. By colouring the spins in terms of their displacement from the equilibrium position, it can be see how the local mode in the AF is being excited across the lattice. In the perfect interface (Fig. 5.8a) there is no spatial variation in the amplitude of excitation in the AF. The microscopic mechanism identified above applies equally at all points on the lattice. Fig. 5.8b) shows that this is not the case for the disordered interface. In some regions of the lattice there is a greater amplitude of excitation than in the perfect interface due to the increased microscopic exchange strength. Other regions of the lattice show no displacement from the ground state (these appear white in the colouring scheme). This indicates that the FM is not exciting the AF local mode within these regions. The compensation of the FM-AF coupling in these regions, caused by the local coupling of the FM to both AF sublattices, means that the local mode cannot be excited as the interaction with one sublattice is countered by the other. Therefore it is the spatial average of the effective coupling across the interface which determines the volume of AF excitation and thus the enhancement in the damping of the FM.

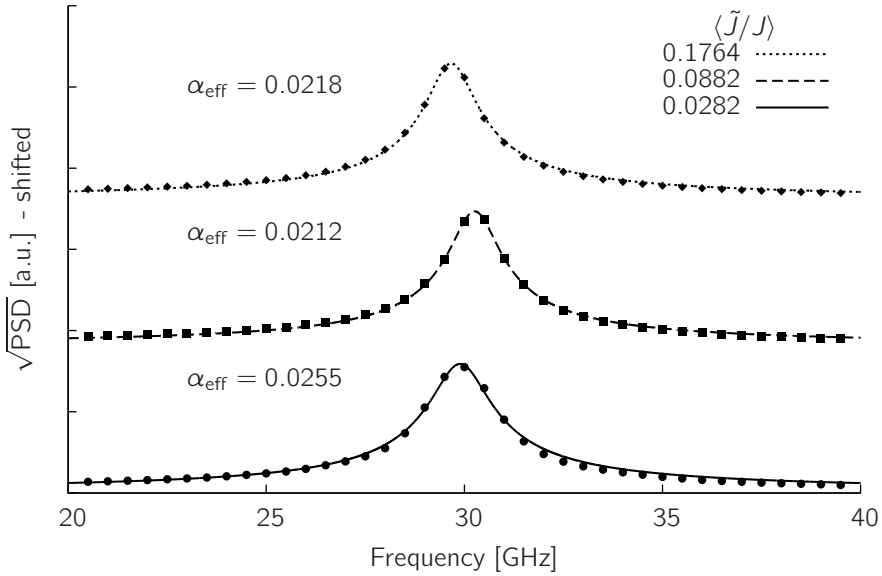

Figure 5.7 | Comparison of effective damping in bilayers with interfacial roughness. A perfect interface and two rough interfaces are simulated. The frequency is kept approximately constant at 30Ghz by increasing the microscopic exchange $\tilde{J}$. The effective damping, α_{eff} is extracted by fitting Eq. (5.32).

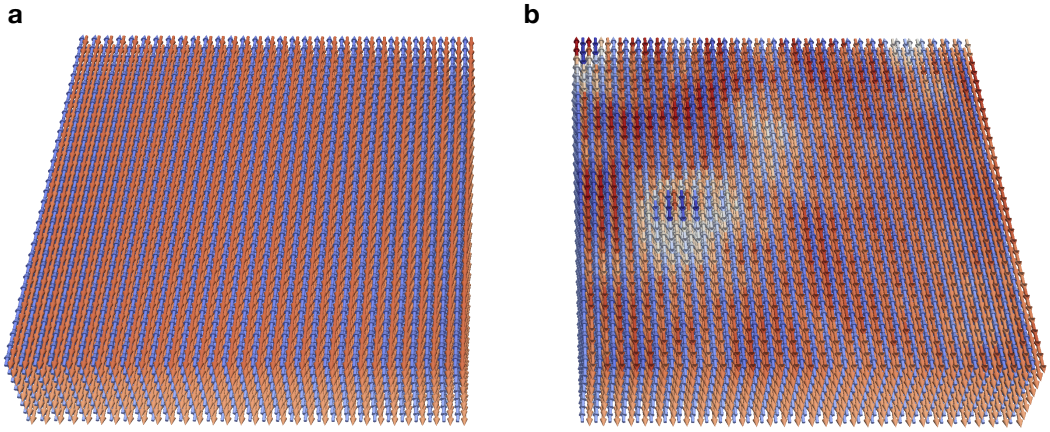

Figure 5.8 | Visual comparison of AF excitation in rough and smooth interfaces. The spin structure of the AF in a bilayer is visualised during a weak transverse excitation of the FM. The colour scheme shows the positive (red) and negative (blue) y-components of the spins from the ground state (white) along $\pm x$. (**a**) A perfect, smooth interface means the AF is excited coherently and with an even displacement of each sublattice. (**b**) A rough interface introduces exchange frustration. Some regions have a larger transverse displacement than in the perfect interface, due to the larger microscopic exchange coupling. Other areas have almost no displacement (white).

5.6 Conclusions

It has been shown that a local mode in the AF is excited from a coupled FM film. This mode effectively damps energy transfered from the FM, increasing the effective damping of the FM. This damping is relatively large for moderate and high interface coupling strengths. This work includes only a single processes of the energy transfer into the AF and as such supports other work which suggests this to be the primary mechanism of enhanced damping in such systems. In large systems the increased damping is often attributed to a large number of degenerate two-magnon scattering modes due to interfacial roughness. For small, nanoscale devices this contribution is likely to be significantly reduced and therefore the mechanism identified is a good explanation for the experimental observations. Knowledge of this mechanism allows both the tuning of device design, for example in spin valves and also has the potential to shed light on the properties of antiferromagnets, which are hard to measure directly. The blocking of the excitation by exchange frustration is intriguing and gives insight into how interface roughness affects the so-called 'pinning field' which is used as a measure of the AF properties. The results suggest that the disorder at the interface reduces the area of the AF which couples effectively with the FM.

CHAPTER 6

Four Spin Interactions in FeRh

One of the more novel experiments in the area of ultrafast magnetism is the generation of FM order in the metamagnet FeRh on a sub-picosecond time scale[10]. It has long been known that FeRh is a metamagnet with an AF-FM phase transition at $\sim$350K[82,83], but it is the speed at which this phase transition can occur which is astounding. The phase transition also causes a lattice expansion, resulting in an increase in the volume of the unit cell of $\sim 1\%$[84]. It is still an open question as to whether the transition is driven by magnetic or structural effects[85]. There is now a wealth of evidence both theoretical and experimental supporting both points of view. The original explanation for sub-picosecond response to laser heating was that a competition between magnetic ordering energies causes the phase transition[10,86], a theory which has not yet been tested. The purpose of the work presented here is to develop a simple model based on this hypothesis and to demonstrate that such a mechanism can lead to an AF-FM phase transition and that it is possible for the phase transition to occur on a sub-picosecond time scale.

6.1 FeRh Background

FeRh is a metallic alloy with a B2 structure, a BCC lattice where the central site is occupied by a Rh atom and the surrounding sites are Fe atoms. The low temperature ground state has been found experimentally[82] and from first principles[87] to be antiferromagnetic with two Fe sublattices in a chequer board fashion (Fig. 6.1a). Each Fe site has a moment of $\sim 3.15\mu_{\mathrm{B}}$ but the Rh ion has no net moment in this phase due to the symmetry of the surrounding Fe moments. There is some evidence that the strong hybridization of the Rh with the Fe significantly polarizes the electronic

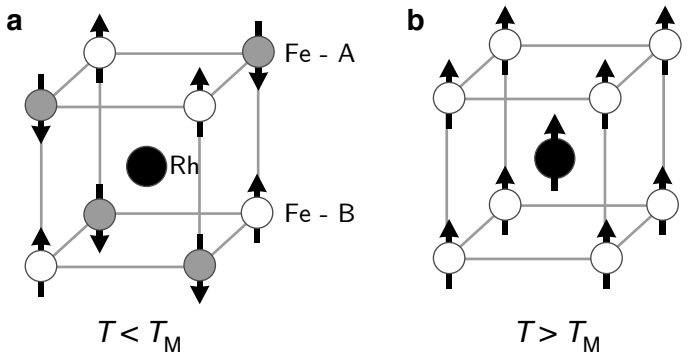

Figure 6.1 | FeRh Unit Cell. FeRh forms a B2 structure where the lattice is similar to a BCC lattice but the central site is Rh and the surrounding sites are Fe. **(a)** At low temperature $T < T_{\mathrm{M}}$ FeRh is an antiferromagnet with two Fe sublattices. There is no net moment on the Rh. **(b)** Above T_{M} FeRh forms ferromagnetic order and Rh now gains a moment of $1\mu_{\mathrm{B}}$.

structure of the Rh site but that the spatial average of the spin moment is zero[88]. Above the metamagnetic temperature, T_{M}, FeRh becomes ferromagnetically ordered and all Fe moments are aligned (Fig. 6.1b). The Rh site now also develops a moment of $\sim 1\mu_{\mathrm{B}}$ which is aligned with the Fe moments. In the FM state there is also a 1% expansion of the lattice volume. The FM phase undergoes a ferromagnet-paramagnetic phase transition at the Curie point, $T_{\mathrm{C}} = 700$K, in the same manner as a simple ferromagnetic material.

Models of FeRh

There exist several proposed models of FeRh which show the AF-FM phase transition. Gruner *et al.* (Ref. 89) combine a Blume-Capel Ising model[90–92] with lattice dynamics using Leonard-Jones molecular dynamics in a Monte-Carlo approach which includes a distance dependent exchange $J(r_{ij})$. The model is parameterised from ab initio calculations and they conclude that the phase transition occurs due to the instability of the Rh moment within the Blume-Capel Ising model. One of the key assumptions in their model is that the fluctuations on the Rh moment are independent of the fluctuations of the Fe moment, effectively saying that the thermal fluctuations on the Rh site lead to the spontaneous formation of a Rh moment. This explanation is challenged by ab initio calculations which show the formation of the Rh moment to be strongly dependent on the Weiss field from the surrounding Fe[86]. A different empirical model by Derlet (Ref. 93) considers a Landau-Heisenberg model. This model is built from a free energy expression which is designed to fit the ab initio data existing in the literature. The model includes fluctuations in the lattice volume and the transverse

and longitudinal fluctuations of the moments. The conclusion is that both volume and moment fluctuations play an equally important role in the occurrence of the phase transition. However this is not a dynamical model and can give no indication of the time scale on which the phase transition occurs. Moreover, the extensive Hamiltonian covering lattice and magnetic degrees of freedom means it would always be hard to identify if the phase transition originates in one system or the other.

A key aspects missing from these models is the ability to study the dynamics of the phase transition which is important given the exceptional speed at which the phase transition has been observed. While the models fit the first principles energy calculations, it does not exclude that there are other possible models which also fit the energetics but offer alternative explanations. Indeed, the Landau free energy approach is a Hamiltonian which is written to match the energetics. The mechanism investigated here has been suggested in the literature on the basis of experiments and first principles calculations[10,86]. This is that the phase transition originates from the magnetic degrees of freedom, where an effective four spin exchange interaction between the Fe moments plays an important role[†]. This model was put forward by Mryasov on the basis of non-collinear ab initio calculations. As the change in magnetic structure originates on an electronic level, such a mechanism can be of much higher speed than a phase transition driven by a lattice expansion. Thus this model may explain the high speed of the phase transition during femtosecond laser heating[10,86]. The key difference of this approach to that of Gruner *et al.* and Derlet is that the effect of the lattice expansion is not needed to describe the phase transition and it is assumed the lattice expansion will result from the change in the magnetic state. This explanation is supported by other first principles calculations which identify thermal spin waves as having sufficient energy to alter the magnetic structure from AF to FM[88]. Validating this approach offers an alternative explanation for the phase transition in FeRh and by exploring this possibility in an ASD approach the complex dynamics which cannot be observed experimentally are available.

6.2 Induced moment model

First principles calculations show that the magnitude and direction of the Rh moment is strongly dependent on the Weiss field from the surrounding Fe moments. They

[†]In his 2005 paper, Mryasov only included Hamiltonian terms up to biquadratic order, but the full expansion should include terms up to four spin order, which proves to be important finding the phase transition.

also show the Fe moment to be stable regardless of the size and orientation of the Rh moment (Fig. 6.2). Therefore the system can be described in terms of localised Fe moments and delocalised Rh moments. Thus the Hamiltonian can be written as Fe and Rh contributions as

$$\mathcal{H} = \mathcal{H}^{\mathrm{Fe}}(\{\mathbf{S}_i\}) + \mathcal{H}^{\mathrm{Rh}}(\{\mathbf{s}_\nu\}) \tag{6.1}$$

where $\mathbf{S}_i$ is a localised, Heisenberg, Fe moment and $\mathbf{s}_\nu$ is a delocalised Rh moment. The dependence of the Rh moment on the Weiss field is non-linear and a higher order term, beyond the Stoner model (see section 2), is needed to describe this behaviour. This can be written in the form of a generalised susceptibility

$$\mathcal{H}^{\mathrm{Rh}}\left(\mathbf{h}_\nu\right) = \frac{\chi^{(1)}}{h_{0\nu}^2}\left(\mathbf{h}_\nu\right)^2 + \frac{\chi^{(2)}}{h_{0\nu}^4}\left(\mathbf{h}_\nu\right)^4 \tag{6.2}$$

where $\chi^{(1)}$ and $\chi^{(2)}$ are susceptibilities and the Weiss field is normalised by its maximum value $h_{0\nu} = \sum_\nu \mathbf{h}_\nu$. The Weiss field is written

$$\mathbf{h}_\nu\left(\{\mathbf{S}_i\}\right) = \sum_i J_{i\nu}\mathbf{S}_i \tag{6.3}$$

where $J_{i\nu}$ is the exchange between the Fe site i and Rh site ν. The Hamiltonian can be written in terms of only Fe degrees of freedom by expressing the Weiss fields in terms of the interaction with the Fe moments. Thus the Rh contribution to the Hamiltonian is expanded in terms of Fe degrees of freedom as

$$\mathcal{H}_\nu^{\mathrm{Rh}} = \chi^{(1)}\sum_{i,j}\tilde{J}_{i\nu}\tilde{J}_{j\nu}\left(\mathbf{S}_i\cdot\mathbf{S}_j\right) + \chi^{(2)}\sum_{i,j,k,l}\tilde{J}_{i\nu}\tilde{J}_{j\nu}\tilde{J}_{k\nu}\tilde{J}_{l\nu}\left(\mathbf{S}_i\cdot\mathbf{S}_j\right)\left(\mathbf{S}_k\cdot\mathbf{S}_l\right). \tag{6.4}$$

Using the adiabatic approximation that the Rh moment is induced by the Weiss field on faster time scale than the spin dynamics and neglecting any Rh-Rh exchange interaction (which has shown from ab initio calculations to be very small compared to all other interactions[†]), Eq. 6.1 can be written purely in Fe degrees of freedom

$$\mathcal{H} = \sum_{i,j}\mathcal{J}_{ij}(\mathbf{S}_i\cdot\mathbf{S}_j) + \sum_{i,j,k,l}\mathcal{D}_{ijkl}(\mathbf{S}_i\cdot\mathbf{S}_j)(\mathbf{S}_k\cdot\mathbf{S}_l) \tag{6.5}$$

[†]Personal communication with O.N. Mryasov

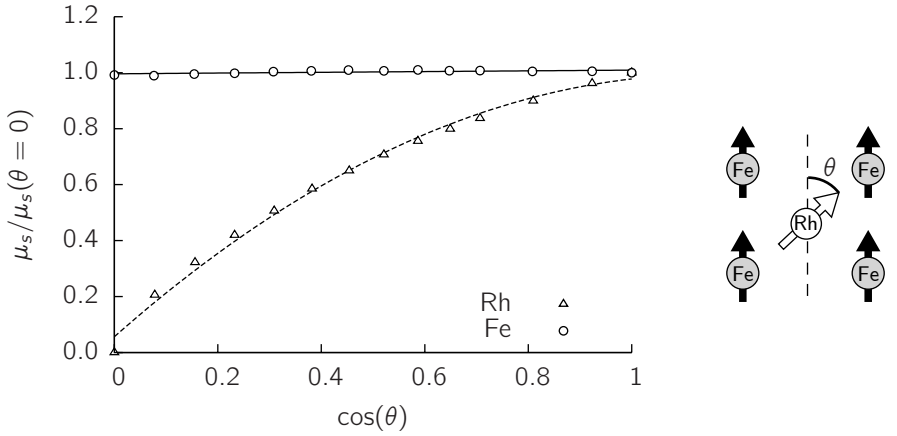

Figure 6.2 | Weiss field dependence of Rh moment. Constrained local spin density approximation calculations of the Rh moment as a function of angle between the Fe moments and the Rh moment. This shows a non-linear dependence of the Rh moment on the Weiss field, while the Fe moment remains constant. Figure adapted from Ref. 86

where $\mathcal{J}_{ij}$ and $\mathcal{D}_{ijkl}$ include both direct Fe-Fe exchange and a mediated Fe-Rh-Fe (and higher order) exchange

$$\begin{aligned} \mathcal{J}_{ij} &= J_{ij} + \chi^{(1)} \tilde{J}_{i\nu} \tilde{J}_{j\nu} \\ \mathcal{D}_{ijkl} &= \chi^{(2)} \tilde{J}_{i\nu} \tilde{J}_{j\nu} \tilde{J}_{k\nu} \tilde{J}_{l\nu}. \end{aligned} \tag{6.6}$$

This is an extended Heisenberg model where the second term is a four spin interaction. Such interactions can occur in materials where there is a significant contribution from electrons moving between four atomic sites. In this case the four spin term is a direct result of the non-linear behaviour of the induced Rh moment. The competition between the Heisenberg term and the four spin term may lead to a change in the order parameter[94] which is investigated in this prototypical model.

6.3 Four Spin Heisenberg Model

Currently there are no first principles calculations of the four spin contributions to the energy terms of Eq. 6.5. These calculations are complicated due to the mixing of bilinear, biquadratic and four spin energy contributions. Therefore constructing the simplest prototypical model of this Hamiltonian allows it to be assessed whether the AF-FM phase transition can occur. This can be implemented in an ASD approach by including an additional interaction matrix for the four spin interactions. In practical terms this is a four dimensional sparse matrix running over the spin indices i, j, k, l and the interaction strength $\mathcal{D}_{ijkl}$ is assumed to be a scalar. One of the immediate

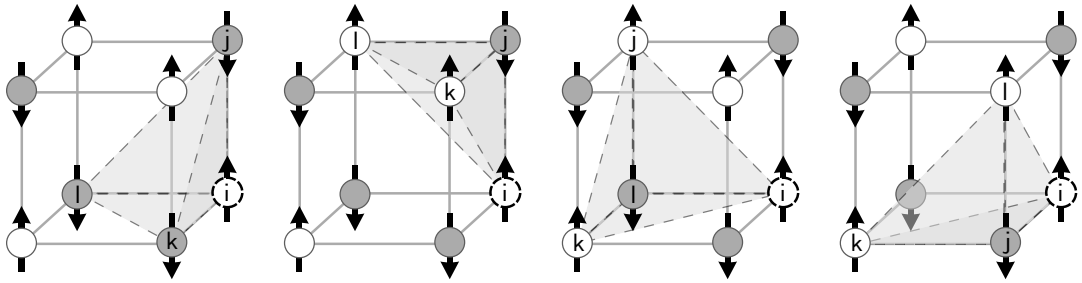

Figure 6.3 | Simple Cubic Basic Quartet. The basic quartet of the simple cubic lattice connects three spins from one sublattice and one from the other. Each lattice site, i, participates in 32 quartets.

complications is the choice of four spins over which to perform the sum. From the ansatz that the phase transition occurs due to the competition between the Heisenberg term and the four spin term it is assumed that one term is responsible for FM order and the other for AF order. Considering a mean field like treatment of thermal spin fluctuations, then the four spin term contains the product of four thermal spin averages $\langle S \rangle$, whereas the Heisenberg term contains the product of two such terms. Therefore the temperature dependence of the four spin term is greater than that of the Heisenberg term, leading to a crossover behaviour. Following this logic, the four spin term must be responsible for the AF low temperature ground state and the Heisenberg term should support FM ordering. This proposal is supported by first principles calculations which show that although the Fe-Fe exchange interactions contain large AF energies ($J_{ij} < 0$), the Fe-Rh exchange strongly cancels this effect and the effective Heisenberg exchange $\mathcal{J}_{ij}$ is dominated by FM energies[86]. The strong hybridization shown in other first principles calculations is also evidence that the Rh moment still plays a role despite the lack of a net moment in the AF state[88]. Interactions are restricted to the nearest inter- (J_{001}) and intra- (J_{111}) sublattice exchange interactions. The four spin term is treated in the simplest way by the set of four spins in the basic quartet[95] as shown in Fig. 6.3. These closed quartets connect the two sublattices with three lattice sites from one sublattice and one from the other. Therefore a negative value for D_{ijkl} promotes AF ordering. The energy from the four spin term must compete with a FM ordering from the inter-sublattice exchange, J_{001}, and in the ground state the four spin term must be greater than the Heisenberg term for the system to be antiferromagnetic.

6.4 First Order Phase Transitions

The metamagnetic phase transition in FeRh is a first order phase transition according to the Ehrenfest classification. This defines the order of a phase transition as the

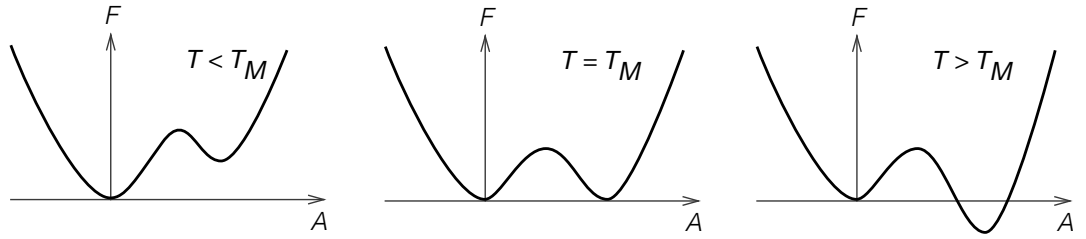

Figure 6.4 | The free energy of first order phase transitions. In a first order phase transition, close to T_M there are two minima in the free energy surface (F) corresponding to the order parameter (A). Below the transition temperature ($T < T_M$) one order parameter is lower in energy and this global minimum defines the phase. At $T = T_M$ the minima become equal and so a mixed phase occurs. Above T_M the minimum of the new phase now becomes the global minimum. Figure adapted from Ref. 97.

derivative of the free energy, with respect to a thermodynamic variable, which shows a discontinuity at the phase transition. For example the Curie point is a second order phase transition because it is the derivative of the magnetisation with respect to field, the susceptibility, which is discontinuous. The magnetisation and susceptibility are derivatives from the free energy (F) with respect to a field (H)

$$M = \frac{\partial F}{\partial H} \tag{6.7}$$

$$\chi = \frac{\partial M}{\partial H} = \frac{\partial^2 F}{\partial H^2} \tag{6.8}$$

The AF-FM phase transition in FeRh is a first order phase transition because it is the magnetisation which is discontinuous at the transition. First order phase transitions usually have interesting properties such as latent heat. There is also no critical behaviour associated with a first order transition. In a magnetic material this means that there is no divergence of the susceptibility and the spin-spin correlation length remains finite through the phase transition. This gives rise to a mixed phase where both phases coexist. In the case of FeRh this means that both FM and AF orders are observed at the phase transition[96]. It is important when investigating the proposed model of FeRh that the metamagnetic phase transition within the model is of first order. Care must be taken about how the phase transition is approached, because the free energy will contain two minima (one for each phase). At the phase transition both minima are equal, hence the phase coexistence, but above or below the phase transition, one minimum is lower in energy (Fig. 6.4). However if the system is prepared in an artificial state then the local minimum may be observed and not the global minimum if the energy barrier between the two is too high. Therefore the phase transition must be approached from both the low and high temperature limits, passing through many temperatures, to ensure that the true minimum is observed.

Inter-sublattice exchange energy	J_{001}	0.40×10^{-21}J
Intra-sublattice exchange energy	J_{011}	2.75×10^{-21}J
Four spin exchange energy	D_{ijkl}	0.23×10^{-21}J

Table 6.1 | Fitted exchange parameters for FeRh. The Heisenberg and four spin exchange parameters for the atomistic model of FeRh as fitted to experimental measurements (Fig. 6.5). Taking into account the number of interactions for each term, these values are of the magnitude expected in strongly ferro or antiferromagnetic materials.

6.5 Four Spin Model Equilibrium Results

The lack of detailed ab initio calculations of the effective four spin interaction means the model must instead be parameterised from the available experimental data. Even in this simple model, a set of exchange parameters can be found which reproduces simultaneously the experimental T_M and T_C, thus identify the total intra-, inter-sublattice and four spin exchange energies. While this is not necessarily an accurate depiction of the precise microscopic interactions, which may extend further within the lattice, it is a reasonable first approximation. Comparison is made to experimental magnetometry results of Kouvel *et al.*[83] and of Thiele *et al.*[98], although both samples are slightly Rh rich at $Fe_{48}Rh_{52}$. The parameters used use in the model are given in table 6.1. A magnetisation curve is produced from two systems which are cubic with linear dimension 9.55nm ($32 \times 32 \times 32$ unit cells, lattice parameter $a = 0.2985$nm) and with periodic boundary conditions. One system is started at zero temperature in the AF state and is heated in temperature steps of 10K until the Curie temperature, T_C. The other system is started above T_C is a randomised state and is cooled to zero temperature in 10K steps. At each step the system is allowed to equilibrate for 10ps before a thermal average of the magnetisation and Neel vector is calculated for a further 40ps. By comparing both magnetisation curves it is confirmed that the high and low temperature phases are indeed FM and AF, irrespective of how they are approached. These results are compared with the experimental results in Fig. 6.5b. The magnitude of the experimental results are normalised to match the reduced magnetisation of the model model.

In comparison to the experimental measurements, the T_{M} and T_{C} from the parameterisation are very similar. Even the shape of the magnetisation is well reproduced by the model, something which is not true of approaches based on an Ising model where a much more critical behaviour is observed at the Curie point[89]. The primary difference between the model Hamiltonian and the experimental results is in the width of the hysteretic behaviour at T_M where the simulations give $\Delta T = 50$K and the thin

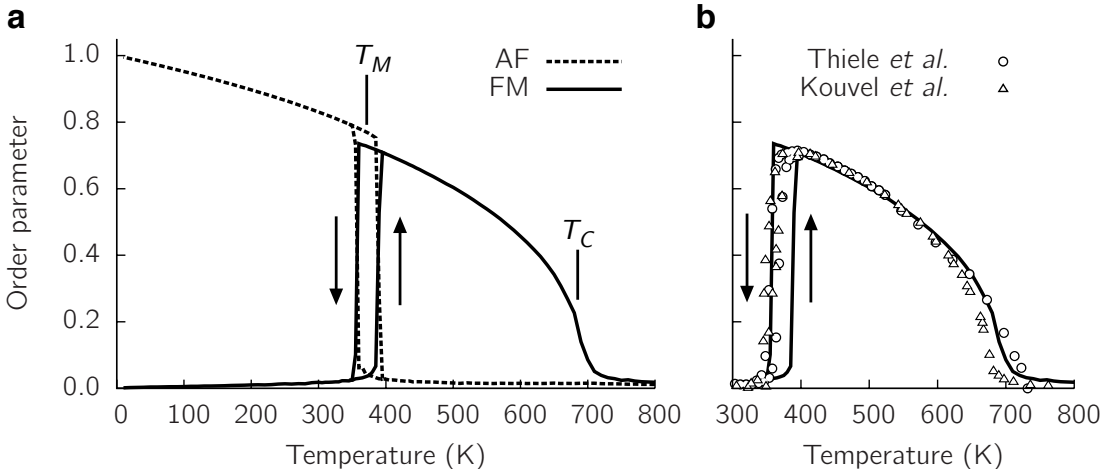

Figure 6.5 | FeRh magnetisation. (**a**) The exchange parameters in table 6.1 give good agreement to the experimental data for T_C and T_M. Thiele *et al.* (Ref. 98) and Kouvel *et al.* (Ref. 83). (**b**) From the experimental parameterisation of the model both AF and FM order parameters are observed. The arrows denote cooling and heating transitions.

film experiments show $\Delta T \sim 15$K. The hysteresis is indicative of the mixed phase and the associated latent heat of a first order phase transition. The reason for the difference is likely to be the limited time and length scales within the model. Finite size effects in first order phase transitions are highly non-trivial due to the lack of critical behaviour. The limited length scales available in a finite simulation limits the size of coherent regions in the mixed phase. Therefore surface effects, usually expressed in terms of a surface energy or tension, play a more dominant role in smaller systems[99]. The simulations are orders of magnitude smaller than experimental results where even laser spots for MOKE measurements are 3μm diameter[10]. Experiments on FeRh nanoparticles do show a very large broadening of the hysteresis with a width of $\Delta T = 110$K for nanoparticles with a mean diameter of 3nm[100,101]. By contrast the simulations are of a 9.6nm system with periodic boundaries and the value obtained for ΔT lies between the experimental nanoparticles and thin films. In terms of time scales, hysteretic behaviour is generally a time dependent phenomenon and so the speed at which the system is heated or cooled also plays a role in the width of the hysteresis. Through T_M the temperature was changed at an average rate of 20×10^9Ks^{-1}, much faster than magnetometry which is performed on the Ks^{-1} time scale.

The second set of experiments which are compared to, are those for the spin wave spectrum. Within the model the spectrum is calculate from the DSF (see section 4.3) and compared to experiments by Castets *et al.* (Ref. 102). This comparison is useful because in the low energy regime ferromagnets and antiferromagnets have different characteristic dispersions of $\omega_{FM}(k) \sim k^2$ and $\omega_{AF}(k) \sim k$ respectively.

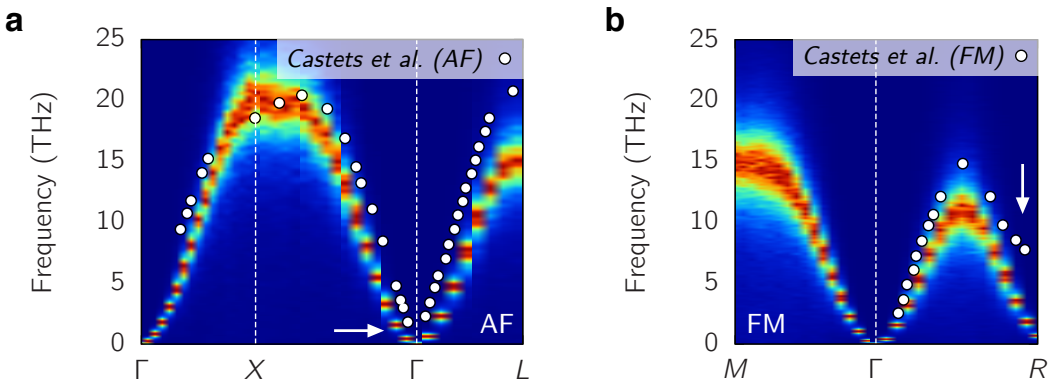

Figure 6.6 | FeRh magnon dispersion. From the parameterisation (table 6.1 the magnon dispersion is calculated from the DSF and compared with Brillouin zone experiments by Castets *et al.* (Ref. 102) in the AF phase **(a)** and the FM phase **(b)**.

The comparison between the model and experiment is shown in Fig. 6.6a and b. In both the AF and FM phases there is a reasonable agreement between the model and the measurements. The similarity in the magnitude of the largest frequencies means the parameterisation of the terms in the model (table 6.1) is reasonable. In the FM phase the low-k dispersion is quadratic in k. In the AF phase, the result appears more complicated with linear dispersion apart from a small area at very low k (marked with an arrow). This probably due to the fact that in the simple model the four spin and inter-sublattice Heisenberg exchange are competing on the same length scale. A full ab initio study of the interactions would be needed to determine the exact microscopic interactions and the length scales on which they dominate. There is also a large deviation at the edge of the Brillouin zone in the FM phase. This again can likely be attributed to the limited range of the simplified Hamiltonian. However, the essential physics is encapsulated, which appears both in experiments and is consistent with the induced moment model put forward on the basis of ab initio calculations.

The contribution of the Heisenberg and four spin terms in Eq. 6.5 is calculated. The results in Fig. 6.7 show that it is the competition between the four spin term and the Heisenberg term which leads to the phase transition. The gradient of the four spin contribution is much greater than that of the Heisenberg term due to the increased effect of thermal fluctuations on the product of four spins. At the phase transition, the change in ordering against the AF phase causes a frustration against the four spin term. The result is that the total energy at the phase transition is actually larger than at higher temperatures. This energy may dissipate into the lattice driving the lattice expansion.

The existence of a mixed phase is demonstrated to confirm the first order nature of

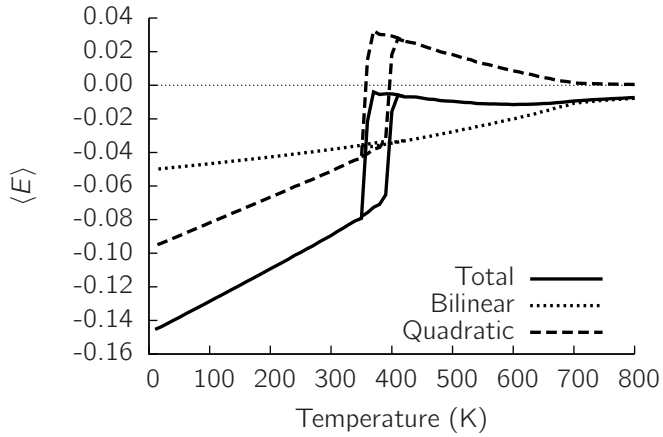

Figure 6.7 | Four spin energy terms. From the mean energy per spin $\langle E \rangle$. At the AF-FM phase transition the energetic minimum of the Heisenberg and four spin terms changes.

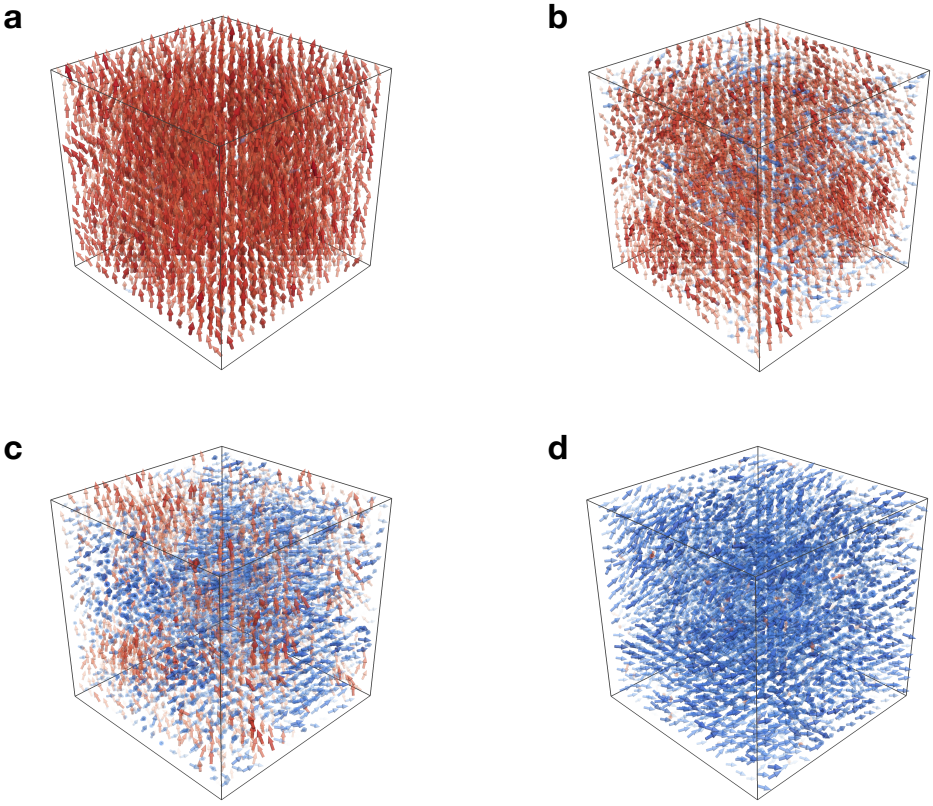

Figure 6.8 | Visualisation of AF-FM phase transition. Each unit cell is averaged to give a magnetisation vector (blue) and Neel vector (red). (**a**) Below T_M the system is an AF and there is no FM ordering. (**b**) Approaching T_M, small areas of FM order nucleate. (**c**) Through T_M a mixed phase is formed of both AF and FM order. (**d**) Above T_M the AF order disappears leaving only a FM phase.

this phase transition. The spin structure is visualised through the phase transition and regions of AF and FM order are differentiated by calculating the average magnetisation and Neel vector within each unit cell. In Fig. 6.8 several snap shots of the spin structure are shown at different points through the phase transition. The Neel and magnetisation vectors are coloured red and blue respectively and the size and orientation is shown by the arrows. Below the phase transition the lattice is entirely in the AF state. As the hysteretic region of the phase transition is entered, some FM nucleation begins at random points through the lattice. At T_M a mixed phase is observed, where AF and FM regions coexist within the lattice with approximately equal volumes. Once the temperature is above the phase transition the lattice shows only FM order.

6.6 Laser induced FM state generation

A unique aspect of approach used here to modelling FeRh is that the dynamical behaviour can be simulated. This is not possible with either Gruner *et al.* or Derlet's approaches[89,93] which are solved using Monte Carlo techniques which are not time quantified. Femtosecond laser heating experiments are simulated to observe the speed at which the phase transition can occur. The time scale of the model will be strongly influenced by the Gilbert damping parameter[48]. Different experimental observations of the Gilbert damping in FeRh give orders of magnitude difference in the value from the very large value of $\alpha = 0.3$ (Ref. 103) to the low value of $\alpha = 0.0013$ (Ref. 104). The difficulty in measuring the Gilbert damping is due to the difficulty in identifying direct and indirect damping in the inverse problem. For example the low value of $\alpha = 0.0013$ was obtained for the FM phase, but approaching the phase transition the damping was observed to increase significantly. The changes in the lattice structure and increased phonon excitation can increase the Gilbert damping, strong magnon-magnon scattering during the reorientation and even the coupling between AF and FM domains as in section 5 may contribute to indirect damping which is measured but should not be included in the Gilbert term as these damping mechanisms are intrinsic to ASD (see section 2.5). Therefore the dynamics are first studied as a function of the Gilbert damping. In Fig. 6.9 a 100fs heat pulse ($T_{e,\max}$ =879K) is applied to three systems with different Gilbert damping parameters. The time scale on which the FM order saturates is strong dependent on the Gilbert damping. In the case of large damping (α =0.100) the time scale for the initial growth of FM order is $\sim$3ps (indicated by the arrow). While this is certainly a fast time scale it is significantly longer than the sub-picosecond time scale of $\sim$500fs reported from experiments[10,105]. The dynamics are

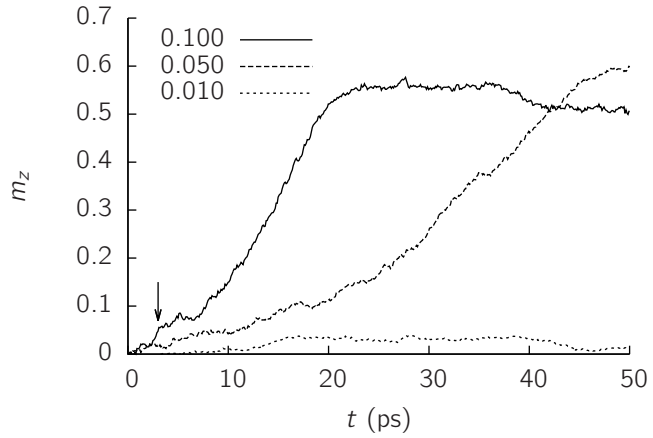

Figure 6.9 | Ultrafast generation of FM order. A 100fs laser pulse is applied at $t = 0$. The subsequent time scale of FM generation is strongly damping (α) dependent as indicated by the key.

also different those observed in thin films, where the interplay between the randomly formed FM domains causes a complex growth and decay of the FM order[96,103]. This is primarily due to the small size of the simulations. From the visualisations in Fig. 6.8 it can be seen that the mixed phase consists of two regions, an AF and a FM domain. This system is too small for multiple FM domains to exist within an AF phase for a long time scale. This presents two challenges for the future. First is for larger scale simulations to be performed. The four spin term is quite computationally expensive, even on the GPU, however optimisation techniques and utilising higher symmetries may make more bulk like systems tractable. Secondly, it is a challenge for experimentalists to image smaller thin film areas and particles of FeRh to allow a better understand of the microscopic behaviour, not just the average properties of a sample. If such advances can be made, then it will help to progress the understanding of the true mechanism behind the phase transition.

The results may also be affected by the choice of parameters for the two temperature model of laser heating. The choice of specific heat capacities (C_e, C_p) and the electron-phonon coupling strength (G) affect the thermal profile in the simulations significantly. In this model of FeRh the fact that the system passes through or near two phase transitions (T_M and T_C), one of which can have a mixed phase and the other has critical behaviour, means the dynamics will be strongly dependent on the temperature profile. As an example three different regimes are studied, where the generation of FM order is dependent on the time that $T_e < T_C$ and where the final temperature lies with respect to T_M.

In the first regime (Fig. 6.10a) T_e is above T_C for just a few femtoseconds and so the

AF order is not completely demagnetised. The final value of T_e is within the hysteretic region of the phase transition and so there is no energetic advantage for FM regions to form, hence the FM order does not increase. For a higher laser fluence (Fig. 6.10b) T_e is above the curie temperature for a longer period of time and so there is a larger reduction in AF order however this recovers within 5ps. Following this fast behaviour, there is a slower behaviour where the FM order increases at the expense of the AF order. Enough energy has been applied to overcome the latent heat and so the FM phase is now favourable. A further increase in fluence means T_e remains above T_C for long enough to destroy all order. On remagnetising, the temperature is above T_{M} and so the system restores in the FM phase.

6.7 Conclusions

It has been demonstrated that a first order AF-FM metamagnetic phase transition does exist in the Heisenberg model with four spin interactions. The strongly hybridised, induced moment picture of Rh within FeRh can be represented by such a Hamiltonian, and this model gives some evidence for an all magnetic origin for the phase transition observed in this material. The model model was parameterised from experimental data and are able to reproduce the equilibrium properties. This is the first dynamical model which has been used to show this phase transition and it allows comparison with optical pump-probe experiments. The dynamics found in the model show the generation of laser induced FM order on a picosecond time scale, slightly slower than is observed experimentally. Furthermore, high values of Gilbert damping must be used to obtain this behaviour, contrary to some experimental measurements. The existence of two phase transitions in the material can lead to different dynamics depending on small differences in the temperature profile applied. This may complicate the use of FeRh in future applications.

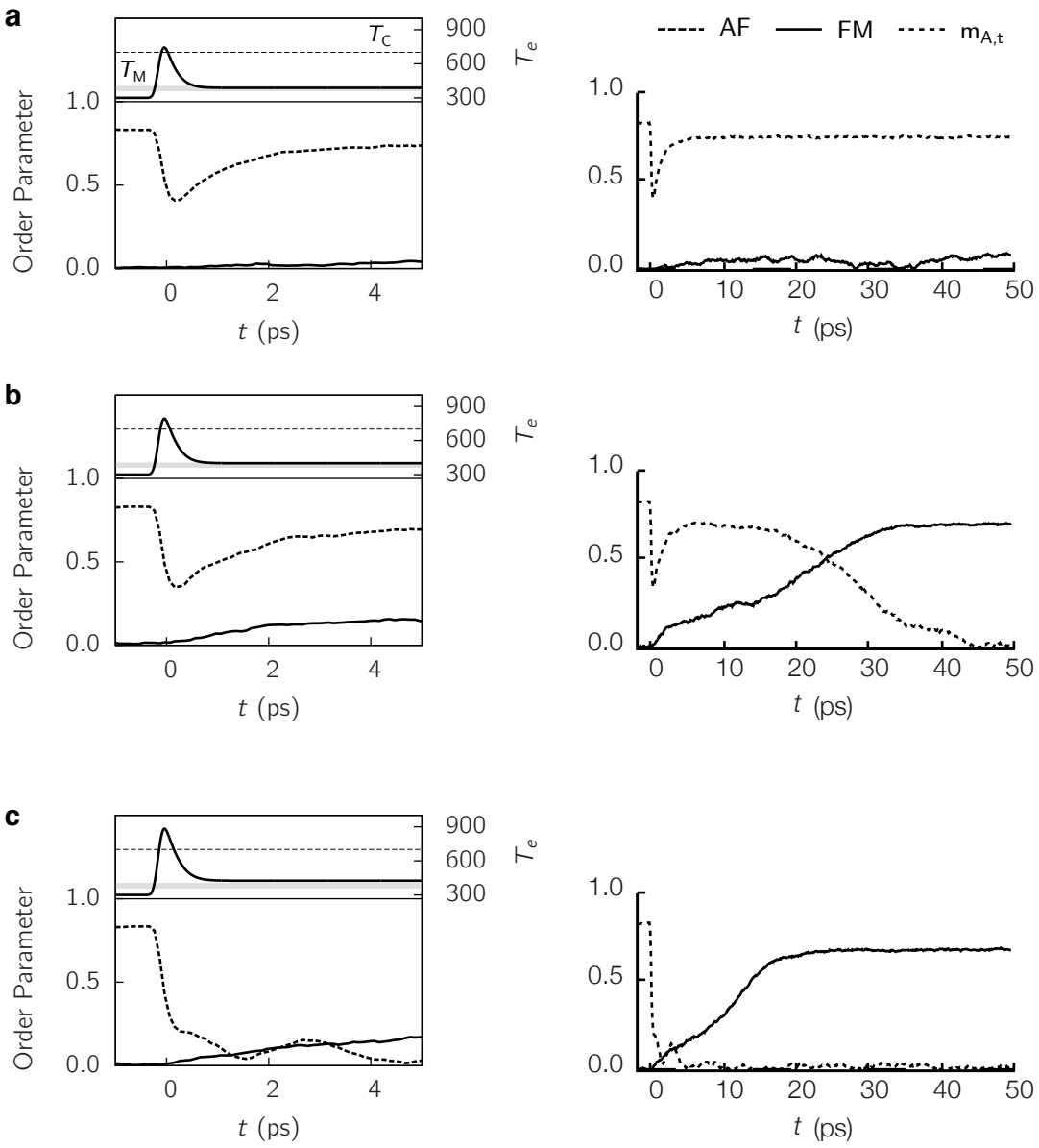

Figure 6.10 | Laser induced phase transition. The application of a 100fs laser pulse with increasing fluence. The short time scale is shown on the left and the long time behaviour on the right. **(a)** FM order is not generated as the laser provides insufficient energy to overcome the latent heat. **(b)** The laser now provides enough energy to produce a mixed phase and the FM order propagates from nucleated sites. **(c)** The system is heated above T_C for long enough to demagnetise the system significantly and recovers into the FM phase.

CHAPTER 7

Thermally Induced Magnetisation Switching

Thermally induced magnetisation switching (TIMS) occurs when an applied sub-picosecond heat pulse causes the magnetic state of a system to deterministically switch to the opposite state without any external or implicit magnetic field to determine the final state[9]. In the literature to date, this reversal mechanism has only been observed in the amorphous rare-earth ferrimagnets GdFeCo[9] and more recently TbCo[106]. It has not yet been explained why TIMS has only been observed in this class of materials and there is no existing theory of the microscopic mechanism which causes the switching behaviour. Understanding the reversal mechanism fully will help identifying other materials in which this behaviour may be observed for use in technological applications where use of rare-earth metals is decreasing due to the issues around sourcing these materials[107].

7.1 Background

It has been known for some time that the electric field of a high intensity laser can cause changes in the magnetisation of a magnetic material through the inverse Faraday effect (IFE)[108,109]. The induced magnetic field is

$$\mathbf{H} = \frac{\chi_{\mathrm{mo}}}{16\pi} \left[\mathbf{E}(\omega) \times \mathbf{E}(\omega)^*\right] \tag{7.1}$$

where χ_{mo} is the magneto-optical susceptibility. The use of circularly polarised light leads to an induced field, with opposite signs for left and right handed chiralities. Under the action of unpolarised (linear) light, there is no net field.

The optical excitation and control of magnetic materials using the IFE has been demonstrated in materials such as $DyFeO_3$ (Ref. 110) and $TmFeO_3$ (Ref. 111).

In 2007 Stanciu *et al.* discovered than in GdFeCo, a ferrimagnetic system, the magnetic state could be switched deterministically with circularly polarised light with the chirality determining the final state[4]. This result indicated the GdFeCo may have an exceptionally large IFE field of $\sim$1-3 Tesla[8,112]. However this was called into question by subsequent works where GdFeCo was show via atomistic spin dynamics to switch deterministically without any applied field, only the application of ultrafast heating. This was confirmed experimentally too by the use of unpolarised laser light and X-ray magnetic circular dichrosim (XMCD) which allows the measurement of magnetic species independently[9]. The helicity dependent switching shown by Stanciu *et al.* was eventually explained in terms of magnetic circular dichroism causing a difference in the energy absorbed by the material depending on the laser light helicity and the relative orientation of the magnetisation[113]. Once this magneto-optical effect is taken into account it is found that a minimum energy threshold needed for TIMS regardless of the helicity of the light. The implication is that there is an intrinsic material property which can be excited at this energy which leads to switching. However this mechanism has so far remained elusive. Finding the microscopic mechanism is important both for the fundamental understanding of this unexpected phenomenon and also to allow technological exploitation. If the intrinsic mechanism is identified then it could allow the materials to be optimised to improve switching or allow switching at lower laser energies. Also, the use of rare-earth elements is being reduced due to issues over the sourcing of the natural deposits[107] and so if this type of switching could be found in other materials or even manufactured in metamaterials this expand the potential for application considerably.

There have been several attempts to explain TIMS, although so far these are almost exclusively based on a macroscopic description of the magnetisation dynamics. Mentink *et al.* described the reversal in terms of longitudinal relaxation via the exchange interaction[114]. Such an explanation is contested by Atixita *et al.* who find that the relaxation of the transverse magnetisation components must also be considered[115]. Crucially though, neither work describes how the initial state is formed that allows these relaxation paths. Schellenkens and Koopmans introduce a microscopic Hamiltonian which describes the switching based on exchange scattering[116]. Their Hamiltonian is for a quantised spin and also includes a Debye model to represent the lattice coupling. They identify that exchange scattering leads to angular momentum transfer between the sublattices, but don't identify any clear criteria for the material properties which are important for the switching.

GdFeCo has ferrimagnetic ordering meaning that the Gd and Fe or Co moments are antiparallel with each other, but because Gd has a much larger moment than Fe or Co, the magnetisation from each sublattice does not necessarily cancel as it would in an antiferromagnet. The lack of a complete cancellation in the magnetisation leads to a measurable net magnetisation in the direction of the dominant sublattice. The different species in a ferrimagnet are also coupled by different exchange energies and if only nearest neighbour exchange interactions are considered, then there are possibilities for inter- and intra-sublattice exchange energies resulting in three exchange parameters. The net magnetisation can have a complex temperature dependence because of the differing exchange energies. At the magnetisation compensation temperature (T_{Comp}) the effective magnetisation, $M(T)$ of both sublattices cancel completely (Fig. 7.1) and crossing through this point, the dominant sublattice changes. The compensation point also leads to a divergence in the Gilbert damping of the material[117]. In much of the literature, it is the traversal of the compensation point which is attributed to TIMS[106,118,119]. However there is also contrary evidence where reversal is found to occur in both simulations and experiments above the magnetisation compensation temperature[9] and also in compounds without a compensation point[120]. It is still unknown what role, if any, the compensation point plays.

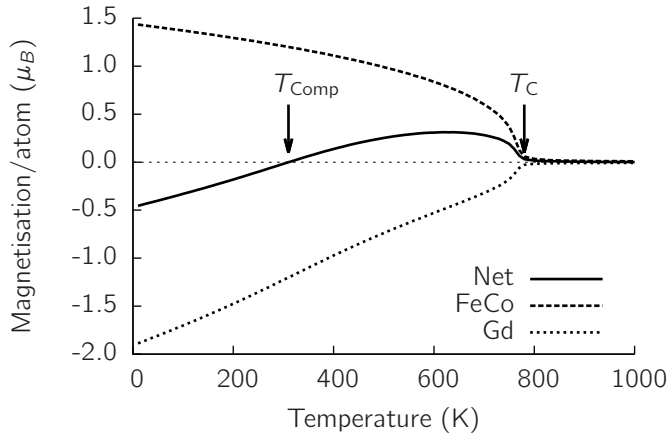

Figure 7.1 | Magnetisation compensation point. The effective magnetisation of each sublattice is temperature dependant according to the exchange interactions. The total moment from each sublattices cancels at the magnetisation compensation temperature (T_{Comp}). This point depends on the size of the moments of each sublattice and the concentration of each species.

7.2 GdFeCo Impurity Model

As an amorphous material, GdFeCo has no underlying crystal structure. Moreover, the large physical size of Gd atoms in comparison to Fe or Co atoms means that the microstructure of such a material is very complex. Recent X-ray measurements of GdFeCo samples show spatial inhomogeneity, where some areas are Gd rich and other areas Gd poor[121]. Constructing a model which includes all of these structural effects would make it difficult to interpret the important physics behind the switching. Instead a prototypical model of GdFeCo is constructed which contains the minimum complexity required to describe the physics of the system and which shows TIMS. Specifically a two sublattice ferrimagnet on a lattice is created, but where the lattice sites are randomly assigned as FeCo or Gd (Fig. 7.2). The Fe and Co moments are combined into a single effective spin as a simplification because the Co content is low (<10%) and is present only to introduce some uniaxial anisotropy into the material for experimental reasons. While no account is taken for the physical size of the atomic species within this model, different exchange constants are ascribed for inter- and intra-sublattice exchange so that the Curie temperature and magnetisation compensation points are similar to those observed experimentally[122].

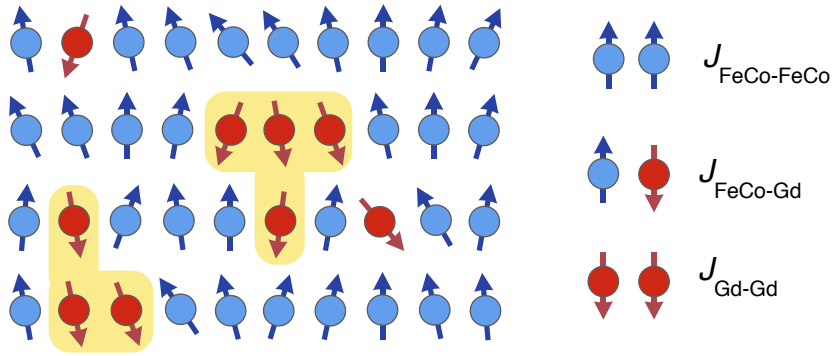

Figure 7.2 | GdFeCo lattice impurity model. FeCo spins (blue) are randomly substituted with Gd spins (red) to a given concentration. There are three types of elementary interactions FeCo-FeCo and Gd-Gd promote FM ordering within their own sublattice and FeCo-Gd which supports AF ordering between sublattices. The random placement of Gd sites also causes the formation of clusters of Gd within the lattice (yellow).

The supercell created for the random impurity model means that for a small system the results would be very sensitive to the random lattice configuration which is generated. To minimise these effects and to ensure the results are relevant on experimental length scales of tens of nanometers, very large systems are simulated where the super cell contains over 2 million spins ($128 \times 128 \times 128$). Here the acceleration obtained from

the GPU implementation becomes very important as the amorphous lattice does not allow the use of Fourier methods to accelerate the calculation of interactions on the lattice[123]. In small systems the spin wave spectrum also becomes highly discrete which can substantially alter the physics of a system and has been shown in the study of nanostructures in many areas of condensed matter physics. Such nanostructures and the different physics that may occur will need to be considered in the future if TIMS proves to be of technological use. The parameters used to represent GdFeCo in this model are given in table 7.1. Note that in this model there is no angular momentum compensation point which can occur if the two species posses different gyromagnetic ratios.

FeCo-FeCo Exchange Energy	J_{ij}	6.920×10^{-21}J
FeCo-Gd Exchange Energy	J_{ij}	-2.410×10^{-21}J
Gd-Gd Exchange Energy	J_{ij}	2.778×10^{-21}J
FeCo Anisotropy Energy	d_z	8.072×10^{-24}J
FeCo Moment	μ_{s}	$1.92\mu_{\mathrm{B}}$
FeCo Damping	α	0.02
FeCo Gyromagnetic Ratio	$\gamma\gamma_e$	1.00
Gd Anisotropy Energy	d_z	8.072×10^{-24}J
Gd Moment	μ_{s}	$7.63\mu_{\mathrm{B}}$
Gd Damping	α	0.02
Gd Gyromagnetic Ratio	γ	$1.00\gamma_e$

Table 7.1 | Material parameters used in the atomistic model for GdFeCo.

7.3 Intermediate Structure Factors

The deterministic reversal observed in TIMS implies that some order is being retained, despite the almost complete demagnetisation of the spin system. To observe the correlations between spins on all length scales present in the lattice, the intermediate structure factor (ISF) can be calculated

$$\mathcal{S}(\mathbf{k},t) = \frac{1}{N}\sum_{\mathbf{r},\mathbf{r}'} \mathrm{e}^{-\mathrm{i}\mathbf{k}\cdot(\mathbf{r}-\mathbf{r}')} C(\mathbf{r}-\mathbf{r}') \tag{7.2}$$

where the equal time spin-spin correlation function is defined as

$$C(\mathbf{r}-\mathbf{r}') = S_+(\mathbf{r},t)S_-(\mathbf{r}',t) \tag{7.3}$$

The ISF is a measure of the power in spin waves of wave vector $\mathbf{k}$ at a given instance in time. A random lattice system is being considered, but it will be useful

to express directions in the reciprocal lattice in terms of the simple cubic symmetry points as shown in Fig. 7.3. For a ferromagnetic system in equilibrium the distribution will be approximately Bose-Einstein (magnon excitations are approximate Bosons[124]). However under the non-equilibrium conditions of fast laser heating this distribution may be radically altered. In a ferrimagnet (or antiferromagnet) Holstein-Primakoff (Eq. 7.4) transformation[125] must be performed to express the excitations of both sublattices in terms of a common set of normal modes. In practice this means inverting the spins of one sublattice, whilst maintaining the handedness of the system

$$S_x \rightarrow S_x; \quad S_y \rightarrow -S_y; \quad S_z \rightarrow -S_z \tag{7.4}$$

The laser heating from the two temperature model increases the power in all spin wave modes significantly, but it is the changes in the distribution of power that are of most interest, rather than the absolute power which is roughly proportional to the spin temperature of the system. Some changes to the ISF power distribution with temperature are expected due to the softening of the spin wave spectrum and higher order magnon processes (section 4.4) however the $\omega \sim k^2$ (ferromagnet) or $\omega \sim k$ (antiferromagnet) low energy regime is still dominant even very close to the Curie temperature. So that the distribution can be observed regardless of the absolute power, a normalisation is performed such that the peak power for any instant in time is unity. This helps to maintain a good contrast despite the large change in system temperature.

Ideally the frequencies as well as the wave vectors of the excited spin wave modes would be calculated. However the time scale on which the demagnetisation and switching occurs gives insufficient time for such a calculation to be meaningful. It is sometimes possible to perform a study of these frequencies using a stroboscopic frozen magnon approach[126]. This involves taking snapshots of the spin lattice at time points of interest and evolving trajectories in the absence of Gilbert damping to observe the modes present in the system. However in such a method there still exists indirect damping, so spin wave modes can still decay (section 2.5). This damping will be especially strong where the spin lattice in non-uniform as in the amorphous lattice model. Instead the ISF is measured and the behaviour of the system is inferred from the spin wave spectrum, $\mathcal{S}(\mathbf{k}, \omega)$, under the adiabatic approximation that the laser heating is so fast that the occupation of spin wave modes is significantly altered without significantly changing the spin wave spectrum.

It is known from experiments and simulations that there is a threshold laser fluence required to induce TIMS[113] and so the ISF is studied both below and above the

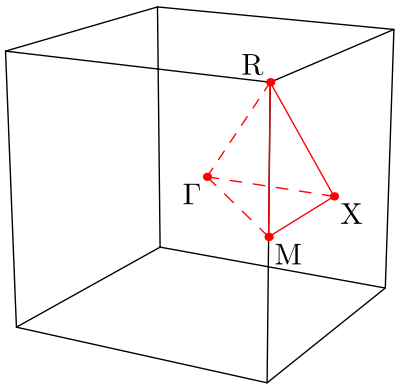

Figure 7.3 | Symmetry points of the simple cubic Brillouin zone. A simple cubic lattice is used and although there is a random placement of Gd moments, directions are referred to in terms of the symmetry points of the simple cubic Brillouin zone as shown here.

switching threshold fluence to observe if there is a difference in the distribution of power in spin wave modes. In Fig. 7.4-7.6 laser heating of the spin system is simulated with the two-temperature model using a Gaussian laser power profile with a width of 50fs. The laser fluence is adjusted so that even with many replicates the same qualitative behaviour is observed for switching with 25% Gd. A fluence above and below the threshold is used for low Gd concentration (10%), the switching concentration (25%) and high Gd concentration (35%). Note that the many replicates cannot be averaged because the stochastic dynamics have slight differences in the time scale of key features and the averaging of such data sets leads to a smearing of features which are observable in each data set individually.

For the low Gd concentration there is no switching for low or high laser fluences (Fig.7.4a,b). The magnetisation of each sublattice reduces but without any switching. The ISF results show that the heating causes a redistribution of the magnons leading to a peak in non-zero k modes. With such a low Gd concentration this system is essentially a ferromagnet and this redistribution of modes is consistent with the formation of randomly orientated unstable domains as previously observed in such systems[48,127]. The degree of demagnetisation determines how long it takes for the domains to annihilate.

In Fig. 7.5a,b the Gd concentration of 25% is used where switching is found. In the upper pannel where the laser fluence is too low to induce switching it can be seen that despite the large degree of demagnetisation the magnon distribution is still centered on the Γ-point. Once the laser fluence is sufficiently high, switching occurs. During the switching, spin waves are strongly excited at the same length scale as the

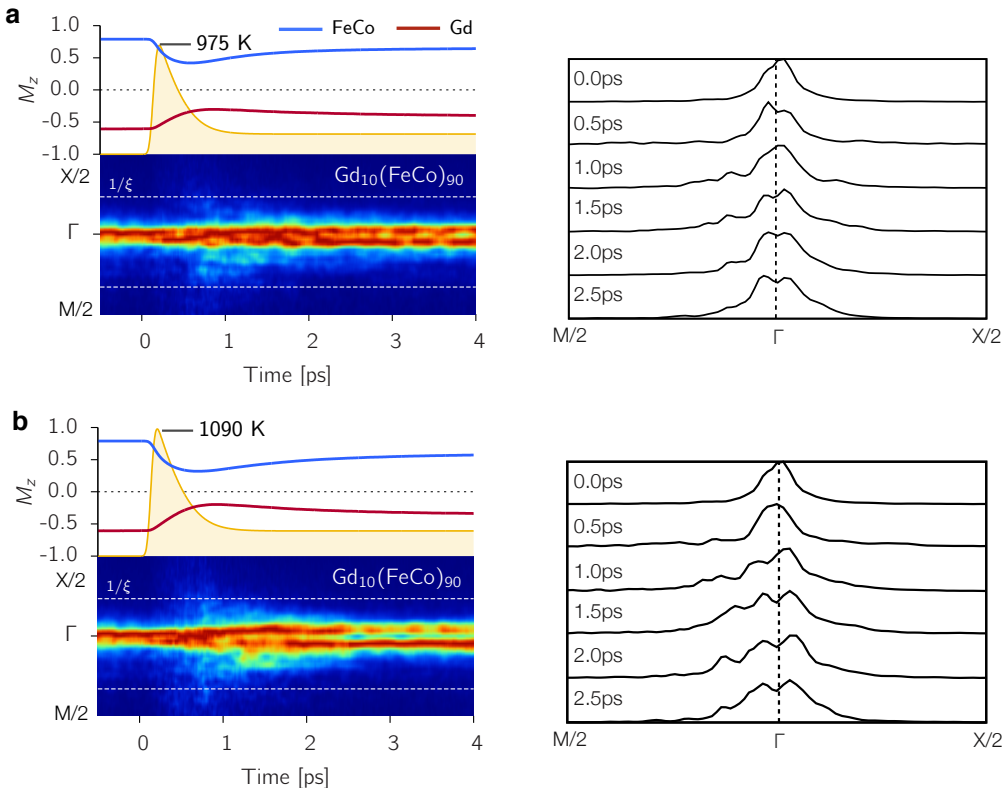

Figure 7.4 | ISF and dynamics for laser excitation - 10% Gd. On the left the magnetisation dynamics and corresponding ISF are given for a 50fs laser excitation with a different fluence in each case. On the right, cross sections of the ISF are given for different times. (**a**) The magnon distribution widens under the application of the laser pulse but this causes only a little demagnetisation. (**b**) For a higher laser fluence, the peak electron temperature is greater and the magnons are now distributed even more widely within the Brillouin zone. There is a small amount of reduction in the excitation on long length scales (at the Γ-point). This is due to the low concentration of Gd sites acting a pinning sites for spin wave modes.

physical correlation length. This excitation lasts only for the duration of the switching and then decays back to the Γ-point. In this system there are a significant number of antiferromagnetic interactions between the Gd and FeCo moments. However this material can no be classified as a ferromagnet or antiferromagnet. Later DSF is studied to find the nature of the excitations in this system.

At the higher Gd concentration of 35%, there is no switching observed. Instead the system demagnetises significantly for both laser fluences (Fig. 7.6a,b). There the excitations are short lived, consistent with the more antiferromagnetic nature of this concentration.

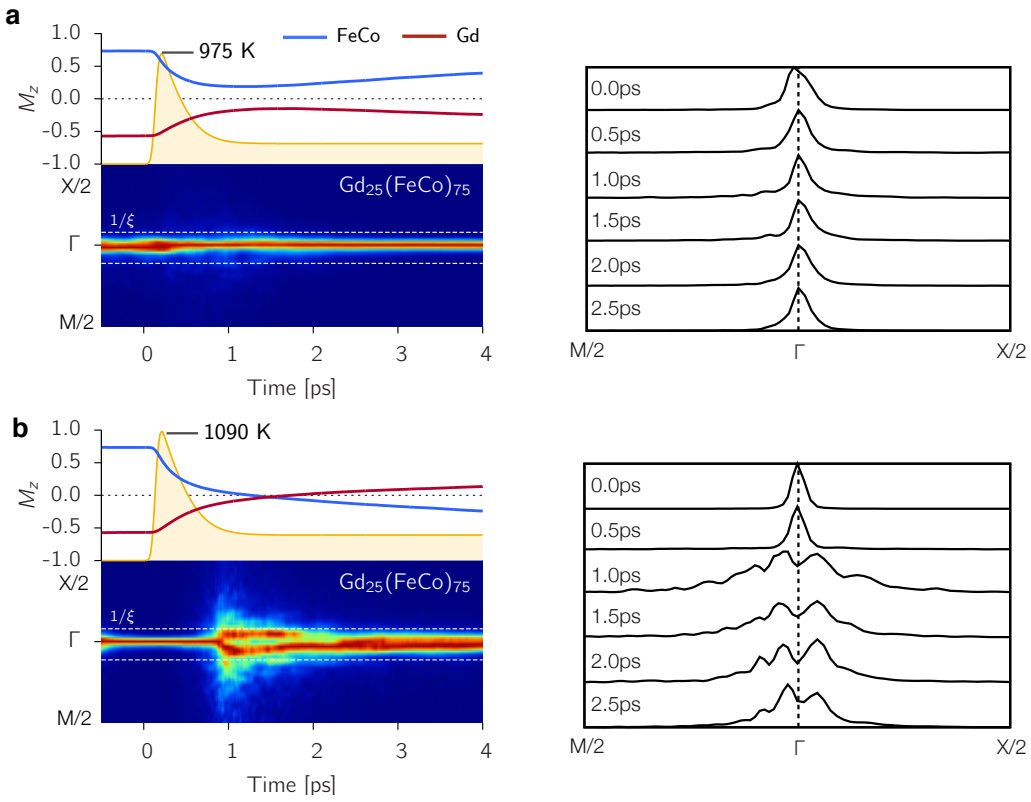

Figure 7.5 | ISF and dynamics for laser excitation - 25% Gd. (**a**) The laser pulse causes more than 50% demagnetisation of both sublattices, but the is little difference in the ISF as the power is distributed among the magnons with no regions of preferential excitation. (**b**) Once the threshold energy has been overcome by a larger laser fluence TIMS occurs and the sublattices form a transient FM state and switch. This corresponds with the almost instantaneous excitation a specific k-vector. This excitation lasts for the duration of the switching and then decays quickly.

7.4 Magnon Band Structures

Dynamic Structure Factors

To interpret the ISF results and the nature of the magnons on different length scales the spin wave spectrum of the impurity model must be calculated in a similar manner to section 4.3. As well as windowing the temporal Fourier transform, a Gaussian convolution of width $\Delta f \approx 0.95$GHz is applied to reduce noise in the spectrum. A normalisation along each k-vector is also performed, so that the maximum value on any given k-vector is unity[14] (see appendix A1). This allows the observation of the dispersion relation and the width of the bands. The information about the absolute amplitude of spin waves at equilibrium is therefore not represented, however

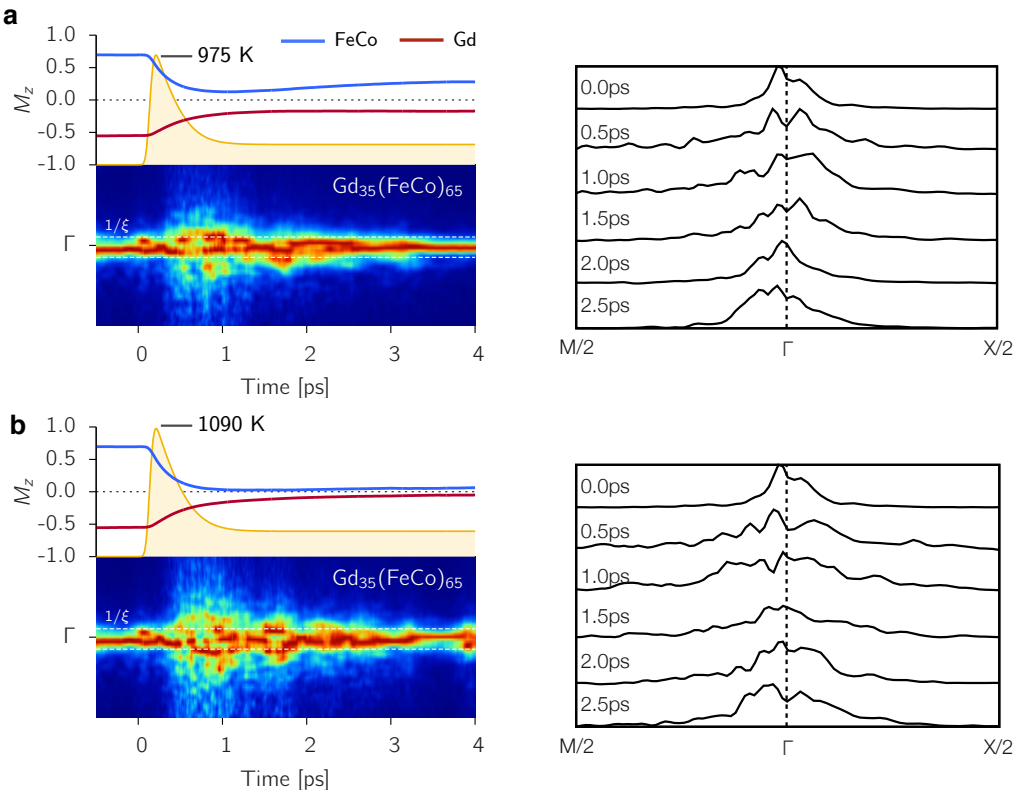

Figure 7.6 | ISF and dynamics for laser excitation - 35% Gd. The increase of Gd content reduces the Curie temperature of the compound because $J_{FeCo-Gd} < J_{FeCo-FeCo}$. In both (**a**) and (**b**) the excitation of magnons is very broad and excitations fluctuate on different length scales.

the distribution of spin waves is already given from the calculated ISF (Fig. 7.4-7.6). Therefore the distribution of power within the DSF at any given point in time is inferred from the ISF.

It is well known that ferrimagnets contain two branches in the spin wave spectrum[33]. This is due to the occurrence of both ferromagnetic and antiferromagnetic interactions within the lattice. The relative amplitude of one branch to another is important, especially within an amorphous lattice as it gives information about the length scales on which these modes are found. Because this is a quantity of interest the combined band amplitude is calculated as

$$\mathcal{A}'_{\mathbf{k}} = (\mathcal{A}_{\mathbf{k},1} + \mathcal{A}_{\mathbf{k},2}) - 1 \tag{7.5}$$

where $\mathcal{A}_{\mathbf{k},1}$ and $\mathcal{A}_{\mathbf{k},2}$ are the normalised amplitude on a given k-vector of each band respectively. Thus $\mathcal{A}'$ is unity when both bands have an equal amplitude and is zero when one band has zero amplitude because the highest amplitude is always normalised

to unity. The simple integration of the power on a given k-vector would distort the results due to the linewidth of each band.

Figure 7.7 shows the DSF for different Gd concentrations as marked in the top left of each colour panel. The white dashed curve on top of each DSF is the spin wave dispersion as calculated from LSWT (discussed in the next section). The red panel above each DSF is $\mathcal{A}'$. The black arrows are calculated from a physical correlation length as discussed later.

Linear Spin Wave Theory

To compare with the numerical calculations and introduce a predictive ability the virtual crystal approximation is used within linear spin wave theory to calculate the spin wave dispersion for an amorphous ferrimagnet. The equations were derived by U. Atxitia at York University and is included here for completeness.

To treat the amorphous characteristic of GdFeCo the virtual crystal approximation is used to weight the exchange parameters relative to the composition

$$\begin{aligned} J_{0,11} &= (1-x)zJ_{11} \quad J_{0,12} = xzJ_{12} \\ J_{0,21} &= (1-x)zJ_{21} \quad J_{0,12} = xzJ_{22} \end{aligned} \tag{7.6}$$

where x is the Gd content, z is the coordination of the lattice, J_{xx} are the bare interactions between the moments of each sublattice and $J_{0,xx}$ are the mean field interactions between the moments in the virtual crystal approximation. The LSWT analysis can be performed in a similar manner to that in section 4.2. Linearising the Landau-Lifshitz equation of motion gives

$$\frac{\mathrm{d}}{\mathrm{d}t}\begin{pmatrix} s^+_{\mathbf{k}1} \\ s^+_{\mathbf{k}2} \end{pmatrix} = -i\begin{pmatrix} \mathcal{A}_{\mathbf{k}11} & \mathcal{B}_{\mathbf{k}12} \\ \mathcal{B}_{\mathbf{k}21} & \mathcal{A}_{\mathbf{k}22} \end{pmatrix}\begin{pmatrix} s^+_{\mathbf{k}1} \\ s^+_{\mathbf{k}2} \end{pmatrix} \tag{7.7}$$

where

$$\begin{aligned} \mathcal{A}_{\mathbf{k}11} &= \frac{\gamma}{\mu_1}\left(J_{0,11} - J_{\mathbf{k}11}\right)\langle s_1\rangle + \frac{\gamma}{\mu_1}J_{0,12}\langle s_2\rangle \\ \mathcal{B}_{\mathbf{k}12} &= \frac{\gamma}{\mu_1}J_{\mathbf{k}12}\langle s_2\rangle \\ \mathcal{A}_{\mathbf{k}22} &= \frac{\gamma}{\mu_2}\left(J_{0,22} - J_{\mathbf{k}22}\right)\langle s_2\rangle + \frac{\gamma}{\mu_1}J_{0,21}\langle s_1\rangle \\ \mathcal{B}_{\mathbf{k}21} &= \frac{\gamma}{\mu_2}J_{\mathbf{k}21}\langle s_1\rangle \end{aligned} \tag{7.8}$$

As with the calculation of the ISF and DSF where a Holstein-Primakoff transformation was performed, equation (7.7) must also be transformed to a common set of spin operators. This is done by a Bogolioubov transformation (which the Holstein-Primakoff is a specific example of) which requires that the common operators retain bosonic commutation relations[124]

$$s^{+}_{\mathbf{k}1} = u_{\mathbf{k}}\alpha_{\mathbf{k}} + v_{\mathbf{k}}\beta^{\dagger}_{\mathbf{k}} \tag{7.9}$$

$$s^{+}_{\mathbf{k}2} = v_{\mathbf{k}}\alpha^{\dagger}_{\mathbf{k}} + u_{\mathbf{k}}\beta_{\mathbf{k}} \tag{7.10}$$

So $\alpha_{\mathbf{k}}$ and $\beta_{\mathbf{k}}$ are eigenstates of the system and the solution of Eq.(7.7) gives the dispersion relations

$$\omega_{\alpha}(\mathbf{k}) = \frac{1}{2}\left[\sqrt{\left(\mathcal{A}_{\mathbf{k}11} + \mathcal{A}_{\mathbf{k}22}\right)^2 - 4\mathcal{B}_{\mathbf{k}12}\mathcal{B}_{\mathbf{k}21}} - \left(\mathcal{A}_{\mathbf{k}22} - \mathcal{A}_{\mathbf{k}11}\right)\right] \tag{7.11}$$

$$\omega_{\beta}(\mathbf{k}) = \frac{1}{2}\left[\sqrt{\left(\mathcal{A}_{\mathbf{k}11} + \mathcal{A}_{\mathbf{k}22}\right)^2 - 4\mathcal{B}_{\mathbf{k}12}\mathcal{B}_{\mathbf{k}21}} - \left(\mathcal{A}_{\mathbf{k}11} - \mathcal{A}_{\mathbf{k}22}\right)\right] \tag{7.12}$$

where the coefficients of the transformation $u_{\mathbf{k}}$ and $v_{\mathbf{k}}$ read

$$u_{\mathbf{k}} = \sqrt{\frac{1}{2}\left(\frac{\mathcal{A}_{\mathbf{k}11} - \mathcal{A}_{\mathbf{k}22}}{\sqrt{\left(\mathcal{A}_{\mathbf{k}11} + \mathcal{A}_{\mathbf{k}22}\right)^2 - 4\mathcal{B}_{\mathbf{k}12}\mathcal{B}_{\mathbf{k}21}}} + 1\right)} \tag{7.13}$$

$$v_{\mathbf{k}} = \sqrt{\frac{1}{2}\left(\frac{\mathcal{A}_{\mathbf{k}11} - \mathcal{A}_{\mathbf{k}22}}{\sqrt{\left(\mathcal{A}_{\mathbf{k}11} + \mathcal{A}_{\mathbf{k}22}\right)^2 - 4\mathcal{B}_{\mathbf{k}12}\mathcal{B}_{\mathbf{k}21}}} - 1\right)} \tag{7.14}$$

obeying the Bogolioubov canonical transformation which requires $u_k^2 - v_k^2 = 1$. There is an energy gap at $\mathbf{k} = 0$ of $\omega_{\alpha} - \omega_{\beta} = \gamma J_{12}(\langle s_2\rangle - \langle s_1\rangle)/\mu_1\mu_2$.

Magnon Spectrum

When there is a very low concentration of Gd within the lattice (10-15%), the Gd sites act as impurities in what is predominately a ferromagnetic system. The DSF shows that the AF interactions are very localised to the edge of the Brillouin zone due to the limited range of the AF interactions. $\mathcal{A}'$ is maximised at the edge of the Brillouin zone, however the vast difference in the band frequencies here means that there is no coupling between modes. In equations (7.7) and (7.8) the off diagonal terms $\mathcal{B}_{\mathrm{k}12}$ and

$\mathcal{B}_{\mathbf{k}21}$ and inter-sublattice terms of $\mathcal{A}_{\mathbf{k}11}$ and $\mathcal{A}_{\mathbf{k}22}$ are very small. The result is that the spin operators $s^+_{\mathbf{k}1}$ and $s^+_{\mathbf{k}2}$ are almost purely eigenstates of $\alpha_{\mathbf{k}}$ and $\beta_{\mathbf{k}}$. Therefore the contribution of each branch of the DSF can be distinguished as excitations of either FeCo or Gd moments.

TIMS is readily found in Gd concentrations between 20-30%. In this regime the FM magnon contribution to spin fluctuations decreases in amplitude on large length scales (near the Γ-point) in favour of AF modes, gradually diminishing the ferromagnetic character of such spin fluctuations. The result is that the excitations become a mixed FM-AF mode, as seen also by the Bogoliubov transform (Eq. 7.10) in the LSWT. The two spin wave mode causes localised oscillations in the magnetisation, leading to the formation of a transient state where the magnetisation of both sublattices is aligned promoting the reversal. When the gap between the bands Δf is minimised, this maximises the energy and angular momentum flow between the sublattices. Therefore reducing Δf in areas of the Brillouin zone which are excited strongly allows reversal more readily.

At even higher Gd concentrations, around 35% and above, TIMS ceases to occur. The DSF shows that the AF band now dominates across the Brillouin zone and the FM modes contain little amplitude. The gap between the bands once again increases stopping the transfer of energy between non linear modes (Fig. 7.8c)

Amorphous Effects

The amorphous nature of GdFeCo, which is approximated in the lattice impurity model, means that the magnetic interactions are not uniform across the system. Instead there are some areas which contain clusters of Gd, where there will be a higher concentration of the AF FeCo-Gd interactions. This phenomenon causes AF interactions to be range-limited, leading to important effects in the magnon spectrum. To measure this effect in the impurity model, clusters within the lattice must be identified and properties their properties quantified. This is done using the Hoshen-Kopelman method. It is also important that these effects are include in the analytic theory and so percolation theory is employed, which describes the occurrence of clusters in random lattices from a statistical mechanics perspective. Using these two approaches it is shown that features in the DSF are directly determined by the properties of Gd clusters in the FeCo lattice.

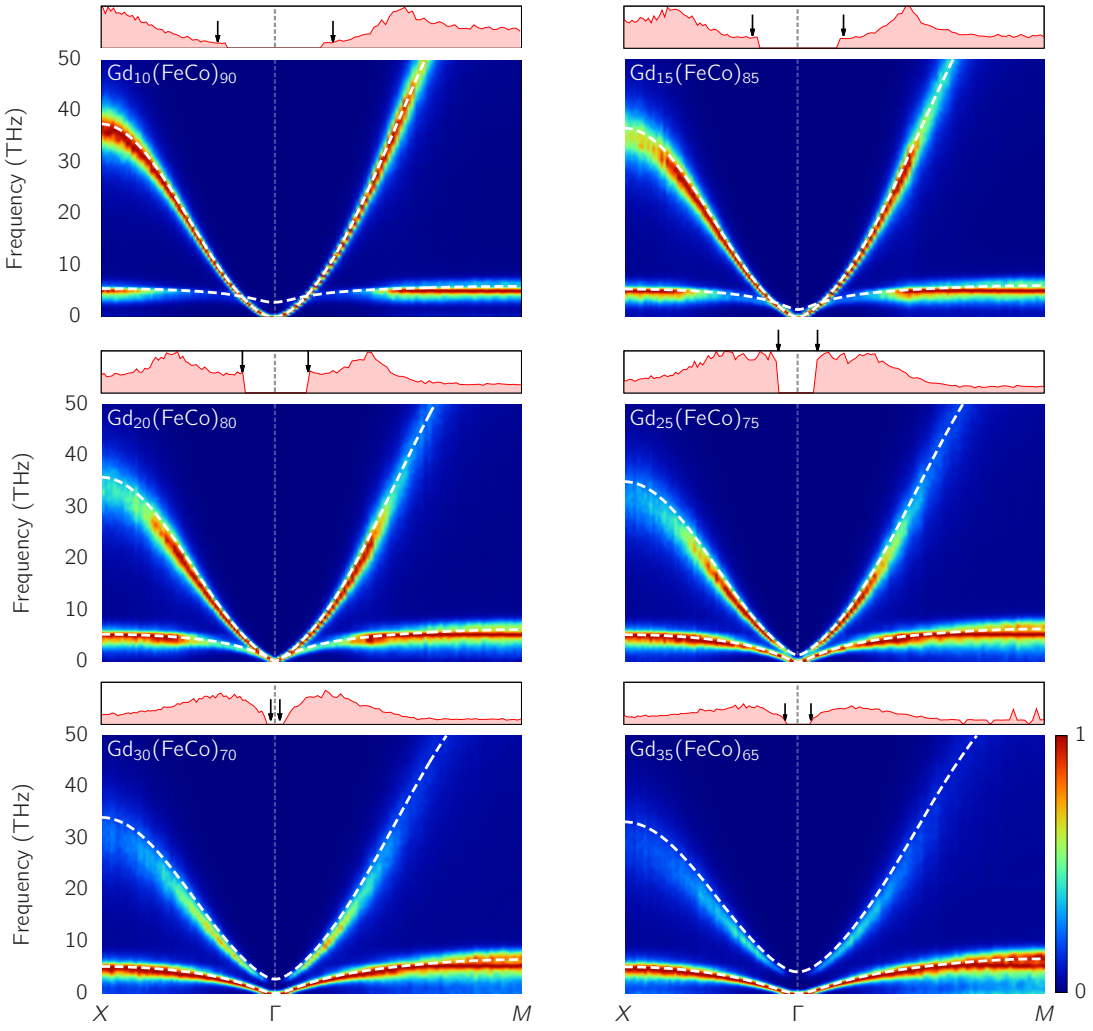

Figure 7.7 | Magnon band structures with Gd content calculated at 10K. The Gd concentration is given in the top right of each panel. The colour indicates the amplitude of excitation on each branch. The plot above each panel shows the amplitude of the two magnon state. This is not exist all the way to the Γ-point but has some finite extent. The arrows correspond to $1/\xi$, the reciprocal correlation length of Gd clusters within the lattice and describe the extent of the two-magnon region very well. The LSWT is overlaid on the panels in dashed-white, showing a good agreement for the band structure.

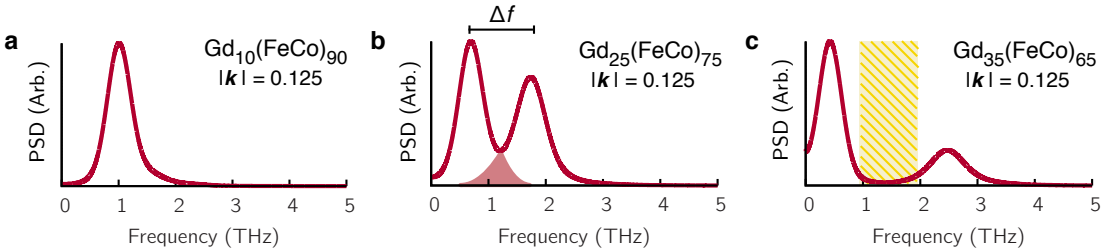

Figure 7.8 | PSD Cross Section. (**a**) At low Gd concentration, in the low k (long length scales) only one band is present. (**b**) At Gd concentrations where TIMS is found, the two bands are very close to each other in areas of the Brillouin zone which can be excited by laser heating. The highlighted area shows the overlap where non-linear interactions allow the transfer of energy and angular momentum between the sublattices. (**c**) As the Gd concentration increases further the gap between the bands (highlighted with hatching) means that interactions between these modes are negligible, so no switching can occur.

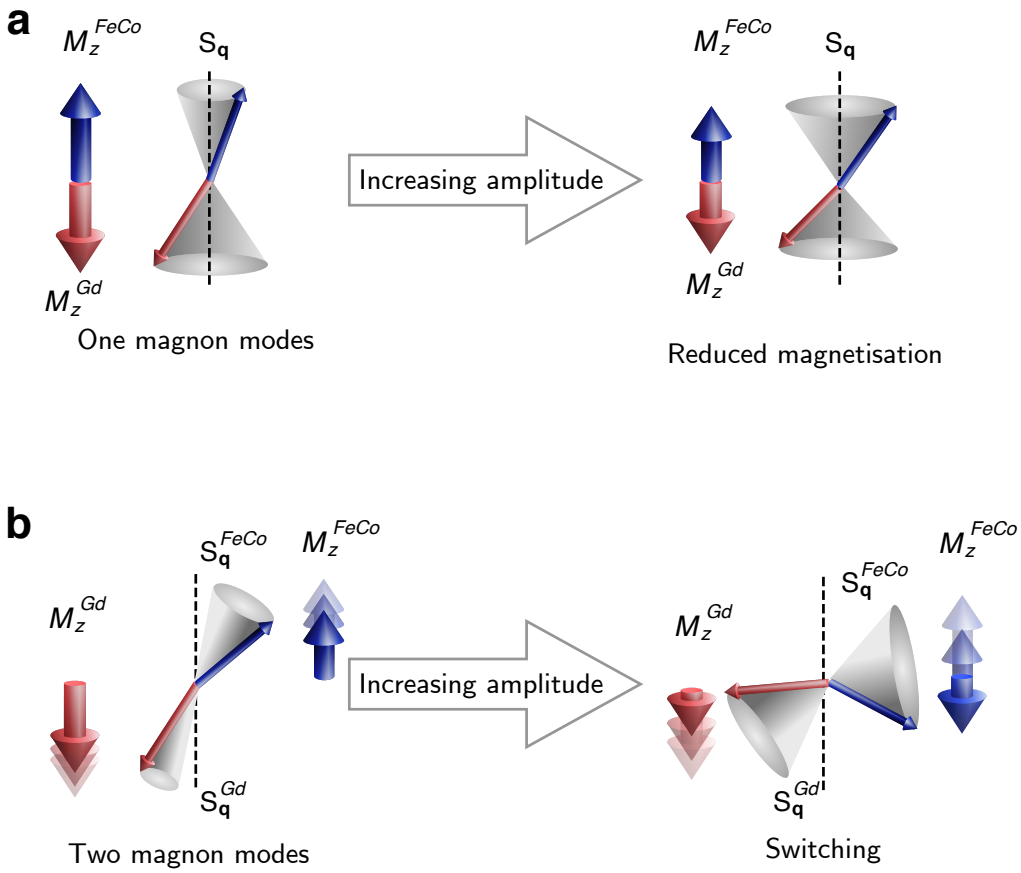

Figure 7.9 | The effect of one and two magnon modes on the magnetisation. (a) The magnetisation is directly related to the amplitude of one magnon modes, increasing the amplitude decreases the magnetisation. **(b)** Two magnon modes are the combination of two types of magnons. This leads to a dynamical mode where the magnetisation fluctuates with time. A strong excitation of this mode can lead to the transient ferromagnetic like state and subsequent reversal.

Hoshen-Kopelman Method

To quantify clusters of Gd within the lattice all unique clusters must be identified. These are defined as regions of Gd which are directly exchange coupled by Gd-Gd exchange. An efficient way of labeling unique clusters in a large lattice is required. One such method is described by Hoshen and Kopelman[128,129]. It involves scanning through the lattice once to number all connected regions in each column and then a second pass to re-number connected regions between columns (Fig. 7.10). During this processes the statistical properties of the clusters such as the number of sites it contains (s) are obtained and subsequently the radius of gyration (R) can be calculated. The discrete distribution of clusters is calculated, in which the number of clusters of a given size is denoted as n_s. The typical correlation length of clusters in the lattice can be calculated from these statistics as[130]

$$\xi^2 = \frac{2\sum_s s^2 \sum_{t=1}^{n_s} R_{st}^2}{\sum_s s^2 n_s} \tag{7.15}$$

This quantity gives a value for the typical spacial extent of an cluster randomly drawn from the lattice. Clearly on large lattices the distribution of cluster sizes can be quite large and also the radius of gyration can be quite different even for clusters of the same size. So ξ gives the dominant length scale occurring from the clusters.

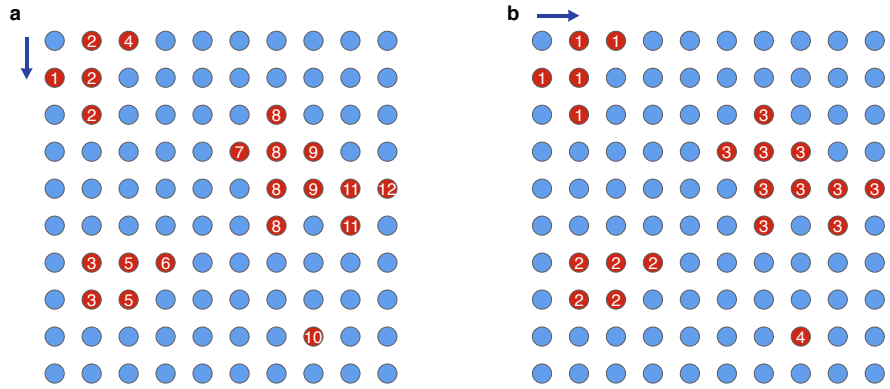

Figure 7.10 | Hoshen-Kopelman Method. Clusters are numbered first as connected regions in a column (**a**) then a second pass re-numbers unique clusters by checking connectivity in the other dimensions (**b**).

Percolation Theory

Percolation theory quantifies the properties of clusters in random lattices. One of the central ideas is that of a percolating cluster, which is a cluster that spans the lattice from

one side to the other. The percolation threshold (p_c) is a phase transition where the statistical properties of clusters is different above and below this threshold. As a phase transition theory, percolation theory is strictly only defined in the thermodynamic limit i.e. for and infinite system size. For finite sized systems the statistical properties must be rescaled to account for the absence of truly divergent behaviour at the critical point[97,130]. It is the typical length scale of Gd clusters which is of interest, as this corresponds to the typical length scale of AF interactions in the system. In percolation theory the correlation length of clusters is

$$\tilde{\xi} = A|p - p_c|^{-\nu} \tag{7.16}$$

where p is the fraction of occupied lattice sites, p_c is the percolation threshold, ν is a universal critical exponent and A is a scaling constant. The percolation threshold, p_c, depends on the symmetries of the lattice and is the same for all lattices which have the same underlying symmetries. In this work a simple cubic lattice is considered

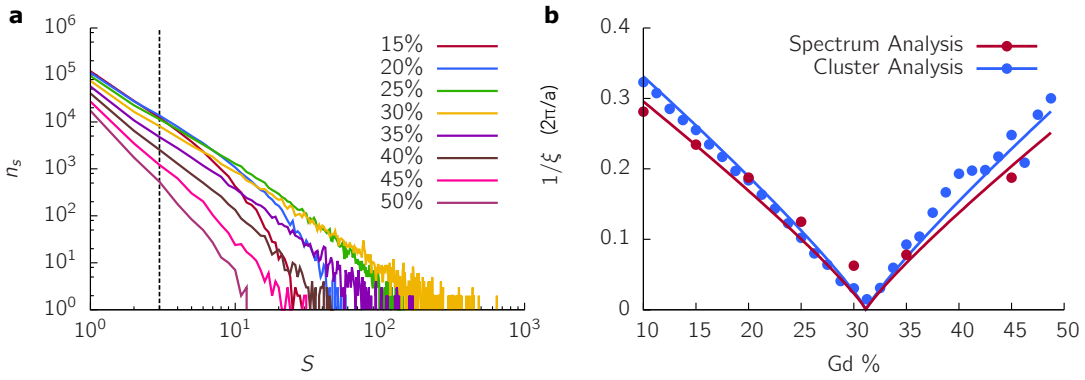

Figure 7.11 | Percolation. The correlation length, ξ as analysed from the Hoshen-Kopelman method are shown in circles and the dashed line is the fit of the percolation theory correlation length, Eq. (7.16), where only the prefactor A is fitted to account for finite size effects ($A = 0.78 \pm 0.01$). The same analysis is performed for the extent of two magnon states in the DSF, shown as squares with the solid line fit ($A = 0.87 \pm 0.04$).

and it is the *site percolation* which is of importance as it is the immediate surface area where the AF interactions exist. If the interaction through the clusters was of importance then instead the *bond percolation* would be considered. The value of p_c is therefore $p_c = 0.3116004$ (Ref. 131). The universal critical exponent, ν is common to all percolating systems and has the value $\nu = 0.875$ (Ref. 132). The scaling factor A of a bulk system is in general a function of the percolation threshold and the lattice size. In a single, finite system, A can be obtained by a fit to the correlation length obtained from both the Hoshen-Kopelman method and analysis of the two magnon states. The result in figure 7.11 shows a good agreement between the correlation lengths obtained

from both methods and with percolation theory for site percolation.

7.5 Band Gap Prediction

It was determined above that TIMS occurs due to the excitation of two magnon states which transfer angular momentum between the two sublattices in GdFeCo. The detailed information about the two magnon states is contained within the magnon spectrum of the material and as such, the magnon spectrum can be used to predict the occurrence of TIMS. The spectrum can be readily calculated from LSWT (with the VCA) as was shown above, but regions within the Brillouin zone where the relative amplitude is similar for both bands must be identified, i.e. the two magnon state is maximised according to the Bogolioubov transform (Eq.(7.10)). Within GdFeCo this is determined by the clustering within the amorphous lattice and the relevant length scale can be calculated from percolation theory (Eq.(7.16)). The efficient excitation of the two magnon modes requires that the difference in frequency of the bands at this point is small. In effect, the energy load supplied by the laser must be sufficient to excite across this frequency difference. But the energy load must not be so much that the magnetisation is destroyed. From the combination of analytic methods LSWT, VCA and percolation theory, an analytic model can be built which describes the frequency gap of the two magnon states. A temperature dependence can be included into the LSWT by calculating $\langle s_1 \rangle$ and $\langle s_2 \rangle$ in Eq. (7.8) from mean field theory[122]. This gives an experimentally accessible parameter space of the initial temperature and the Gd concentration, within which the energy threshold can be described (in terms of $\hbar\omega$) which is required for TIMS. As an instructive comparison the band gap at the Γ-point is calculated, which describes a simplified, macroscopic description where only the magnetisation compensation point is considered.

In the macroscopic picture, Fig. 7.12a, the minimum Δf follows the magnetisation compensation point, meaning that switching would always require a low energy threshold regardless of the initial temperature when close to the compensation point. This is not supported by experimental observations[9]. Furthermore the magnon spectrum shows that there are rarely two magnon states at the Γ-point, and this demonstrative diagram shows the importance of accounting for clustering within GdFeCo.

Going beyond the macroscopic picture and including the effects of Gd clustering, Fig. 7.12b, a radically different Δf landscape is obtained. There is now a temperature dependence to the band gap because the magnon spectrum is more temperature

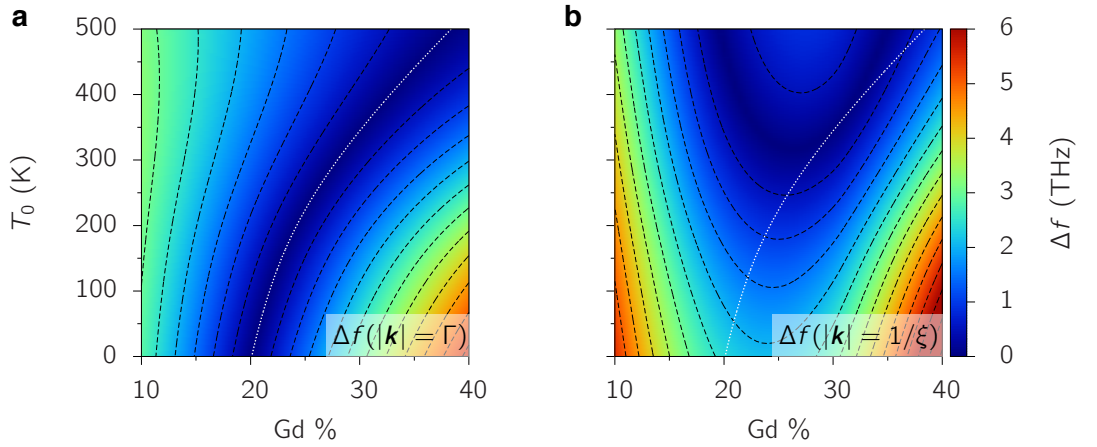

Figure 7.12 | TIMS band gaps. The colour maps give the predicted frequency gap Δf between the two bands in the DSF, using a combination of LSWT, VSA, MFA and percolation theory. The magnetisation compensation temperature is given by the white dashed line. (**a**) Considering the gap at the Γ-point (i.e. only consider the magnetisation) then the results show that the smallest band gap exists at the compensation temperature. However this does not explain all experimental results. (**b**) Taking into account the Gd clustering via percolation theory to predict the region of two magnon states gives a greatly modified result. Now the smallest frequency gap exists in a parabolic moat at high temperatures.

dependent at larger wave vectors, an effect known as magnon softening[14]. At room temperature the minimum Δf is relatively flat between 20-30% Gd concentrations, which explains why these concentrations are found to switch experimentally. Also in the region of 25-30% Gd concentration the compensation point is coincident with the Δf minimum around 300-400K. This helps to explain why experiments have frequently shown the compensation point to be important but also justifies why in some cases such as 20-25%, switching occurs even above the compensation point.

The predictive power of this theory can be tested by performing extensive switching simulations for different initial temperatures and Gd concentrations using a laser heat profile from the two-temperature model in the same way as the results in Fig. 7.4 were produced. Repeating these experiments for different laser fluence, a different energy load is applied to the system. To validate the combination of theories which form Fig. 7.12b switching must be shown to occur within a contour of $\Delta f(|\mathbf{k}| = 1/\xi)$ for a given energy load. The resulting switching windows are given in Fig. 7.13, where the colouring describes the area of parameter space where TIMS is found for a given laser fluence (energy load). There is a very good agreement between the observed switching and the contours and the larger energy loads switch systems with larger energy gaps.

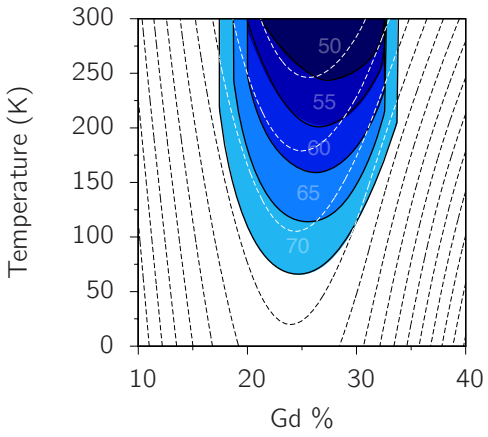

Figure 7.13 | TIMS switching windows. Each coloured area is the parameter space where TIMS is found during femtosecond laser heating experiments with the laser fluence as indicated on each area. The dashed contours overlaid are from the LSWT predictions in Fig. 7.12 when the effect of Gd clusters is taken into account.

7.6 Conclusions

The angular momentum transfer channel between the Gd and FeCo sublattices during TIMS has been identified in the impurity lattice Heisenberg model. The range limiting of the exchange interactions due to amorphous clustering in the lattice causes this transfer channel to be strong only in a small area of the Brillouin zone corresponding to a two magnon mode. The prediction that follows is that if the transfer channel is larger, i.e. the overlap of the two bands in the DSF is greater then TIMS occurs more readily. In the low Gd concentration, quasi-FM limit it is not possible to excite TIMS because the two magnon states only exist at the edge of the Brillouin zone which is not strongly excited by the laser heating. There is also a large difference in the frequency between the two bands in this regime which precludes the angular momentum transfer. In the high Gd concentration, quasi-AF regime, the exchange field from the inter-sublattice exchange raises the upper band in the DSF, leading to a wide gap between the two bands. The upper band is also weaker due to the reduction in FeCo intra-sublattice exchange. Therefore TIMS cannot occur because the angular momentum channel is impeded.

Using the knowledge of the microscopic mechanism for TIMS and the angular momentum transfer channel leads to the key optimisation criteria. The gap between the two excitation bands must be minimised where the two magnon state is strongest. In GdFeCo this is determined by the properties of the random clustering as it is the mix of interactions at the interfaces of the clusters that allows the angular momentum transfer. If enough energy is provided by the laser to excite the two magnon modes then TIMS

occurs. Otherwise the material demagnetises according to the usual behaviour in an FM or AF like material.

CHAPTER 8

Conclusions

Atomistic spin dynamics and multiscale modelling

Within this work a highly efficient model of atomistic spin dynamics was implemented on a graphical processing unit, leading to a performance increase of up to $75\times$ in simulations. The use of ASD is important in the work presented here due to the requirements of representing high temperatures and the need to include antiferromagnetic order. The increase in performance has allowed the study of novel magnetic materials on time and length scales which were previously prohibitive. These abilities were used to study the temperature scaling of micromagnetic parameters, in comparison to semi-analytic methods. By simulating very large systems of the order of two million atomistic spins up to the nanosecond time scale, it was possible to identify which decoupling schemes in the classical spectral density method, most closely reproduces the results of ASD. This work is of importance in multiscale modelling, where the ability to model materials on many time and length scales from an ab initio input is highly desirable. The Callen decoupling procedure, in the classical Heisenberg model, gives results which are most similar to ASD on micromagnetic length scales. However the anisotropy scaling was found to scale as $K(T) \sim M^3$ for all temperatures up to the Curie point, in contrast to the Callen scheme which predicts this only as the low temperature exponent.

Enhanced damping in antiferromagnetic/ferromagnetic bilayers

A study of the eigenmodes in ferromagnetic/antiferromagnetic bilayers was performed. Analytical calculations were made, taking the low frequency limit where the anti-

ferromagnetic dynamics are not considered. A local mode was identified within the system on the scale of the exchange length and that the eigenfrequency is strongly effected by the AF properties if the AF/FM coupling is sufficiently strong. Further analysis allowed the determination of the effective damping of the system, which increases with the interfacial coupling strength. The damping is also sensitive to the AF properties and this mechanism explains the enhanced damping found experimentally in spin valve structures. The analytic results were validated by comparison with numeric simulations. A numerical study of a bilayer with a disordered interface, beyond the analytic approach, found that the damping remained frequency dependent as determined by the effective interfacial exchange strength, rather than the local exchange strength at the interface. It was explained that due to the lack of excitation of areas of the AF due to the exchange frustration caused by the disorder at the interface. This limits the volume of the AF which partakes in the enhanced damping mechanism.

Four spin interactions in FeRh

The origin of the metamagnetic phase transition in FeRh has long been debated. On the basis of ab initio calculations a model was implemented in this work where an effective four spin interaction between the Fe moments leads to an AF-FM phase transition. This model was shown to contain an AF-FM phase transition and in parametrising to experiment, the model can closely represent FeRh. This provides weight to the argument of a purely magnetic origin to the phase transition as this model does not explicitly include lattice dynamics. The phase transition was found to occur due to the increased temperature dependence of the four spin exchange term in comparison to the Heisenberg term. At the phase transition the total energy is larger than that of higher temperatures and this dissipation of this excess energy may lead to the observed lattice expansion in FeRh. This model is unique in the ability to study dynamics through the phase transition. Studying the behaviour during femtosecond laser heating, mirroring experiments which have been performed, a similar dynamical behaviour was found. However there is some uncertainty in the time scales of the dynamics due to the complicated issue of the magnitude of the Gilbert damping in FeRh.

Thermally induced magnetisation switching in GdFeCo

The microscopic mechanism leading to thermally induced magnetisation switching has eluded explanation since the discovery of this phenomenon. A study was

conducted using large scale ASD simulations, to identify the microscopic mechanism and the important material parameters for TIMS. Linear spin wave theory was used in the virtual crystal approximation to form a theoretical framework to study and predict this phenomenon. By studying the spin wave dynamics and the spin wave spectrum the excitation of two magnon states in the spectrum, which mix AF and FM interactions, were identified. This leads to the switching in GdFeCo. The study of the spin wave spectrum allowed the identification of the important material feature, the relative energies of the two bands, which determines the energy threshold required for switching. The amorphous character of GdFeCo means that the two magnon states do not necessarily exist on all length scales. The mean size of clusters of Gd was found to determine the important length scale of the two magnon modes. Finally a comparison was performed between predictions of the energy threshold required for TIMS from the analytic framework with numerical simulations of femtosecond laser heating. Switching was found within contours of constant energy in regions of the explored parameter space (initial temperature, Gd concentration) for a given laser energy input.

8.1 Further Work

The work presented in this thesis just touches the surface of many interesting areas of magnetism. It is often the case in numerical work that there is a very large parameter space which can be explored, but finding interesting physics within this can prove difficult. Below is listed the intended direction for future research of the work which has been presented here.

Enhanced damping in antiferromagnetic/ferromagnetic bilayers

The work presented here is a smaller area of an extremely large parameter space. Several assumptions have been made in the analytic work, focussing on the practically exploitable low frequency regime. In the future the same approach will be used, but in a high frequency approximation, therefore retaining the dynamics of the antiferromagnet rather than using the quasi-static approximation. The results from this are interesting for the study of antiferromagnets experimentally. It may be possible to discern the properties of an antiferromagnet from how a coupled ferromagnet behaves when driven at high frequency, thus allowing access to measurements of antiferromagnets without the complication of methods such as X-ray magnetic linear dichroism (XMLD).

Thermally induced magnetisation switching in GdFeCo

A full parameterisation of the FeRh induced moment model from first principles will be attempted. This is difficult because of the difficulty in isolating four spin contributions in constrained field electronic structure calculations. A successful parameterisation of the Hamiltonian will give much weight to the evidence for a purely magnetic origin of the phase transition in FeRh. Coupling a lattice model to the magnetic model would be instructive to observe how the energy from the phase transition is dissipated within the lattice and if this is consistent with the observations that have been made experimentally. Beyond these immediate steps, a study of the surface effect in FeRh would be very interesting. There is some anecdotal evidence of a ferromagnetic 'skin' at the surface which does not undergo the phase transition. There are also experimental measurements of small FeRh clusters embedded in carbon which do not have the AF-FM phase transition and are always ferromagnetic[133]. Understanding how the reduced size and dimensionality effects the phase transition is important if FeRh is ever to be used in nanoscale applications.

Thermally induced magnetisation switching

This work has explained the observed switching behaviour within GdFeCo, which is an amorphous ferrimagnet. The next case which can be considered is heterostructures with antiferromagnet and ferromagnetic ordering. For such materials the k-vector at which the two magnon states are accessible is likely to be determined by the construction of the heterostructure, therefore allowing the tuning of TIMS to specific energy ranges. Experimentally it is important that TIMS can be found in systems which do not contain rare-earth elements. This is because sourcing rare-earth materials is now becoming costly due to export restrictions and also due to the practical implementation of there materials where corrosion can be a major issue.

APPENDIX A

Data Processing

A.1 Dynamic Structure Factors

The random fluctuations from the thermal noise term of the Langevin equation means that dynamic structure factors calculated in a reasonable time frame can be quite noisy. On top of this there is usually a large contrast between small and large wave vectors as the magnons follow an approximately Bose-Einstein distribution. Therefore it is useful to apply some smoothing and normalisation of the data to improve readability. Following the example of Bergman, Taroni, Bergqvist, Hellsvik, Hjörvarsson & Eriksson [14] we perform a Gaussian convolution of the frequency domain along constant $\mathbf{q}$. We then normalise the maximum peak value on this $\mathbf{q}$ to unity. This means that information can be read about the relative intensity of peaks along a given $\mathbf{q}$.

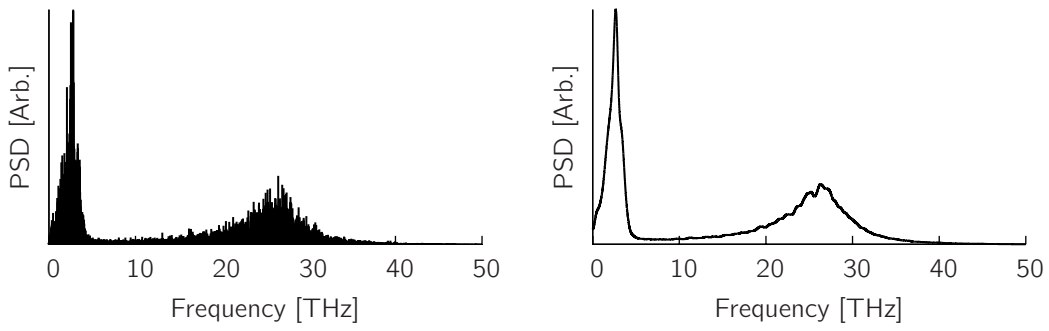

(a) Raw PSD data **(b)** PSD data after Gaussian convolution

Figure A.1 | Gaussian convolution of PSD. The PSD along one q-value is filtered using Gaussian convolution with a width of $\sigma = 0.95$ THz.

References

1. Richter, H. J. The transition from longitudinal to perpendicular recording. *J. Phys. D: Appl. Phys.* **40,** R149 (2007)

2. Rottmayer, R. E., Batra, S., Buechel, D., Challener, W. A., Hohlfeld, J., Kubota, Y., Li, L., Lu, B., Mihalcea, C., Mountfield, K., Pelhos, K., Peng, C., Rausch, T., Seigler, M. A., Weller, D. & Yang, X. M. Heat-Assisted Magnetic Recording. *IEEE Trans. Magn.* **42,** 2417 (2006)

3. Challener, W. A., Peng, C., Itagi, A. V., Karns, D., Peng, W., Peng, Y., Yang, X., Zhu, X., Gokemeijer, N. J., Hsia, Y. T., Ju, G., Rottmayer, R. E., Seigler, M. A. & Gage, E. C. Heat-assisted magnetic recording by a near-field transducer with efficient optical energy transfer. *Nature Photon.* **3,** 220 (2009)

4. Stanciu, C. D., Hansteen, F., Kimel, A. V., Kirilyuk, A., Tsukamoto, A., Itoh, A. & Rasing, T. All-Optical Magnetic Recording with Circularly Polarized Light. *Phys. Rev. Lett.* **99,** 047601 (2007)

5. Beaurepaire, E., Merle, J., Daunois, A. & Bigot, J.-Y. Ultrafast spin dynamics in ferromagnetic nickel. *Phys. Rev. Lett.* **76,** 4250 (1996)

6. Tudosa, I., Stamm, C., Kashuba, A. B., King, F., Siegmann, H. C., Stöhr, J., Ju, G., Lu, B. & Weller, D. The ultimate speed of magnetic switching in granular recording media. *Nature* **428,** 831 (2004)

7. Kimel, A. V., Kirilyuk, A., Usachev, P. A., Pisarev, R. V., Balbashov, A. M. & Rasing, T. Ultrafast non-thermal control of magnetization by instantaneous photomagnetic pulses. *Nature* **435,** 655 (2005)

8. Kirilyuk, A., Kimel, A. V. & Rasing, T. Ultrafast optical manipulation of magnetic order. *Rev. Mod. Phys.* **82,** 2731 (2010)

9. Ostler, T. A., Barker, J., Evans, R. F. L., Chantrell, R. W., Atxitia, U., Chubykalo-Fesenko, O., El Moussaoui, S., Le Guyader, L., Mengotti, E., Heyderman, L. J., Nolting, F., Tsukamoto, A., Itoh, A., Afanasiev, D., Ivanov, B. A., Kalashnikova, A. M., Vahaplar, K., Mentink, J., Kirilyuk, A., Rasing, T. & Kimel, A. V. Ultrafast heating as a sufficient stimulus for magnetization reversal in a ferrimagnet. *Nat. Commun.* **3,** 666 (2012)

10. Ju, G., Hohlfeld, J., Bergman, B., van de Veerdonk, R., Mryasov, O. N., Kim, J., Wu, X., Weller, D. & Koopmans, B. Ultrafast generation of ferromagnetic order via a laser-induced phase transformation in FeRh thin films. *Phys. Rev. Lett.* **93,** 197403 (2004)

11. Kazantseva, N., Hinzke, D., Nowak, U., Chantrell, R. W. & Chubykalo-Fesenko, O. Atomistic models of ultrafast reversal. *Phys. Status Solidi B* **244,** 4389 (2007)

12. Barker, J., Evans, R. F. L., Chantrell, R. W., Hinzke, D. & Nowak, U. Atomistic spin model simulation of magnetic reversal modes near the Curie point. *Appl. Phys. Lett.* **97,** 192504 (2010)

13. Radu, I., Vahaplar, K., Stamm, C., Kachel, T., Pontius, N., Dürr, H. A., Ostler, T. A., Barker, J., Evans, R. F. L., Chantrell, R. W., Tsukamoto, A., Itoh, A., Kirilyuk, A., Rasing, T. & Kimel, A. V. Transient ferromagnetic-like state mediating ultrafast reversal of antiferromagnetically coupled spins. *Nature* **472,** 205 (2011)

14. Bergman, A., Taroni, A., Bergqvist, L., Hellsvik, J., Hjörvarsson, B. & Eriksson, O. Magnon softening in a ferromagnetic monolayer: a first-principles spin dynamics study. *Phys. Rev. B* **81,** 144416 (2010)

15. Hellsvik, J., Skubic, B., Nordström, L. & Eriksson, O. Simulation of a spin-wave instability from atomistic spin dynamics. *Phys. Rev. B* **79,** 184426 (2009)

16. Gruner, M. E. Antiferromagnetism and segregation in cuboctahedral FePt nanoparticles. *J. Phys. D: Appl. Phys.* **41,** 134015 (2008)

17. Garanin, D. A. Fokker-Planck and Landau-Lifshitz-Bloch equations for classical ferromagnets. *Phys. Rev. B* **55,** 3050 (1997)

18. Evans, R. F. L., Hinzke, D., Atxitia, U., Nowak, U., Chantrell, R. W. & Chubykalo-Fesenko, O. Stochastic form of the Landau-Lifshitz-Bloch equation. *Phys. Rev. B* **85,** 014433 (2012)

19. Chantrell, R. W., Walmsley, N., Gore, J. & Maylin, M. Calculations of the susceptibility of interacting superparamagnetic particles. *Phys. Rev. B* **63,** 024410 (2000)

20. Schellekens, A. J. & Koopmans, B. Comparing Ultrafast Demagnetization Rates Between Competing Models for Finite Temperature Magnetism. *Phys. Rev. Lett.* **110,** 217204 (2013)

21. Battiato, M. & Carva, K. Superdiffusive Spin Transport as a Mechanism of Ultrafast Demagnetization. *Phys. Rev. Lett.* **105,** 027203 (2010)

22. Carva, K., Battiato, M. & Oppeneer, P. M. Ab Initio Investigation of the Elliott-Yafet Electron-Phonon Mechanism in Laser-Induced Ultrafast Demagnetization. *Phys. Rev. Lett.* **107,** 207201 (2011)

23. Skomski, R. *Simple Models of Magnetism* (Oxford University Press, New York, 2008)

24. Stöhr, J. & Siegmann, H. C. *Magnetism From Fundamentals to Nanoscale Dynamics* 1st ed. (Springer, 2006)

25. Stoner, E. C. Collective electron ferromagnetism. II. Energy and specific heat. *Proc. R. Soc. A* **169,** 339 (1939)

26. Gyorffy, B. L., Pindor, A., Staunton, J., Stocks, G. & Winter, H. A first-principles theory of ferromagnetic phase transitions in metals. *J. Phys. F: Met. Phys.* **15,** 1337 (1985)

27. Fähnle, M. & Illg, C. Electron theory of fast and ultrafast dissipative magnetization dynamics. *J. Phys.: Condens. Matter* **23,** 493201 (2011)

28. Hubbard, J. Electron Correlations in Narrow Energy Bands. *Proc. R. Soc. A* **276,** 238 (1963)

29. Anderson, P. *Concepts in Solids* (World Scientific, 1997)

30. Heinze, S., von Bergmann, K., Menzel, M., Brede, J., Kubetzka, A., Wiesendanger, R., Bihlmayer, G. & Blügel, S. Spontaneous atomic-scale magnetic skyrmion lattice in two dimensions. *Nature Physics* **7,** 713 (2011)

31. Landau, L. & Lifshitz, E. M. On the theory of the dispersion of magnetic permeability in ferromagnetic bodies. *Phys. Z. Soviet Union* **8,** 153 (1935)

32. Landau, L. & Lifshitz, E. M. Reprint: On the theory of the dispersion of magnetic permeability in ferromagnetic bodies. *Ukr. J. Phys.* **53,** 14 (2008)

33. Gurevich, A. & Melkov, G. A. *Magnetization Oscillations and Waves* (CRC Press, 1996)

34. Gilbert, T. A Lagrangian formulation of the gyromagnetic equation of the magnetic field - abstract only. *Phys. Rev.* **100,** 1243 (1955)

35. Gilbert, T. A phenomenological theory of damping in ferromagnetic materials. *IEEE Trans. Magn.* **40,** 3443 (2004)

36. Gilmore, K., Stiles, M. D., Seib, J., Steiauf, D. & Fähnle, M. Anisotropic damping of the magnetization dynamics in Ni, Co, and Fe. *Phys. Rev. B* **81,** 174414 (2010)

37. Brataas, A., Tserkovnyak, Y. & Bauer, G. E. W. Magnetization dissipation in ferromagnets from scattering theory. *Phys. Rev. B* **84,** 054416 (2011)

38. Liu, Y., Starikov, A. A., Yuan, Z. & Kelly, P. J. First-principles calculations of magnetization relaxation in pure Fe, Co, and Ni with frozen thermal lattice disorder. *arXiv,* 014412 (2011)

39. Mankovsky, S., Ködderitzsch, D., Woltersdorf, G. & Ebert, H. First-principles calculation of the Gilbert damping parameter via the linear response formalism with application to magnetic transition metals and alloys. *Phys. Rev. B* **87,** 014430 (2013)

40. Thijssen, J. M. *Computational Physics* 2nd ed. (Cambridge University Press, Cambridge, 2007)

41. Gardiner, C. *Handbook of Stochastic Methods* 2nd ed. (Springer, Berlin, 1985)

42. Berkov, D. V. & Gorn, N. Thermally activated processes in magnetic systems consisting of rigid dipoles: equivalence of the Ito and Stratonovich stochastic calculus. *J. Phys.: Condens. Matter* **14,** L281 (2002)

43. Ma, P.-W. & Dudarev, S. L. Longitudinal magnetic fluctuations in Langevin spin dynamics. *Phys. Rev. B* **86,** 054416 (2012)

44. Kloeden, P. E. & Platen, E. *Numerical Solution of Stochastic Differential Equations* (Springer, Berlin, 1999)

45. Honeycutt, R. Stochastic runge-kutta algorithms. I. White noise. *Phys. Rev. A* **45,** 600 (1992)

46. Kaganov, M. I., Lifshitz, I. M. & Tanatarov, L. V. Relaxation between electrons and crystalline lattices. *JETP,* 173 (1957)

47. Chen, J. K., Tzou, D. Y. & Beraun, J. E. A semiclassical two-temperature model for ultrafast laser heating. *Int. J. Heat Mass Transfer* **49,** 307 (2006)

48. Kazantseva, N., Nowak, U., Chantrell, R. W., Hohlfeld, J. & Rebei, A. Slow recovery of the magnetisation after a sub-picosecond heat pulse. *Europhys. Lett.* **81,** 27004 (2007)

49. Kittel, C. *Introduction to solid state physics* 6th (John Wiley & Sons, New York, 1986)

50. Kazantseva, N., Hinzke, D., Nowak, U., Chantrell, R. W., Atxitia, U. & Chubykalo-Fesenko, O. Towards multiscale modeling of magnetic materials: Simulations of FePt. *Phys. Rev. B* **77,** 184428 (2008)

51. Gibbs, N. E., Poole, W. G. Jr & Stockmeyer, P. K. A comparison of several bandwidth and profile reduction algorithms. *ACM T. Math. Software* **2,** 322 (1976)

52. Dowd, K. & Severance, C. R. *High performance computing* (O'Reilly Media, 1998)

53. *NVIDIA CUDA C Programming Guide* 2010

54. Bell, N. & Garland, M. *Implementing sparse matrix-vector multiplication on throughput-oriented processors* in *Proceedings of the Conference on High Performance Computing Networking, Storage and Analysis* (2009), 1

55. Majlis, N. *The Quantum Theory of Magnetism* (World Scientific, 2007)

56. Stancil, D. & Prabhakar, A. *Spin Waves* (Springer, 2009)

57. Douglass, R. Heat Transport by Spin Waves in Yttrium Iron Garnet. *Phys. Rev.* **129,** 1132 (1963)

58. Fähnle, M. & Steiauf, D. In *Handbook of Magnetism and Advanced Magnetic Materials I* (eds Kronmüller, H. & Parkin, S.) 282 (Wiley, Chichester, 2007)

59. Marshall, W. & Lovesey, S. W. *Theory of thermal neutron scattering* (Oxford University Press, 1971)

60. *Excitations in Disordered Systems* (ed Thorpe, M. F.) (Plenum Press, 1981)

61. Zhong, W., Overney, G. & Toma, D. Structural properties of Fe crystals. *Phys. Rev. B* **47,** 95 (1993)

62. Bhagat, S. & Lubitz, P. Temperature variation of ferromagnetic relaxation in the 3d transition metals. *Phys. Rev. B* **10,** 179 (1974)

63. Sasioglu, E., Friedrich, C. & Blügel, S. Strong magnon softening in tetragonal FeCo compounds. *arXiv* (2013)

64. Campana, L., D'Auria, A., D'Ambrosio, M., Esposito, U., De Cesare, L. & Kamieniarz, G. Spectral-density method for classical systems: Heisenberg ferromagnet. *Phys. Rev. B* **30,** 2769 (1984)

65. Cavallo, A., Cosenza, F. & De Cesare, L. In *New Developments in Ferromagnetism Research* (ed Murray, V. N.) 131 (Nova Science Publishers, 2006)

66. Atxitia, U., Hinzke, D., Chubykalo-Fesenko, O., Nowak, U., Kachkachi, H., Mryasov, O. N., Evans, R. F. L. & Chantrell, R. W. Multiscale modeling of magnetic materials: Temperature dependence of the exchange stiffness. *Phys. Rev. B* **82,** 134440 (2010)

67. Callen, H. Green Function Theory of Ferromagnetism. *Phys. Rev.* **130,** 890 (1963)

68. Copeland, J. & Gersch, H. First-Order Green's-Function Theory of the Heisenberg Ferromagnet. *Phys. Rev.* **143,** 236 (1966)

69. Swendsen, R. H. Modified Callen Decoupling in the Green's-Function Theory of the Heisenberg Ferromagnet with Application to the Europium Chalcogenides. *Phys. Rev. B* **5,** 116 (1972)

70. Bastardis, R., Atxitia, U., Chubykalo-Fesenko, O. & Kachkachi, H. Unified decoupling scheme for exchange and anisotropy contributions and temperature-dependent spectral properties of anisotropic spin systems. *Phys. Rev. B* **86,** 094415 (2012)

71. Kazantseva, N., Hinzke, D., Nowak, U., Chantrell, R. W., Atxitia, U. & Chubykalo-Fesenko, O. Towards multiscale modeling of magnetic materials: Simulations of FePt. *Phys. Rev. B* **77,** 184428 (2008)

72. Asselin, P., Evans, R. F. L., Barker, J., Chantrell, R. W., Yanes, R., Chubykalo-Fesenko, O., Hinzke, D. & Nowak, U. Constrained Monte Carlo method and calculation of the temperature dependence of magnetic anisotropy. *Phys. Rev. B* **82,** 054415 (2010)

73. Callen, H. & Callen, E. The present status of the temperature dependence of magnetocrystalline anisotropy, and the power law. *J. Phys. Chem. Solids* **27,** 1271 (1966)

74. Meiklejohn, W. & Bean, C. New magnetic anisotropy. *Phys. Rev.* **102,** 1413 (1956)

75. Weber, M., Nembach, H. & Hillebrands, B. Modified Gilbert damping due to exchange bias in NiFe/FeMn bilayers. *J. Appl. Phys.* **97,** 10A701 (2005)

76. Smith, N., Carey, M. & Childress, J. Measurement of Gilbert damping parameters in nanoscale CPP-GMR spin valves. *Phys. Rev. B* **81,** 184431 (2010)

77. O grady, K., Fernandez-Outon, L. & Vallejo-Fernandez, G. A new paradigm for exchange bias in polycrystalline thin films. *J. Magn. Magn. Mater.* **322,** 883 (2010)

78. Cottam, M. G. & Tilley, D. R. *Introduction to surface and superlattice exications* 1st ed. (Cambridge University Press, New York, 1989)

79. Ivanov, B. A., Zaspel, C. & Merkulov, A. Discommensurate and inhomogeneous states induced by a strong magnetic field in low-dimensional antiferromagnets. *Phys. Rev. B* **68,** 212403 (2003)

80. Landau, L. & Lifshitz, E. M. *Mechanics* Third (Elsevier, 1976)

81. Sukhov, A., Usadel, K. D. & Nowak, U. Ferromagnetic resonance in an ensemble of nanoparticles with randomly distributed anisotropy axes. *J. Magn. Magn. Mater.* **320,** 31 (2008)

82. Sawyer, D., George, R. & Bagger, J. Magnetic Transformations in Iron-Rhodium Alloys. *Platin. Met. Rev.* **7,** 29 (1963)

83. Kouvel, J. S. & Hartelius, C. C. Anomalous Magnetic Moments and Transformations in the Ordered Alloy FeRh. *J. Appl. Phys.* **33,** 1343 (1962)

84. Kouvel, J. S. & Hartelius, C. C. Anomalous magnetic moments and transformations in the ordered alloy FeRh. *J. Appl. Phys.* **33,** 1343 (1962)

85. Moruzzi, V. & Marcus, P. Antiferromagnetic-ferromagnetic transition in FeRh. *Phys. Rev. B* **46,** 2864 (1992)

86. Mryasov, O. N. Magnetic interactions and phase transformations in FeM, M=(Pt, Rh) ordered alloys. *Phase Transit.* **78,** 197 (2005)

87. Moruzzi, V. & Marcus, P. Magnetic structure in FeRh from constrained total-energy calculations. *Solid State Commun.* **83,** 735 (1992)

88. Sandratskii, L. M. & Mavropoulos, P. Magnetic excitations and femtomagnetism of FeRh: A first-principles study. *Phys. Rev. B* **83,** 174408 (2011)

89. Gruner, M. E., Hoffmann, E. & Entel, P. Instability of the rhodium magnetic moment as the origin of the metamagnetic phase transition in α-FeRh. *Phys. Rev. B* **67,** 064415 (2003)

90. Capel, H. W. On the possibility of first-order phase transitions in Ising systems of triplet ions with zero-field splitting. *Physica* **32,** 966 (1966)

91. Capel, H. W. On the possibility of first-order transitions in Ising systems of triplet ions with zero-field splitting II. *Physica* **33,** 295 (1967)

92. Capel, H. W. On the possibility of first-order transitions in Ising systems of triplet ions with zero-field splitting III. *Physica* **37,** 423 (1967)

93. Derlet, P. M. Landau-Heisenberg Hamiltonian model for FeRh. *Phys. Rev. B* **85,** 174431 (2012)

94. Onyszkiewicz, Z. A simple model describing all types of collinear metamagnets. *Phys. Lett.* **68,** 113 (1978)

95. Mouritsen, O., Frank, B. & Mukamel, D. Cubic Ising lattices with four-spin interactions. *Phys. Rev. B* **27,** 3018 (1983)

96. Baldasseroni, C., Bordel, C., Gray, A. X., Kaiser, A. M., Kronast, F., Herrero-Albillos, J., Schneider, C. M., Fadley, C. S. & Hellman, F. Temperature-driven

nucleation of ferromagnetic domains in FeRh thin films. *Appl. Phys. Lett.* **100,** 262401 (2012)

97. Goldenfeld, N. *Lectures on phase transitions and the renormalization group* (Perseus Books, 1992)

98. Thiele, J.-U., Maat, S. & Fullerton, E. E. FeRh/FePt exchange spring films for thermally assisted magnetic recording media. *Appl. Phys. Lett.* **82,** 2859 (2003)

99. Binder, K. Theory of first-order phase transitions. *Rep. Prog. Phys.* **50,** 783 (1987)

100. Ko, H. Y. Y., Suzuki, T., Nam, N. T., Phuoc, N. N., Cao, J. & Hirotsu, Y. Magnetic and structural characterizations on nanoparticles of FePt, FeRh and their composites. *J. Magn. Magn. Mater.* **320,** 3120 (2008)

101. Ko, H. Y. Y., Inoue, S., Nam, N. T., Suzuki, T. & Hirotsu, Y. Magnetic Properties of Nanocomposite Particles of FePt/FeRh. *IEEE Trans. Magn.* **44,** 2780 (2008)

102. Castets, A., Tochetti, D. & Hennion, B. Spin wave spectrum of iron-rhodium alloy in antiferromagnetic and ferromagnetic phases. *Physica B* **86,** 353 (1977)

103. Bergman, B., Ju, G., Hohlfeld, J., van de Veerdonk, R., Kim, J.-Y., Wu, X., Weller, D. & Koopmans, B. Identifying growth mechanisms for laser-induced magnetization in FeRh. *Phys. Rev. B* **73,** 060407 (2006)

104. Mancini, E., Pressacco, F., Haertinger, M., Fullerton, E. E., Suzuki, T., Wolters-dorf, G. & Back, C. H. Magnetic phase transition in iron–rhodium thin films probed by ferromagnetic resonance. *J. Phys. D: Appl. Phys.* **46,** 245302 (2013)

105. Thiele, J.-U., Buess, M. & Back, C. H. Spin dynamics of the antiferromagnetic-to-ferromagnetic phase transition in FeRh on a sub-picosecond time scale. *Appl. Phys. Lett.* **85,** 2857 (2004)

106. Alebrand, S., Gottwald, M., Hehn, M., Steil, D., Cinchetti, M., Lacour, D., Fullerton, E. E., Aeschlimann, M. & Mangin, S. Light-induced magnetization reversal of high-anisotropy TbCo alloy films. *Appl. Phys. Lett.* **101,** 162408 (2012)

107. The new oil? *Nature Photon.* **5,** 1 (2011)

108. Pitaevskii, L. P. Electric forces in a transparent disperive medium. *Sov. Phys. JETP* **12,** 1008 (1961)

109. Van der Ziel, J., Pershan, P. & Malmstrom, L. Optically-Induced Magnetization Resulting from the Inverse Faraday Effect. *Phys. Rev. Lett.* **15,** 190 (1965)

110. Kimel, A. V., Kirilyuk, A., Tsvetkov, A., Pisarev, R. V. & Rasing, T. Laser-induced ultrafast spin reorientation in the antiferromagnet $TmFeO_3$. *Nature* **429,** 850 (2004)

111. Kimel, A. V., Stanciu, C. D., Usachev, P. A., Pisarev, R. V., Gridnev, V. N., Kirilyuk, A. & Rasing, T. Optical excitation of antiferromagnetic resonance in $TmFeO_3$. *Phys. Rev. B* **74,** 060403(R) (2006)

112. Kimel, A. V., Kirilyuk, A. & Rasing, T. Femtosecond opto-magnetism: ultrafast laser manipulation of magnetic materials. *Laser Photon. Rev.* **1,** 275 (2007)

113. Khorsand, A., Savoini, M., Kirilyuk, A., Kimel, A. V., Tsukamoto, A., Itoh, A. & Rasing, T. Role of Magnetic Circular Dichroism in All-Optical Magnetic Recording. *Phys. Rev. Lett.* **108,** 127205 (2012)

114. Mentink, J., Hellsvik, J., Afanasiev, D., Ivanov, B. A., Kirilyuk, A., Kimel, A. V., Eriksson, O., Katsnelson, M. I. & Rasing, T. Ultrafast Spin Dynamics in Multisublattice Magnets. *Phys. Rev. Lett.* **108,** 057202 (2012)

115. Atxitia, U., Ostler, T. A., Barker, J., Evans, R. F. L., Chantrell, R. W. & Chubykalo-Fesenko, O. Ultrafast dynamical path for the switching of a ferrimagnet after femtosecond heating. *Phys. Rev. B* **87,** 224417 (2013)

116. Schellekens, A. J. & Koopmans, B. Microscopic model for ultrafast magnetization dynamics of multisublattice magnets. *Phys. Rev. B* **87,** 020407(R) (2013)

117. Wangsness, R. K. Sublattice Effects in Magnetic Resonance. *Phys. Rev.* **91,** 1085 (1953)

118. Medapalli, R., Razdolski, I., Savoini, M., Khorsand, A., Kirilyuk, A., Kimel, A. V., Rasing, T., Kalashnikova, A. M., Tsukamoto, A. & Itoh, A. Efficiency of ultrafast laser-induced demagnetization in $Gd_xFe_{100-x-y}Co_y$ alloys. *Phys. Rev. B* **86,** 054442 (2012)

119. Medapalli, R., Razdolski, I., Savoini, M., Khorsand, A. R., Kalashnikova, A. M., Tsukamoto, A., Itoh, A., Kirilyuk, A., Kimel, A. V. & Rasing, T. The role of magnetization compensation point for efficient ultrafast control of magnetization in $Gd_{24}Fe_{66.5}Co_{9.5}$ alloy. *Eur. Phys. J. B* **86,** 183 (2013)

120. Hassdenteufel, A., Hebler, B., Schubert, C., Liebig, A., Teich, M., Helm, M., Aeschlimann, M., Albrecht, M. & Bratschitsch, R. Thermally Assisted All-Optical Helicity Dependent Magnetic Switching in Amorphous $Fe_{100-x}Tb_x$Alloy Films. *Adv. Mater.* **25,** 3122 (2013)

121. Graves, C. E., Reid, A. H., Wang, T., Wu, B., de Jong, S., Vahaplar, K., Radu, I., Bernstein, D. P., Messerschmidt, M., Müller, L., Coffee, R., Bionta, M., Epp, S. W., Hartmann, R., Kimmel, N., Hauser, G., Hartmann, A., Holl, P., Gorke, H., Mentink, J., Tsukamoto, A., Fognini, A., Turner, J. J., Schlotter, W. F., Rolles, D., Soltau, H., Strüder, L., Acremann, Y., Kimel, A. V., Kirilyuk, A., Rasing, T., Stöhr, J., Scherz, A. O. & Dürr, H. A. Nanoscale spin reversal by nonlocal angular momentum transfer following ultrafast laser excitation in ferrimagnetic GdFeCo. *Nature Mater.* **12,** 293–298 (2013)

122. Ostler, T. A., Evans, R., Chantrell, R. W., Atxitia, U., Chubykalo-Fesenko, O., Radu, I., Abrudan, R., Radu, F., Tsukamoto, A., Itoh, A., Kirilyuk, A., Rasing, T. & Kimel, A. V. Crystallographically amorphous ferrimagnetic alloys: Comparing a localized atomistic spin model with experiments. *Phys. Rev. B* **84,** 024407 (2011)

123. Nowak, U. Thermally activated reversal in magnetic nanostructures. *Annual Reviews of Computational Physics IX* **105** (2001)

124. Mahan, G. D. *Many-particle physics* 2nd ed. (Plenum Press, New York, 1990)

125. Holstein, T. & Primakoff, H. Field dependence of the intrinsic domain magnetization of a ferromagnet. *Phys. Rev.* **58,** 1098 (1940)

126. Skubic, B., Hellsvik, J., Nordström, L. & Eriksson, O. A method for atomistic spin dynamics simulations: implementation and examples. *J. Phys.: Condens. Matter* **20,** 315203 (2008)

127. Djordjevic, M. & Münzenberg, M. G. Connecting the timescales in picosecond remagnetization experiments. *Phys. Rev. B* **75,** 012404 (2007)

128. Hoshen, J. & Kopelman, R. Percolation and cluster distribution. I. Cluster multiple labeling technique and critical concentration algorithm. *Phys. Rev. B* **14,** 3438 (1976)

129. Hoshen, J., Berry, M. & Minser, K. Percolation and cluster structure parameters: The enhanced Hoshen-Kopelman algorithm. *Phys. Rev. E* **56,** 1455 (1997)

130. Stauffer, D. & Aharoni, A. *Introduction to Percolation Theory* 2nd ed. (Taylor & Francis, London, 1994)

131. Grassberger, P. Numerical studies of critical percolation in three dimensions. *J. Phys. A: Math. Gen.* **25,** 5867 (1992)

132. Lorenz, C. & Ziff, R. Precise determination of the bond percolation thresholds and finite-size scaling corrections for the sc, fcc, and bcc lattices. *Phys. Rev. E* **57,** 230 (1998)

133. Hillion, A., Cavallin, A., Vlaic, S., Tamion, A., Tournus, F., Khadra, G., Dreiser, J., Piamonteze, C., Nolting, F., Rusponi, S., Sato, K., Konno, T. J., Proux, O., Dupuis, V. & Brune, H. Low Temperature Ferromagnetism in Chemically Ordered FeRh Nanocrystals. *Phys. Rev. Lett.* **110,** 087207 (2013)